DRAFT VERSION MAY 24, 2026
Typeset using LaTeX **twocolumn** style in AASTeX631

GWTC-5.0: Observations from the Second Part of the Fourth LIGO-Virgo-KAGRA Observing Run and Updates to the Gravitational-Wave Transient Catalog

THE LIGO SCIENTIFIC COLLABORATION, THE VIRGO COLLABORATION, AND THE KAGRA COLLABORATION

(Compiled: May 24, 2026)

ABSTRACT

Version 5.0 of the Gravitational-Wave Transient Catalog (GWTC-5.0) adds new candidates detected by the LIGO–Virgo–KAGRA network of observatories through the second part of the fourth observing run (O4b: 2024 April 10 15:00:00 to 2025 January 28 17:00:00 UTC) and four days of the preceding engineering run (2024 April 6 to 2024 April 10). We find 161 compact binary coalescence candidates that are identified by at least one of our search algorithms with a probability of astrophysical origin $p_{\rm astro} \geq 0.5$ and that are not vetoed during event validation. We also provide detailed source property measurements for 104 candidates that have a false-alarm rate $< 1\,\mathrm{yr}^{-1}$. Based on the inferred component masses, all these candidates are consistent with signals from binary black holes. Median inferred component masses in the new candidates range from $5.14 M_\odot$ (GW241109_115924) to $70 M_\odot$ (GW241116_151753). Improvements in detector sensitivity allow us to observe compact binary coalescences with increasing clarity: 5 binary-black-hole signals have network signal-to-noise ratio exceeding 30, with a maximum to date of 76.9 for GW250114_082203. Such loud signals enable more precise studies of properties of their astrophysical sources and tests of general relativity. We also present updated results up to the first part of the fourth observing run, identifying 229 candidates. This brings the total number of transients in the cumulative GWTC having $p_{\rm astro} \geq 0.5$ to 390, further expanding the size of the catalog and our view of the gravitational-wave universe.

Keywords: Gravitational wave astronomy (675); Gravitational wave detectors (676); Gravitational wave sources (677); Stellar mass black holes (1611); Neutron stars (1108)

1. INTRODUCTION

An ever-increasing population of gravitational-wave (GW) sources in our Universe is now being uncovered by the Laser Interferometer Gravitational-Wave Observatory (LIGO; Aasi et al. 2015) and the Virgo (Acernese et al. 2015) and KAGRA (Akutsu et al. 2021) observatories. In the past decade, these detectors have made many observations of black holes (BHs) and neutron stars (NSs), with detection of transient GWs from binary BHs (BBHs; Abbott et al. 2016a), binary NSs (BNSs; Abbott et al. 2017a), and NS–BH binaries (NSBHs; Abbott et al. 2021a) with a significant impact on physics, astrophysics, and cosmology. The increasing number of detected GW candidates has been summarized in the LIGO–Virgo–KAGRA Collaboration (LVK) Gravitational-Wave Transient Catalogs; GWTC-1 (Abbott et al. 2019a), GWTC-2 (Abbott et al. 2021b, 2024), GWTC-3 (Abbott et al. 2023a) and GWTC-4 (Abac et al. 2025)[1]. This work presents the observations and results of version 5.0 (GWTC-5.0) and is part of a collection of articles which also includes an introduction (Abac et al. 2026a) and a description of the data-analysis methods (Abac et al. 2026b); we refer readers to these articles for contextual information on the results presented here.

GWTC-5.0 updates the previous GWTC-4.0 (Abac et al. 2025) by including the results of searches for compact binary coalescences (CBCs) in data collected through the end of the second part of the fourth observing run (O4b). While the overall structure and analysis framework of this paper closely follow those used in the previous GWTC-4.0 paper (Abac et al. 2025a), the results presented here include discoveries from the new data-taking period, and hence, constitute the most comprehensive set of GW observations to date. This period consists of data collected by the three-detector network

Corresponding author: LSC P&P Committee, via LVK Publications as proxy
lvc.publications@ligo.org

[1] In the catalog naming convention, GWTC-<*major*> can refer to any minor version having the major version number. See Abac et al. (2026a) for more details of the naming convention.

of LIGO Hanford Observatory (LHO), LIGO Livingston Observatory (LLO) and Virgo between 2024 April 10 15:00:00 and 2025 January 28 17:00:00 UTC; the KAGRA detector did not participate in O4b. Our analyses also include four days of data (between 2024 April 6 and 2024 April 10) from a pre-O4b engineering run, which was conducted between 2024 March 20 and 2024 April 10 UTC (Abac et al. 2026c). During the data-taking period, the three (any combination of two) detectors took data at science quality for about 30 % (70 %) of the time, respectively. More details on the observed data can be found in Abac et al. (2026a,c).

We identify 1886 candidates with a false-alarm rate (FAR) $< 2\,\mathrm{d}^{-1}$ in at least one of our four search pipelines. Of these candidates, 161 have a probability of astrophysical CBC origin of $p_{\mathrm{astro}} \geq 0.5$ in at least one pipeline, and are not vetoed during event validation (Abac et al. 2026b). In online, low-latency analyses, there were 1820 candidates assigned a FAR $< 2\,\mathrm{d}^{-1}$ by at least one search pipeline. Of these candidates, 114 reached a FAR < 1 per $30\,\mathrm{d}$ after applying a trials factor to account for the number of simultaneously observing analyses and were reported as significant detection candidates. No confident multimessenger counterparts have been reported for any O4b candidates. Our offline analyses recover 94 of the candidates identified as significant in online searches in the subset of candidates with both $p_{\mathrm{astro}} \geq 0.5$ and FAR $< 1\,\mathrm{yr}^{-1}$. We identify 23 new candidates with $p_{\mathrm{astro}} \geq 0.5$ which were not part of the 1820 candidates identified in online as either significant or of low significance; of these 23 only 3 events have a FAR $< 1\,\mathrm{yr}^{-1}$.

We also update some of the results for candidates identified in the first part of the fourth observing run (O4a) and published in Abac et al. (2025a), based on the reanalysis by the two search pipelines PyCBC and GstLAL with updated configurations: Appendix A presents detailed results of this reanalysis. To clarify that these O4a results supersede those in GWTC-4.0, we name them GWTC-4.1. However, as GWTC-5.0 is a cumulative catalog, all the results labeled GWTC-4.1 are included in GWTC-5.0. Combined with these updated 229 candidates up to O4a, GWTC-5.0 now contains 390 candidates with $p_{\mathrm{astro}} \geq 0.5$ and not vetoed during event validation.

We analyze in detail the properties of a smaller, higher-purity (≈ 0.879) subset of 104 candidates with a FAR $< 1\,\mathrm{yr}^{-1}$ and which are not vetoed during event validation. However, GW240406_062847 was excluded from this current analysis, as detailed information about strain data calibration during the pre-O4b engineering run was not available. We find that all new candidates in GWTC-5.0 are entirely consistent with being BBHs, and we do not find any new BNS or NSBH candidates in O4b. The BBHs reported here have properties that span a similar range of values as those reported in previous GWTC versions (Abbott et al. 2019a, 2021b, 2024, 2023a; Abac et al. 2025); however, a number of candidates exhibit new extremes.

Among the notable candidates, GW250114_082203 (Abac et al. 2025b) was observed with a signal-to-noise ratio (SNR) of 76.9 (along this paper, we define the SNR to be the matched-filter network SNR), which is higher than any of our previously detected GW candidates including the loudest one during O4a, GW230814_230901 (Abac et al. 2025). Despite only the two LIGO detectors operating at the time of GW250114_082203, this unprecedented SNR led to a relatively precise localization of the source, with a 90% credible area of 42 deg^2. GW240925_005809 is another BBH candidate with a high SNR of 31.9. Miscalibration of the LHO detector around the time of this candidate allowed us to use this high-SNR signal to make informative astrophysical measurements of GW detector calibration, verifying in-situ detector-based measurements, for the first time (Abac et al. 2026a).

As our catalog grows in parallel with the increasing sensitivity of the GW detector network, we detect a larger number of remarkable candidates and measure their source properties more precisely. In particular, during O4b the three-detector network drastically improved our ability to measure the sky location of sources. For example, GW240615_113620 is the best localized GW source observed to date, with a 90% credible area of 6 deg^2. Several BBH sources reported here have a well-measured effective inspiral spin χ_{eff} deviating from zero with high probability. Here, χ_{eff} is a measure of the total spin angular momentum aligned with the orbital angular momentum (see Abac et al. 2026a, for a definition). These include GW241011_233834 and GW241110_124123 (Abac et al. 2025c) with $\chi_{\mathrm{eff}} = 0.50^{+0.06}_{-0.04}$ and $\chi_{\mathrm{eff}} = -0.31^{+0.23}_{-0.18}$, respectively (here, and throughout this work, we present the median value and uncertainties based on the 90% credible interval). Both of these are also notable for having measured masses that rule out equal component masses with mass ratio $q = 0.31^{+0.07}_{-0.06}$ and $0.49^{+0.34}_{-0.19}$, respectively. The source of GW241011_233834 is also the closest among the new O4b candidates, with a luminosity distance of $0.21^{+0.04}_{-0.04}$ Gpc. Additionally, we highlight several other candidates with support for non-negligible spins.

The remainder of this article is structured as follows. In Section 2, we present the new candidates identified by search pipelines and discuss similarities and differences with the set identified by low-latency analyses. For a high-purity subset of these candidates, we present measurements of the inferred astrophysical source properties and discuss the impact of systematic differences between waveform models in Section 3. Finally, we summarize the results and discuss future prospects for GW astronomy in Section 4. As appendices, we provide detailed results of our O4a reanalysis in Appendix A; additional details of search results for O4b candidates in Appendix B, and a list of O4b candidates for which a glitch mitigation process was applied in Appendix C.

2. CANDIDATE LIST

Search pipelines operate in two different modes: online (low latency) and offline. Online searches analyze data in near real time as they are collected. The rapid identification of candidate astrophysical transients in low latency enables public alerts and facilitates searches for multimessenger counterparts (Abbott et al. 2019b, 2023a; Abac et al.

2026b). Offline searches can be run at a higher latency using data that have undergone final calibration, and benefit from additional noise subtraction (Vajente et al. 2020; Soni et al. 2025) and the identification of transient noise artifacts, known as *glitches* (Nuttall 2018; Glanzer et al. 2023; Soni et al. 2025), based on detector-monitor channel information (Essick et al. 2020; Huxford et al. 2024). Additionally, online searches may be subject to occasional data dropout due to network instability or computing outages, while offline searches have access to the complete dataset. Together with other methodological differences, these factors generally make offline searches more sensitive than their online counterparts, which leads to differences between the final candidate list and the initial online results. The majority of low-FAR online candidates (e.g., with a FAR $< 1\,\mathrm{yr}^{-1}$) are expected to remain significant in offline searches, but candidates that were initially identified with a higher FAR can change in significance when later re-evaluated.

In this paper, we describe the offline search results in O4b data from four search pipelines: cWB-BBH (Klimenko et al. 2005, 2008, 2016; Mishra et al. 2025), GstLAL (Messick et al. 2017; Sachdev et al. 2019; Tsukada et al. 2023; Sakon et al. 2024; Joshi et al. 2025), MBTA (Alléné et al. 2025), and PyCBC (Dal Canton et al. 2014; Usman et al. 2016; Nitz et al. 2017). Each of these searches also searched for GW transients in low latency (Cannon et al. 2012; Adams et al. 2016; Nitz et al. 2018), as did the SPIIR pipeline (Chu et al. 2022); the online candidates are discussed more in Section 2.1.1. The cWB-BBH pipeline is a minimally modeled search that coherently analyzes the data from the network to identify transient signals, while GstLAL, MBTA, PyCBC, and SPIIR use matched filtering to correlate the data with CBC waveform templates. Additional differences are detailed in Abac et al. (2026b).

2.1. *Search results*

While there are many potential sources of transient GWs, all of the high-significance candidates identified to date by the LVK analyses are consistent with being CBCs (Abbott et al. 2017b, 2019c, 2021c; Abac et al. 2025d). We therefore limit the GWTC-5.0 candidate list to search results for potential BBHs, NSBHs and BNSs. Following GWTC-4.0 (Abac et al. 2025), we down-select candidates found by at least one pipeline based on the probability of astrophysical origin p_{astro} and FAR, which is a measure of its detection significance defined by the estimated rate of non-astrophysical (noise) events found by a pipeline with a rank at least as high as the candidate. Both p_{astro} and FAR depend on the specific noise background seen by each pipeline, and also incorporate assumptions on the (absolute or relative) astrophysical rates of signals for different binary sources. The p_{astro} calculation also depends on the sensitivity of the searches to CBC signals, which varies across the source parameter space. This, coupled with methodological differences in estimating the noise background, can lead to significant differences in estimated FAR and p_{astro} across pipelines. Such differences are more pronounced for candidates of marginal significance, as well as those with inferred properties (under the assumption of astrophysical origin) lying outside the range of previously observed sources (Abbott et al. 2023a; Abac et al. 2025a).

Given such systematic variability over pipelines, we sort candidates into three disjoint sets. First, candidates with both FAR $< 1\,\mathrm{yr}^{-1}$ and $p_{\mathrm{astro}} \geq 0.5$ in one or more pipelines. Second, candidates with $p_{\mathrm{astro}} \geq 0.5$ in one or more pipelines but FAR $\geq 1\,\mathrm{yr}^{-1}$ in all pipelines. Third, subthreshold candidates with $p_{\mathrm{astro}} < 0.5$ in all pipelines. There is no GW candidate with a FAR $< 1\,\mathrm{yr}^{-1}$ and $p_{\mathrm{astro}} < 0.5$ in all pipelines.

All candidates identified in GW data by the search pipelines are named with a *GW* prefix (Abac et al. 2026a). Those GW candidates found in O4b with a FAR $< 1\,\mathrm{yr}^{-1}$ in at least one pipeline, and for which $p_{\mathrm{astro}} \geq 0.5$, can be found in Table 1 alongside their FAR, SNR, and p_{astro}. Their individual detector SNRs are reported in Table 8 of Appendix B. Of these, 75 candidates are found in periods when all three detectors (HLV) were operating, and 29 during any two-detector combination (HL, HV or LV). We carry out event validation for this higher-purity subset of candidates (Abac et al. 2026b), and for those that pass validation we estimate their source properties, which we report in Section 3. In O4b, all events in the higher-purity subset of candidates passed the event validation. In addition, we list all other candidates assigned $p_{\mathrm{astro}} \geq 0.5$ by at least one pipeline in Table 2, and discuss the remaining subthreshold candidates in Section 2.1.4.

2.1.1. *Online candidates*

As mentioned above, in O4b five pipelines conducted online searches for CBCs. These searches distributed Notices via General Coordinates Network (GCN; NASA 2025) and SCiMMA Hopskotch (SCiMMA 2025) for 1820 GW candidates with a FAR $< 2\,\mathrm{d}^{-1}$. Of these, 114 passed a stricter threshold of FAR < 1 per $30\,\mathrm{d}$ after applying a trials factor to account for the number of simultaneous searches (LIGO–Virgo–KAGRA Collaboration 2025); these candidates were reported as high-significance candidates. The high-significance candidates underwent human vetting (LIGO–Virgo–KAGRA Collaboration 2025; Soni et al. 2025), and additional information was disseminated via GCN Circulars. These alerts facilitated rapid searches for potential electromagnetic counterparts to transient GWs.

The online searches run in near real time and are only able to use data collected up to the current time. Data quality can vary suddenly and noise transients in the detectors can be mistakenly identified as astrophysical in origin. Of the 114 high-significance candidates identified in low latency, 9 were later retracted. Of these 9 retractions, 3 were due to triggers from early-warning search pipelines (Sachdev et al. 2020; Alléné et al. 2025; Nitz et al. 2020a; Kovalam et al. 2022) that did not have corresponding triggers in the full-bandwidth searches. The other 6 retracted candidates were all found to be significant by only one pipeline. None of the 9 retracted online candidates were recovered with a FAR $< 2\,\mathrm{d}^{-1}$ in the offline searches.

Table 1. Candidate GW signals from O4b with a FAR $< 1\,\mathrm{yr}^{-1}$ in at least one pipeline and for which $p_{\mathrm{astro}} \geq 0.5$.

Candidate	Inst.	cWB-BBH			GstLAL			MBTA			PyCBC		
		FAR (yr^{-1})	SNR	p_{astro}	FAR (yr^{-1})	SNR	p_{astro}	FAR (yr^{-1})	SNR	p_{astro}	FAR (yr^{-1})	SNR	p_{astro}
GW240406_062847	HL	–	–	–	$< 1.0 \times 10^{-5}$	11.2	> 0.99	1.5×10^{-5}	11.1	> 0.99	6.2×10^{-5}	11.3	> 0.99
GW240413_022019	HLV	0.028	12.9	> 0.99	$< 1.0 \times 10^{-5}$	17.1	> 0.99	$< 1.0 \times 10^{-5}$	18.1	> 0.99	4.5×10^{-5}	17.5	> 0.99
GW240414_054515	HV	–	–	–	0.0026	10.7	> 0.99	0.0028	11.2	> 0.99	5.3×10^{-5}	10.8	> 0.99
GW240420_175625	H	–	–	–	*350*	*10.0*	*0.02*	–	–	–	0.078	9.9	0.98
GW240426_031451	HL	0.0046	10.3	> 0.99	0.0011	9.4	> 0.99	0.20	9.9	0.96	3.8×10^{-5}	9.8	> 0.99
GW240428_225440	HV	–	–	–	$< 1.0 \times 10^{-5}$	15.5	> 0.99	$< 1.0 \times 10^{-5}$	15.6	> 0.99	2.6×10^{-5}	15.5	> 0.99
GW240501_033534	HLV	0.0035	10.4	> 0.99	$< 1.0 \times 10^{-5}$	10.2	> 0.99	0.0029	10.6	> 0.99	3.2×10^{-5}	10.0	> 0.99
GW240505_133552	HLV	0.45	9.2	0.97	0.13	8.7	0.98	*4.8*	*9.4*	*0.59*	0.97	8.0	0.94
GW240507_041632	HLV	–	–	–	5.7×10^{-4}	10.2	> 0.99	0.85	10.2	0.88	2.5×10^{-4}	9.4	> 0.99
GW240511_031507	HLV	0.0013	16.2	> 0.99	$< 1.0 \times 10^{-5}$	15.9	> 0.99	$< 1.0 \times 10^{-5}$	16.3	> 0.99	4.9×10^{-5}	15.7	> 0.99
GW240512_024139	HLV	–	–	–	$< 1.0 \times 10^{-5}$	11.1	> 0.99	$< 1.0 \times 10^{-5}$	11.6	> 0.99	4.9×10^{-5}	10.5	> 0.99
GW240513_183302	HLV	0.0013	13.8	> 0.99	$< 1.0 \times 10^{-5}$	14.5	> 0.99	$< 1.0 \times 10^{-5}$	14.0	> 0.99	4.9×10^{-5}	14.0	> 0.99
GW240514_121713	HLV	0.0013	16.9	> 0.99	$< 1.0 \times 10^{-5}$	15.6	> 0.99	$< 1.0 \times 10^{-5}$	16.2	> 0.99	4.9×10^{-5}	15.6	> 0.99
GW240515_005301	HLV	*8.1*	*12.8*	*0.55*	$< 1.0 \times 10^{-5}$	11.6	> 0.99	*3.1*	*11.1*	*0.70*	7.3×10^{-4}	10.4	> 0.99
GW240519_012815	LV	–	–	–	0.30	10.3	0.96	–	–	–	0.014	10.6	> 0.99
GW240520_213616	HLV	–	–	–	$< 1.0 \times 10^{-5}$	11.6	> 0.99	$< 1.0 \times 10^{-5}$	11.9	> 0.99	6.8×10^{-5}	11.2	> 0.99
GW240525_031210	HLV	–	–	–	0.29	9.1	0.97	*15*	*9.0*	*0.34*	*1.4*	*8.2*	*0.90*
GW240526_093944	HLV	–	–	–	–	–	–	0.14	9.7	0.97	–	–	–
GW240527_183429	HLV	0.0013	10.4	> 0.99	0.0012	9.4	> 0.99	0.18	9.7	0.97	1.7×10^{-4}	9.9	> 0.99
GW240527_230910	HLV	*1.1*	*9.3*	*0.89*	0.053	10.6	> 0.99	1.4×10^{-5}	11.0	> 0.99	0.0071	9.7	> 0.99
GW240530_012417	HLV	*88*	*9.4*	*0.06*	$< 1.0 \times 10^{-5}$	10.8	> 0.99	$< 1.0 \times 10^{-5}$	10.6	> 0.99	8.4×10^{-4}	10.0	> 0.99
GW240531_040326	HLV	–	–	–	*1.8*	*9.1*	*0.84*	–	–	–	0.87	8.7	0.95
GW240531_075248	HLV	*19*	*8.9*	*0.29*	0.012	9.0	> 0.99	0.049	9.3	0.99	0.0039	9.2	> 0.99
GW240601_061200	HL	0.082	10.0	0.99	*2.0*	*8.6*	*0.83*	*3.4*	*9.2*	*0.67*	*1.3*	*8.5*	*0.93*
GW240601_231004	HLV	–	–	–	0.022	9.9	> 0.99	2.6×10^{-5}	10.4	> 0.99	0.0032	10.1	> 0.99
GW240612_081540	HLV	*34*	*9.9*	*0.16*	*51*	*8.1*	*0.19*	0.56	8.4	0.88	0.91	8.2	0.92
GW240615_113620	HLV	0.0012	25.8	> 0.99	$< 1.0 \times 10^{-5}$	25.8	> 0.99	$< 1.0 \times 10^{-5}$	26.4	> 0.99	4.9×10^{-5}	26.4	> 0.99
GW240615_160735	HLV	*1.6*	*13.1*	*0.85*	2.8×10^{-5}	10.5	> 0.99	6.1×10^{-4}	10.6	> 0.99	5.0×10^{-5}	10.7	> 0.99
GW240618_071627	HL	0.83	8.7	0.89	0.16	8.0	0.98	0.28	8.2	0.93	*6.1*	*8.0*	*0.70*
GW240621_195059	HLV	0.0012	28.2	> 0.99	$< 1.0 \times 10^{-5}$	27.2	> 0.99	$< 1.0 \times 10^{-5}$	27.9	> 0.99	2.5×10^{-5}	27.2	> 0.99
GW240621_200935	HLV	0.0012	10.7	> 0.99	0.0022	9.7	> 0.99	0.11	10.3	0.97	0.011	9.9	> 0.99
GW240621_214041	HLV	*18*	*7.6*	*0.34*	*1.6*	*7.9*	*0.86*	*1.6*	*7.9*	*0.74*	0.038	7.9	> 0.99
GW240622_004008	HLV	0.37	9.9	0.96	$< 1.0 \times 10^{-5}$	12.5	> 0.99	$< 1.0 \times 10^{-5}$	12.7	> 0.99	2.5×10^{-5}	12.6	> 0.99

Table 1 *continued*

Table 1 *(continued)*

Candidate	Inst.	cWB-BBH			GstLAL			MBTA			PyCBC		
		FAR (yr^{-1})	SNR	p_{astro}	FAR (yr^{-1})	SNR	p_{astro}	FAR (yr^{-1})	SNR	p_{astro}	FAR (yr^{-1})	SNR	p_{astro}
GW240627_131622	HLV	–	–	–	0.33	9.8	0.96	0.087	9.8	0.97	0.16	9.3	0.99
GW240629_145256	HLV	–	–	–	$< 1.0 \times 10^{-5}$	12.6	> 0.99	$< 1.0 \times 10^{-5}$	12.7	> 0.99	2.5×10^{-5}	12.5	> 0.99
GW240630_101703	HLV	0.058	10.6	> 0.99	1.5×10^{-5}	10.2	> 0.99	0.0017	10.1	> 0.99	4.1×10^{-5}	9.9	> 0.99
GW240703_191355	LV	–	–	–	$< 1.0 \times 10^{-5}$	10.1	> 0.99	–	–	–	0.38	9.8	> 0.99
GW240705_053215	HLV	0.0013	16.8	> 0.99	$< 1.0 \times 10^{-5}$	14.0	> 0.99	$< 1.0 \times 10^{-5}$	15.3	> 0.99	7.9×10^{-5}	15.2	> 0.99
GW240716_034900	LV	–	–	–	$< 1.0 \times 10^{-5}$	12.9	> 0.99	–	–	–	*3.5*	*11.7*	*0.80*
GW240824_205609	HLV	0.25	8.6	0.96	*3.1*	*8.4*	*0.77*	*7.8*	*9.0*	*0.46*	*2.4*	*7.7*	*0.87*
GW240825_055146	HLV	–	–	–	0.036	9.8	> 0.99	2.0×10^{-5}	10.3	> 0.99	0.0027	9.7	> 0.99
GW240830_211120	HLV	–	–	–	1.2×10^{-4}	11.1	> 0.99	$< 1.0 \times 10^{-5}$	11.1	> 0.99	6.5×10^{-5}	10.8	> 0.99
GW240902_143306	HLV	*5.1*	*9.5*	*0.50*	$< 1.0 \times 10^{-5}$	10.6	> 0.99	0.0016	10.6	> 0.99	1.5×10^{-4}	10.3	> 0.99
GW240907_153833	HLV	0.0023	10.5	> 0.99	0.0082	9.4	> 0.99	0.0026	10.0	> 0.99	8.0×10^{-5}	9.7	> 0.99
GW240908_082628	HLV	0.0069	9.8	> 0.99	1.2×10^{-5}	11.1	> 0.99	8.2×10^{-4}	10.9	> 0.99	4.4×10^{-5}	9.6	> 0.99
GW240908_125134	HLV	–	–	–	0.29	8.4	0.97	1.00	8.6	0.85	*1.9*	*7.8*	*0.88*
GW240910_103535	HL	0.0011	15.5	> 0.99	$< 1.0 \times 10^{-5}$	17.8	> 0.99	$< 1.0 \times 10^{-5}$	17.8	> 0.99	$< 1.0 \times 10^{-5}$	17.8	> 0.99
GW240915_001357	HLV	0.0011	16.2	> 0.99	$< 1.0 \times 10^{-5}$	15.0	> 0.99	$< 1.0 \times 10^{-5}$	16.4	> 0.99	3.5×10^{-5}	15.9	> 0.99
GW240915_105151	HV	–	–	–	$< 1.0 \times 10^{-5}$	13.8	> 0.99	–	–	–	0.12	13.9	> 0.99
GW240916_184352	HLV	–	–	–	0.54	9.5	0.94	0.028	9.8	> 0.99	0.53	9.1	0.96
GW240919_061559	HLV	0.0011	16.2	> 0.99	$< 1.0 \times 10^{-5}$	16.5	> 0.99	$< 1.0 \times 10^{-5}$	16.9	> 0.99	3.9×10^{-5}	16.5	> 0.99
GW240920_073424	HLV	0.0011	14.0	> 0.99	$< 1.0 \times 10^{-5}$	12.6	> 0.99	$< 1.0 \times 10^{-5}$	13.1	> 0.99	3.9×10^{-5}	12.9	> 0.99
GW240920_124024	HL	0.0011	37.4	> 0.99	$< 1.0 \times 10^{-5}$	36.6	> 0.99	$< 1.0 \times 10^{-5}$	36.8	> 0.99	$< 1.0 \times 10^{-5}$	36.9	> 0.99
GW240921_201835	LV	–	–	–	1.4×10^{-4}	11.0	> 0.99	$< 1.0 \times 10^{-5}$	11.3	> 0.99	0.19	10.5	> 0.99
GW240922_142106	HLV	*10*	*11.3*	*0.47*	$< 1.0 \times 10^{-5}$	12.1	> 0.99	$< 1.0 \times 10^{-5}$	12.5	> 0.99	3.9×10^{-5}	11.7	> 0.99
GW240923_204006	HLV	0.0011	13.6	> 0.99	$< 1.0 \times 10^{-5}$	11.5	> 0.99	3.5×10^{-5}	12.4	> 0.99	9.1×10^{-5}	11.8	> 0.99
GW240924_000316	HLV	0.0011	11.4	> 0.99	2.0×10^{-5}	10.4	> 0.99	0.0076	10.2	> 0.99	0.0058	9.0	> 0.99
GW240925_005809	HLV	0.0011	29.6	> 0.99	$< 1.0 \times 10^{-5}$	30.6	> 0.99	$< 1.0 \times 10^{-5}$	31.2	> 0.99	3.9×10^{-5}	31.0	> 0.99
GW240930_035959	HLV	0.0011	15.6	> 0.99	$< 1.0 \times 10^{-5}$	15.3	> 0.99	$< 1.0 \times 10^{-5}$	16.1	> 0.99	3.9×10^{-5}	15.4	> 0.99
GW240930_234614	HL	0.24	11.3	0.98	–	–	–	–	–	–	–	–	–
GW241002_030559	LV	–	–	–	$< 1.0 \times 10^{-5}$	11.5	> 0.99	$< 1.0 \times 10^{-5}$	11.9	> 0.99	0.064	11.4	> 0.99
GW241006_015333	HLV	0.0016	17.6	> 0.99	$< 1.0 \times 10^{-5}$	16.5	> 0.99	$< 1.0 \times 10^{-5}$	16.9	> 0.99	9.9×10^{-5}	16.5	> 0.99
GW241007_082943	HLV	0.042	9.5	> 0.99	*1.1*	*9.4*	*0.90*	0.094	9.8	0.97	*1.3*	*9.1*	*0.98*
GW241009_022835	HLV	–	–	–	0.99	8.3	0.91	*18*	*8.3*	*0.26*	0.97	8.4	> 0.99
GW241009_084816	HLV	–	–	–	$< 1.0 \times 10^{-5}$	11.4	> 0.99	$< 1.0 \times 10^{-5}$	12.1	> 0.99	9.9×10^{-5}	11.8	> 0.99
GW241009_220455	HLV	–	–	–	0.072	9.7	> 0.99	0.023	10.0	> 0.99	0.54	10.0	> 0.99
GW241011_233834	HV	–	–	–	$< 1.0 \times 10^{-5}$	34.6	> 0.99	$< 1.0 \times 10^{-5}$	35.6	> 0.99	2.4×10^{-5}	35.8	> 0.99
GW241101_220523	LV	–	–	–	5.5×10^{-4}	10.6	> 0.99	–	–	–	*12*	*10.4*	*0.85*

Table 1 *continued*

Table 1 *(continued)*

Candidate	Inst.	cWB-BBH			GstLAL			MBTA			PyCBC		
		FAR (yr^{-1})	SNR	p_{astro}	FAR (yr^{-1})	SNR	p_{astro}	FAR (yr^{-1})	SNR	p_{astro}	FAR (yr^{-1})	SNR	p_{astro}
GW241102_124058	HLV	0.0013	19.9	> 0.99	$< 1.0 \times 10^{-5}$	21.0	> 0.99	$< 1.0 \times 10^{-5}$	21.7	> 0.99	7.0×10^{-5}	21.4	> 0.99
GW241102_144729	HLV	0.0013	12.7	> 0.99	$< 1.0 \times 10^{-5}$	11.9	> 0.99	1.2×10^{-4}	12.2	> 0.99	7.0×10^{-5}	11.4	> 0.99
GW241109_033317	LV	–	–	–	0.0013	10.9	> 0.99	0.0020	11.3	> 0.99	0.30	10.9	> 0.99
GW241109_115924	HV	–	–	–	1.2×10^{-4}	11.8	> 0.99	0.0011	11.9	> 0.99	0.16	11.7	> 0.99
GW241110_124123	HLV	–	–	–	0.10	10.1	0.99	0.10	10.2	0.97	6.3×10^{-4}	10.1	> 0.99
GW241111_111552	HL	0.0013	16.3	> 0.99	$< 1.0 \times 10^{-5}$	15.6	> 0.99	$< 1.0 \times 10^{-5}$	15.9	> 0.99	1.4×10^{-5}	15.3	> 0.99
GW241113_163507	LV	–	–	–	$< 1.0 \times 10^{-5}$	12.5	> 0.99	–	–	–	0.29	12.5	> 0.99
GW241114_024711	HLV	0.0013	11.3	> 0.99	$< 1.0 \times 10^{-5}$	10.7	> 0.99	*1.4*	*10.4*	*0.78*	1.1×10^{-4}	10.2	> 0.99
GW241114_235258	LV	–	–	–	$< 1.0 \times 10^{-5}$	12.4	> 0.99	–	–	–	0.049	11.6	> 0.99
GW241116_151753	HLV	0.025	9.9	> 0.99	0.45	9.8	0.95	0.023	10.5	> 0.99	0.0044	9.0	> 0.99
GW241124_024914	HLV	*14*	*8.5*	*0.46*	*5.5*	*8.5*	*0.65*	*7.1*	*8.7*	*0.48*	0.78	8.5	0.94
GW241125_010116	HLV	0.0013	11.0	> 0.99	1.1×10^{-5}	10.0	> 0.99	0.067	10.5	0.98	5.4×10^{-5}	9.9	> 0.99
GW241127_061008	HLV	0.0013	31.3	> 0.99	$< 1.0 \times 10^{-5}$	29.8	> 0.99	$< 1.0 \times 10^{-5}$	31.2	> 0.99	5.3×10^{-5}	30.7	> 0.99
GW241129_021832	HLV	0.0013	16.7	> 0.99	$< 1.0 \times 10^{-5}$	16.1	> 0.99	$< 1.0 \times 10^{-5}$	16.3	> 0.99	5.3×10^{-5}	15.7	> 0.99
GW241130_034908	HLV	0.0013	13.2	> 0.99	$< 1.0 \times 10^{-5}$	13.4	> 0.99	$< 1.0 \times 10^{-5}$	13.8	> 0.99	5.3×10^{-5}	12.9	> 0.99
GW241130_110422	HLV	–	–	–	0.26	9.7	0.97	5.5×10^{-4}	10.3	> 0.99	0.014	9.7	> 0.99
GW241201_055758	HLV	*7.7*	*8.9*	*0.59*	0.83	8.7	0.92	*27*	*9.0*	*0.19*	*4.9*	*7.5*	*0.73*
GW241210_060606	HLV	0.0012	13.4	> 0.99	$< 1.0 \times 10^{-5}$	12.4	> 0.99	$< 1.0 \times 10^{-5}$	12.6	> 0.99	5.1×10^{-5}	12.4	> 0.99
GW241210_120900	HL	*1.9*	*8.9*	*0.86*	0.28	8.5	0.97	*4.4*	*9.0*	*0.65*	*6.3*	*8.3*	*0.70*
GW241225_042553	LV	–	–	–	$< 1.0 \times 10^{-5}$	16.5	> 0.99	–	–	–	0.034	16.4	> 0.99
GW241225_082815	HL	0.0012	19.5	> 0.99	$< 1.0 \times 10^{-5}$	17.5	> 0.99	3.0×10^{-5}	17.9	> 0.99	$< 1.0 \times 10^{-5}$	17.8	> 0.99
GW241229_155844	HLV	*10*	*8.0*	*0.55*	*2.3*	*8.7*	*0.81*	*10.0*	*8.4*	*0.50*	0.083	7.9	> 0.99
GW241230_084504	LV	–	–	–	$< 1.0 \times 10^{-5}$	11.1	> 0.99	–	–	–	–	–	–
GW241230_233618	HLV	0.96	12.2	0.92	0.48	10.4	0.95	–	–	–	–	–	–
GW241231_054133	HLV	0.0012	16.8	> 0.99	$< 1.0 \times 10^{-5}$	17.2	> 0.99	$< 1.0 \times 10^{-5}$	17.4	> 0.99	2.8×10^{-5}	16.7	> 0.99
GW250101_011205	HLV	–	–	–	0.020	9.7	> 0.99	0.35	9.8	0.94	0.52	9.0	0.97
GW250104_015122	HLV	0.0012	12.1	> 0.99	$< 1.0 \times 10^{-5}$	11.3	> 0.99	0.0099	11.6	> 0.99	1.5×10^{-4}	11.4	> 0.99
GW250108_152221	HLV	0.0012	11.8	> 0.99	1.5×10^{-4}	11.2	> 0.99	2.4×10^{-4}	11.5	> 0.99	0.0016	11.1	> 0.99
GW250109_010541	HLV	0.0012	13.1	> 0.99	$< 1.0 \times 10^{-5}$	12.0	> 0.99	0.0018	12.3	> 0.99	0.013	11.0	> 0.99
GW250109_074552	HV	–	–	–	0.42	10.7	0.95	*2.0*	*10.0*	*0.78*	*140*	*9.6*	*0.02*
GW250114_082203	HL	0.0012	72.8	> 0.99	$< 1.0 \times 10^{-5}$	76.6	> 0.99	$< 1.0 \times 10^{-5}$	78.6	> 0.99	2.0×10^{-5}	77.7	> 0.99
GW250116_015318	HLV	–	–	–	*87*	*8.0*	*0.11*	*240*	*7.9*	*0.03*	0.12	7.8	> 0.99
GW250118_023225	HLV	0.46	9.0	0.97	0.0035	9.0	> 0.99	*1.9*	*8.8*	*0.79*	0.033	8.5	> 0.99
GW250118_055802	HLV	*290*	*9.8*	*0.02*	0.18	10.5	0.98	0.0089	10.2	> 0.99	0.95	9.6	0.93
GW250118_170523	HL	0.0012	13.9	> 0.99	$< 1.0 \times 10^{-5}$	13.3	> 0.99	$< 1.0 \times 10^{-5}$	13.5	> 0.99	$< 1.0 \times 10^{-5}$	13.0	> 0.99

Table 1 *continued*

Table 1 *(continued)*

Candidate	Inst.	cWB-BBH			GstLAL			MBTA			PyCBC		
		FAR (yr^{-1})	SNR	p_{astro}	FAR (yr^{-1})	SNR	p_{astro}	FAR (yr^{-1})	SNR	p_{astro}	FAR (yr^{-1})	SNR	p_{astro}
GW250119_025138	HLV	0.0012	14.3	> 0.99	$< 1.0 \times 10^{-5}$	14.1	> 0.99	$< 1.0 \times 10^{-5}$	14.5	> 0.99	5.7×10^{-5}	13.8	> 0.99
GW250119_190238	HLV	0.0012	20.1	> 0.99	$< 1.0 \times 10^{-5}$	20.1	> 0.99	$< 1.0 \times 10^{-5}$	21.3	> 0.99	5.7×10^{-5}	20.1	> 0.99

NOTE— The date and time of each candidate is encoded in the name as GWYYMMDD_hhmmss. The names of candidates not previously reported in online are given in **bold**. The detectors that were observing at the time of each transient are denoted by a single-letter (e.g., H for LIGO Hanford). This does not necessarily indicate that the same detectors contributed triggers for a given candidate. We include results from search pipelines that observe a candidate with a FAR $\geq 1\,\mathrm{yr}^{-1}$ in *italics*. A dash (–) indicates that a candidate was not found by a pipeline. FARs have been capped at $1 \times 10^{-5}\,\mathrm{yr}^{-1}$ to maintain a consistent limiting FAR across pipelines.

Out of the significant online candidates that were not retracted, 11 were identified with a FAR $\geq 1\,\mathrm{yr}^{-1}$ in the offline search:

- Candidates with $p_{\mathrm{astro}} \geq 0.5$, shown in Table 2, are likely of astrophysical origin: GW241210_023335, GW240917_130237, GW240813_034548, GW240807_214559, GW240430_093517 and GW240421_052935.

- Candidates with $p_{\mathrm{astro}} < 0.5$: S240426dl and S240422ed. S240426dl was found confidently only by cWB with a FAR $< 1.6\,\mathrm{yr}^{-1}$ in low latency, while other pipelines reported it as a sub-threshold trigger. Afterwards, this candidate was not recovered with a FAR $< 1\,\mathrm{yr}^{-1}$ in the offline search by any pipeline. S240422ed was found by GstLAL with a FAR $< 1 \times 10^{-5}\,\mathrm{yr}^{-1}$ in low latency, but later this was found less significant with a FAR < 1 per $35\,\mathrm{d}$ (LIGO Scientific Collaboration et al. 2024) after collecting more background data and reevaluating the significance because the additional background data in the SNR–ξ^2 histogram populated the parameter space near the candidate's point estimates (Abac et al. 2026b).

- Candidates with a FAR $\geq 2\,\mathrm{d}^{-1}$ and hence not included in this catalog: S241122a, S240813d and S240514c. Similar to S240422ed, all of these events were found by GstLAL online but updated to be less significant by its offline search with more accurate background statistics.

One of the significant online candidates in Table 1, GW240406_062847, was detected during the pre-O4b engineering run with a FAR $< 1\,\mathrm{yr}^{-1}$ as well as in the offline searches by GstLAL, MBTA, and PyCBC. Due to the less detailed information available about detector calibration during the engineering run, we do not currently include a estimate of the candidate's source properties comparable to that for other candidates in Section 3; based only on information from search pipelines, point estimates of the primary mass and the secondary for this candidate are 42.60 $M_{\odot}$and 17.71 $M_{\odot}$, respectively, which indicates the source would likely be a BBH.

2.1.2. *New offline candidates*

There are 23 candidates identified with $p_{\mathrm{astro}} \geq 0.5$ by at least one pipeline in the offline search that were not identified in low latency and not previously shared via GCN or SCiMMA Hopskotch Notices or GCN Circulars. These new candidates are indicated in bold in Tables 1 and 2.

The majority are of low significance (FAR $\geq 1\,\mathrm{yr}^{-1}$) and are listed in Table 2. All of the new candidates have moderate network SNRs ($\lesssim 10$). Of the 23 new candidates, 20 are coincident triggers contributed from two or more of LHO, LLO and Virgo, 12 events of which involve Virgo in their coincident detections, while there is no event found only by Virgo (see Tables 1 and 2).

Table 2. Candidate GW signals from O4b with $p_{\rm astro} \geq 0.5$ in at least one pipeline and FAR $\geq 1\,{\rm yr}^{-1}$ in all pipelines.

Candidate	Inst.	cWB-BBH			GstLAL			MBTA			PyCBC		
		FAR ($\rm yr^{-1}$)	SNR	$p_{\rm astro}$	FAR ($\rm yr^{-1}$)	SNR	$p_{\rm astro}$	FAR ($\rm yr^{-1}$)	SNR	$p_{\rm astro}$	FAR ($\rm yr^{-1}$)	SNR	$p_{\rm astro}$
GW240407_040938	HLV	–	–	–	*18*	*7.8*	*0.36*	*3.5*	*8.5*	*0.67*	*1.8*	*7.5*	*0.91*
GW240407_061416	HLV	–	–	–	*2.7*	*8.8*	*0.78*	*25*	*8.7*	*0.24*	*3.6*	*7.9*	*0.78*
GW240407_214946	HL	–	–	–	–	–	–	–	–	–	*4.2*	*7.5*	*0.79*
GW240408_081753	HL	–	–	–	–	–	–	*4.4*	*8.3*	*0.61*	–	–	–
GW240411_074140	HL	–	–	–	*24*	*8.0*	*0.29*	*3.4*	*8.2*	*0.68*	–	–	–
GW240419_041206	HL	*3.4*	*9.1*	*0.71*	–	–	–	–	–	–	–	–	–
GW240421_052935	HL	*2.7*	*8.5*	*0.77*	*8.5*	*7.5*	*0.55*	–	–	–	–	–	–
GW240426_085802	HLV	–	–	–	*180*	*8.0*	*0.05*	*4.2*	*8.2*	*0.63*	*120*	*7.3*	*0.12*
GW240430_093517	HL	*2.7*	*8.7*	*0.77*	*1.3*	*8.1*	*0.88*	–	–	–	*150*	*8.2*	*0.10*
GW240509_102351	HLV	–	–	–	–	–	–	–	–	–	*2.0*	*8.2*	*0.89*
GW240512_051606	HLV	–	–	–	–	–	–	*3.1*	*9.4*	*0.70*	–	–	–
GW240516_041939	HLV	–	–	–	–	–	–	*3.4*	*9.0*	*0.67*	–	–	–
GW240525_201644	HLV	–	–	–	*2.3*	*9.0*	*0.81*	–	–	–	*8.0*	*8.9*	*0.69*
GW240527_150907	HLV	–	–	–	*2.2*	*9.2*	*0.81*	–	–	–	–	–	–
GW240611_214835	LV	–	–	–	*170*	*7.9*	*0.05*	*50*	*8.2*	*0.09*	*1.7*	*8.9*	*0.61*
GW240613_011503	HLV	–	–	–	*3.7*	*8.3*	*0.74*	–	–	–	–	–	–
GW240619_044535	HLV	–	–	–	*43*	*9.3*	*0.21*	*6.2*	*9.1*	*0.44*	*5.1*	*7.9*	*0.75*
GW240619_212357	HLV	*300*	*8.5*	*0.01*	*10*	*8.4*	*0.51*	–	–	–	–	–	–
GW240620_094631	HLV	*5.4*	*8.6*	*0.61*	*30*	*8.3*	*0.26*	*2.1*	*8.5*	*0.68*	*180*	*7.7*	*0.08*
GW240621_103457	HLV	*68*	*8.6*	*0.10*	*10*	*7.7*	*0.51*	*56*	*8.2*	*0.08*	–	–	–
GW240625_073331	HL	–	–	–	–	–	–	*2.5*	*10.1*	*0.64*	–	–	–
GW240630_115348	HLV	–	–	–	*14*	*8.5*	*0.42*	*51*	*8.2*	*0.09*	*6.5*	*8.3*	*0.67*
GW240630_212937	HLV	–	–	–	*600*	*8.2*	*0.01*	–	–	–	*4.9*	*7.3*	*0.75*
GW240701_011640	HLV	–	–	–	–	–	–	–	–	–	*12*	*7.8*	*0.51*
GW240701_013826	HLV	–	–	–	–	–	–	*2.5*	*10.4*	*0.64*	–	–	–
GW240701_203807	HLV	–	–	–	*8.6*	*7.8*	*0.55*	*160*	*7.9*	*0.03*	*220*	*7.6*	*0.08*
GW240806_043539	LV	–	–	–	*6.7*	*8.2*	*0.60*	*16*	*8.9*	*0.24*	*1.9*	*8.4*	*0.89*
GW240807_214559	LV	–	–	–	*310*	*9.6*	*0.03*	–	–	–	*17*	*9.0*	*0.66*
GW240813_034548	LV	–	–	–	*310*	*9.7*	*0.03*	–	–	–	*19*	*8.9*	*0.64*
GW240814_145043	LV	–	–	–	*39*	*9.3*	*0.22*	*2.1*	*9.4*	*0.74*	*23*	*9.4*	*0.13*
GW240828_102340	HLV	–	–	–	*450*	*8.0*	*0.02*	*3.8*	*8.0*	*0.62*	*690*	*7.7*	*0.03*
GW240901_195332	HLV	*24*	*9.4*	*0.27*	*7.8*	*8.4*	*0.57*	*730*	*8.5*	*< 0.01*	*9.6*	*7.7*	*0.62*
GW240907_092521	HLV	–	–	–	*4.0*	*8.3*	*0.72*	*120*	*7.9*	*0.05*	*15*	*7.6*	*0.55*
GW240907_121650	HLV	–	–	–	–	–	–	*6.0*	*9.8*	*0.52*	–	–	–
GW240908_174149	HLV	–	–	–	–	–	–	*3.1*	*9.0*	*0.67*	–	–	–

Table 2 *continued*

Table 2 *(continued)*

Candidate	Inst.	cWB-BBH			GstLAL			MBTA			PyCBC		
		FAR (yr^{-1})	SNR	p_{astro}	FAR (yr^{-1})	SNR	p_{astro}	FAR (yr^{-1})	SNR	p_{astro}	FAR (yr^{-1})	SNR	p_{astro}
GW240913_111216	HLV	–	–	–	*6.2*	*7.8*	*0.62*	–	–	–	–	–	–
GW240915_045510	HLV	*36*	*8.1*	*0.23*	*3.5*	*8.2*	*0.75*	*22*	*8.1*	*0.24*	*240*	*7.0*	*0.06*
GW240917_130237	HL	–	–	–	*1.8*	*7.7*	*0.85*	*22*	*7.8*	*0.23*	*7.0*	*7.6*	*0.63*
GW240919_215453	HL	*5.1*	*10.1*	*0.70*	–	–	–	–	–	–	–	–	–
GW240923_000715	HLV	–	–	–	–	–	–	*1.6*	*11.0*	*0.78*	–	–	–
GW240923_110846	H	–	–	–	–	–	–	–	–	–	*8.5*	*8.6*	*0.61*
GW240925_000956	HLV	–	–	–	*6.5*	*8.5*	*0.61*	–	–	–	–	–	–
GW240930_123408	HLV	–	–	–	*590*	*7.9*	*0.01*	*190*	*8.3*	*0.03*	*2.9*	*8.1*	*0.81*
GW241018_235402	H	–	–	–	–	–	–	–	–	–	*1.8*	*9.6*	*0.98*
GW241101_034726	HLV	–	–	–	*13*	*8.2*	*0.45*	*24*	*8.0*	*0.21*	*2.1*	*7.9*	*0.87*
GW241106_110932	HLV	–	–	–	*3.9*	*9.0*	*0.73*	*8.7*	*9.2*	*0.43*	–	–	–
GW241109_005349	HL	*7.4*	*10.5*	*0.56*	–	–	–	–	–	–	–	–	–
GW241129_140416	HL	–	–	–	–	–	–	–	–	–	*16*	*8.2*	*0.51*
GW241201_142737	HLV	–	–	–	*55*	*7.3*	*0.18*	–	–	–	*7.6*	*7.5*	*0.66*
GW241210_023335	HL	*710*	*7.8*	*< 0.01*	*1.9*	*7.8*	*0.84*	*13*	*7.7*	*0.43*	*2.0*	*7.5*	*0.87*
GW241219_222607	HL	*500*	*8.7*	*0.01*	*7.9*	*8.4*	*0.56*	*27*	*8.4*	*0.27*	*340*	*8.5*	*0.05*
GW241220_062146	HL	–	–	–	–	–	–	–	–	–	*9.4*	*7.9*	*0.57*
GW250105_134047	HLV	*160*	*8.7*	*0.04*	*10*	*8.0*	*0.51*	–	–	–	–	–	–
GW250109_083206	H	–	–	–	–	–	–	–	–	–	*1.4*	*10.5*	*> 0.99*
GW250116_051426	HL	–	–	–	*15*	*7.0*	*0.40*	*4.8*	*7.9*	*0.63*	*660*	*6.9*	*0.03*
GW250120_042414	HLV	–	–	–	*1.8*	*8.7*	*0.84*	*23*	*8.4*	*0.30*	*1.6*	*8.1*	*0.89*

NOTE— These candidates do not meet our criterion for source-property estimation, but are likely astrophysical in origin. The names of candidates not previously reported in online are given in **bold**. The date and time of each candidate is encoded in the name as GWYYMMDD_hhmmss. The detectors that were observing at the time of each transient are denoted by a single-letter (e.g., H for LIGO Hanford). This does not necessarily indicate that the same detectors contributed triggers for a given candidate. We include results from searches that observe a candidate with $p_{\mathrm{astro}} < 0.5$. *Italics* denote that the candidate was found with a FAR $\geq 1\,\mathrm{yr}^{-1}$. A dash (–) indicates that a candidate was not found by an pipeline.

2.1.3. *Pipeline consistency*

The search algorithms, methods, and configurations used differ between the search pipelines (Abac et al. 2026b), which causes them to have different responses to both noise and astrophysical transients. As a result, we expect candidate lists to differ between pipelines. There is less disagreement between pipelines for high-SNR candidates. Lower-SNR candidates, however, may be identified by only a subset of pipelines. Some candidates are observed in only one detector, which increases the uncertainty in significance estimation and can lead to additional disagreement across pipelines in both the estimated FAR and p_{astro}.

Not all of the 161 candidates with $p_{\mathrm{astro}} \geq 0.5$ were observed with $p_{\mathrm{astro}} \geq 0.5$ by all pipelines. Of these 161 candidates, 64 were found by cWB-BBH, 121 were found by GstLAL, 100 were found by MBTA, and 126 were found by PyCBC. Only 53 of these candidates were found by all pipelines, while 82 were found by all matched filter-based pipelines, 85 by three or more pipelines, and 112 by two or more pipelines. Of the 161 candidates for which $p_{\mathrm{astro}} \geq 0.5$ in any pipeline, several meet this criterion in only a single pipeline:

- The cWB-BBH pipeline found 4 unique candidates, one of which, GW240930_234614, was assigned FAR $< 1\,\mathrm{yr}^{-1}$, but was also not detected by any other pipeline. While this consideration might reduce our

confidence in the astrophysical origin of the candidate, cWB-BBH has the potential to detect BBH candidates impacted by physical effects neglected by the matched-filter searches, such as precession and eccentricity (e.g., Abac et al. 2024; Mishra et al. 2025). We discuss the parameter inference for GW240930_234614 in more detail, assuming an astrophysical origin, in Section 3.5.

- The GstLAL pipeline found 12 unique candidates, one of which, GW241230_084504, was highly significant with a FAR $< 1 \times 10^{-5}\,\mathrm{yr}^{-1}$; the remaining candidates are listed in Table 2.
- The MBTA pipeline found 14 unique candidates, one of which, GW240526_093944, was assigned a FAR $< 1\,\mathrm{yr}^{-1}$, with the others summarized in Table 2.
- The PyCBC pipeline found 19 unique candidates, one of which, GW240420_175625, was assigned a FAR $< 1\,\mathrm{yr}^{-1}$; additional candidates appear in Table 2.

2.1.4. *Subthreshold candidates*

We have highlighted 161 GW candidates in O4b with $p_{\mathrm{astro}} \geq 0.5$ as listed in Tables 1 and 2. These candidates are a subset of the O4b candidates in GWTC-5.0, which is comprised of 1886 triggers. The remaining 1725 subthreshold candidates in O4b have a FAR $< 2\,\mathrm{d}^{-1}$ and $p_{\mathrm{astro}} < 0.5$. These candidates are made publicly available at Gravitational Wave Open Science Center (GWOSC; Abac et al. 2026c) for completeness, but the possibility that these are of instrumental origin has not been examined. Following the formalism outlined in Abbott et al. (2023a); Abac et al. (2026b), we also estimate the number of astrophysical signals among the set of 1725 subthreshold candidates. Using the p_{astro} values in each pipeline and their relative sensitivities to simulated signals, as described below, we expect approximately 32 true signals among the subthreshold candidates in total. This implies that the purity of this sample is expected to be low: 0.019 when considering all of the subthreshold candidates, an estimate comparable to that obtained for O4a as discussed in Appendix A.

2.2. *Search sensitivity*

Here we describe the estimated sensitivity of each search pipeline, calculated by adding simulated CBC signals to the data and running search pipelines to recover them. These simulated signals are referred to as *injections*. We parameterize the sensitivity of the searches via the estimated time–volume product or hypervolume $\langle VT \rangle$ (Abac et al. 2026a). As discussed further in Abac et al. (2026b), the number of astrophysical signals, $\hat{N}$, that a pipeline is expected to detect can be estimated as

$$\hat{N} = \langle VT \rangle \mathcal{R}\,, \tag{1}$$

where $\mathcal{R}$ is the volumetric rate of mergers per unit (source-frame) time. To estimate $\langle VT \rangle$ for each pipeline, we simulate a distribution of signals that approximates the detected population of BBHs, NSBHs and BNSs (Essick et al. 2025). To estimate the overall catalog sensitivity, each pipeline analyzes the same set of simulated signals: the injections are added into the collected data, and we record how many are recovered significantly.

As in Abbott et al. (2023a), several combinations of masses are used to assess our sensitivity to BBH, NSBH, and BNS systems. We thus estimate $\langle VT \rangle$ at a set of fiducial points in the component mass space:

- BHs at $35M_\odot$. These correspond to GW150914-like systems (Abbott et al. 2016b, 2024). This is also approximately where we see a feature in the BH mass spectrum (Abac et al. 2026d).
- BHs at $5M_\odot$, $10M_\odot$, $20M_\odot$, $60M_\odot$, and $100M_\odot$. These lie within the range of previously detected BH masses (Abbott et al. 2023a).
- NSs at $1.5M_\odot$, which is consistent with the distribution of known NS masses (Antoniadis et al. 2016; Alsing et al. 2018; Özel & Freire 2016; Farrow et al. 2019; Landry & Read 2021; Abbott et al. 2023b).

For each given point, injections are weighted so that they follow a log-normal distribution about the central mass with a width of 0.1 in logarithmic space (Essick et al. 2025). Figure 1 shows the resulting variation in the O4b $\langle VT \rangle$ with a detection threshold of FAR $< 1\,\mathrm{yr}^{-1}$ across the component mass parameter space for each search.

Similar to GWTC-4.0 (Abac et al. 2025a) and previous catalogs, the results at the top-left panel of Figure 1, labelled as *O4b Any*, represent our overall sensitivity for the latest observing run (O4b) to CBCs in the specified region. Additionally, at the top-right panel we include the sensitivity estimates accumulated across all the observing runs to date, labelled as *All Cumulative*. They are derived by taking the minimum FAR for an injection from all of the pipelines or by considering a semi-analytic injection whose phase-maximized network SNR larger than 10 for the first observing run (O1) and the second observing run (O2). The sensitivity is greatest for the *Any* pipeline (the top-left panel) for $100M_\odot + 100M_\odot$ binaries, though different pipelines are more or less sensitive to different regions of the binary parameter space. Only sensitivity estimates that have an uncertainty smaller than 25% are shown in Figure 1. The method of estimating $\langle VT \rangle$ uncertainty has been changed since GWTC-4.0, and the new upper limit on relative uncertainty is set to be broadly consistent with the GWTC-4.0's estimates (Abac et al. 2026b). Compared to the sensitivity estimates using the O4a data (Abac et al. 2025a), we find that the sensitivity of O4b has improved by approximately 20%, which can be attributed to several factors: a longer duration for O4b; the addition of Virgo detector; better noise sensitivity of individual detectors, and improvement of search pipelines. Furthermore, the sensitivity of O4a and O4b combined accounts for approximately 75% of the total sensitivity accumulated across all observing runs.

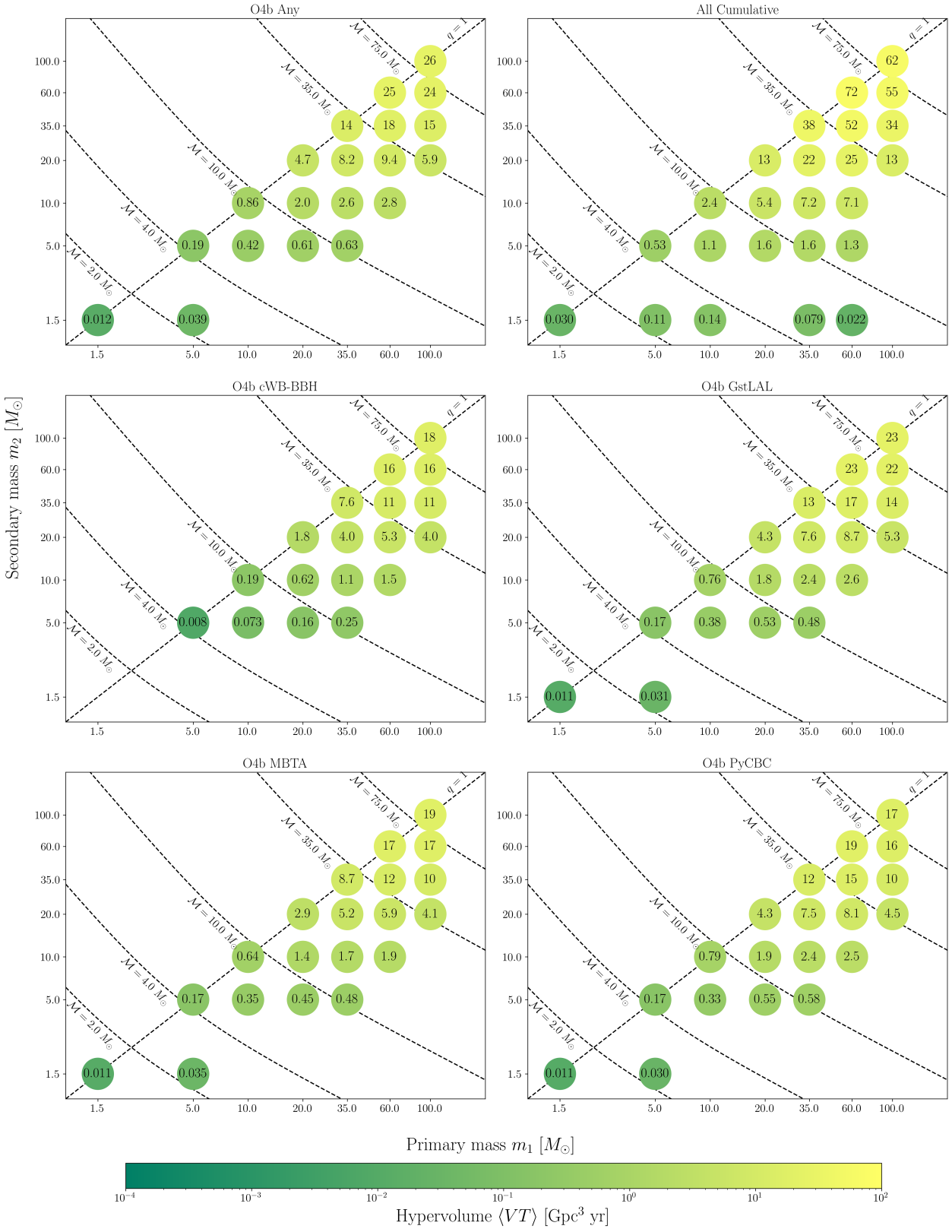

Figure 1. The sensitive hypervolume $\langle VT \rangle$ for searches of O4b data applying a significance threshold FAR $< 1\,\mathrm{yr}^{-1}$, evaluated at points in component mass space. The *O4b Any* results come from calculating the $\langle VT \rangle$ for injections found by at least one search pipeline, while the *All Cumulative* results refer to the $\langle VT \rangle$ accumulated across all observing runs to date by applying an alternative threshold SNR > 10 on the phase-minimized network SNR for the semi-analytic injections in O1 and O2. The color of each circle corresponds to the $\langle VT \rangle$ value. The plotted points correspond to the central points of log-normal distributions with widths 0.1 in logarithmic mass.

3. SOURCE PROPERTIES

After identifying GW candidates, we coherently analyze the data from the network of GW detectors to infer the properties of the source of each signal (Abac et al. 2026b). These inferences are in turn used in companion papers to understand the population of compact objects (Abac et al. 2026d), measure cosmic expansion history (Abac et al. 2026e), and as a baseline for analyses that extend beyond our standard assumptions, such as for tests of general relativity carried out on new candidates from O4b (Abac et al. 2026f). These downstream analyses set stricter thresholds than used in Section 2 in order to mitigate the impact of differing methods of computing $p_{\rm astro}$ across search pipelines and attain a higher-purity subset of candidates. We restrict our estimation of the source properties to those that have both $p_{\rm astro} \geq 0.5$ and FAR $< 1\,{\rm yr}^{-1}$ at least one search pipeline. There is no GW candidate with a FAR $< 1\,{\rm yr}^{-1}$ and $p_{\rm astro} < 0.5$ in all pipelines.

We use Bayesian parameter estimation in order to infer the posterior probability distributions over the source parameters given a segment of data around each candidate. The posteriors are derived assuming models of GW emission and under the assumption of stationary, Gaussian noise which is uncorrelated across detectors (e.g., Veitch et al. 2015; Abbott et al. 2016b; Thrane & Talbot 2019; Abbott et al. 2020; Christensen & Meyer 2022; Abac et al. 2026b). When we identify the presence of transient, non-Gaussian noise around the time of a candidate, we exclude the affected frequency band or model and coherently remove the noise transient using the BayesWave algorithm (Cornish & Littenberg 2015; Littenberg & Cornish 2015; Cornish et al. 2021; Hourihane et al. 2022; Gupta & Cornish 2024; Chatziioannou et al. 2021). We discuss these cases further in Appendix C.

Our default priors are chosen to be agnostic and sufficiently wide to cover the region of the parameter space where the posteriors have support (Abac et al. 2026b). Specifically, they are uniform in (redshifted) component masses, uniform in spin magnitudes, isotropic in spin orientations, isotropic in binary orientation, uniform in merger time and coalescence phase, isotropic in sky location, and our distance prior corresponds to a uniform merger rate in comoving volume and time. Our inferences are given in terms of samples from the posteriors, from which we derive point estimates and uncertainties for the binary parameters (in the form of median values and 90% credible intervals) after marginalizing over the remaining parameters.

For all candidates, we assume quasi-circular orbits, and we carry out inference using multiple waveform models that all incorporate the effects of higher-order multipolar emission and spin precession. We also use two independent sampling codes, Bilby (Ashton et al. 2019; Romero-Shaw et al. 2020) and RIFT (Pankow et al. 2015; Lange et al. 2017; Wysocki et al. 2019). Details of the waveform models and sampling algorithms are given in Abac et al. (2026b). For each BBH candidate, we use the IMRPhenomXPHM_SpinTaylor (Pratten et al. 2021; Colleoni et al. 2025) and IMRPhenomXPNR (Hamilton et al. 2026) waveform models together with the Bilby sampler, and the SEOBNRv5PHM (Pompili et al. 2023; Ramos-Buades et al. 2023; Estellés et al. 2026) waveform model with either Bilby or RIFT sampler. In particular for SEOBNRv5PHM, we select results inferred with Bilby for candidates where further runs would be required to ensure the convergence of the RIFT results.

Many BBH candidates lie within the parameter-space coverage of the surrogate model NRSur7dq4 (Varma et al. 2019) which is built on numerical simulations of BBH coalescences, and in these cases we additionally use NRSur7dq4 for parameter estimation with Bilby. As an illustrative result, we report our posterior samples in tables or figures based on the IMRPhenomXPHM_SpinTaylor waveform model unless otherwise specified. More details are provided in Section 3.5 on where analyses with different models differ significantly.

Our key results for the O4b candidates passing our selection criteria with a FAR $< 1\,{\rm yr}^{-1}$ are summarized in Table 3 and shown in Figures 2, 3, and 4. As mentioned in Section 2, GW240406_062847 in Table 1, which was detected during the pre-O4b engineering run, lacks detailed information about the detector calibration, and hence, we do not report its source properties here. Our default agnostic priors (Abac et al. 2026b) do not make strong assumptions about the nature of the underlying astrophysical population. In addition to the default prior, we also reweight the inferred posterior distribution of our BBH candidates using a population-informed prior (default strongly-parameterised models, Table 1 of Abac et al. 2026d), and show these population-informed measurements in Figure 2.

Table 3. The properties of GW candidates from O4b with a FAR $< 1\,{\rm yr}^{-1}$ and $p_{\rm astro} \geq 0.5$, inferred with the default prior. For one-dimensional distributions, we provide the median and 90% symmetric credible intervals, while for the localization area $\Delta\Omega$ we provide the 90% credible area.

Candidate	M $[M_\odot]$	$\mathcal{M}$ $[M_\odot]$	m_1 $[M_\odot]$	m_2 $[M_\odot]$	$\chi_{\rm eff}$	$D_{\rm L}$ [Gpc]	z	$M_{\rm f}$ $[M_\odot]$	$\chi_{\rm f}$	$\Delta\Omega$ [deg^2]	SNR
GW240413_022019	$13.56^{+1.41}_{-0.52}$	$5.74^{+0.23}_{-0.11}$	$7.9^{+2.8}_{-1.2}$	$5.57^{+0.96}_{-1.35}$	$0.07^{+0.14}_{-0.04}$	$0.57^{+0.11}_{-0.22}$	$0.12^{+0.02}_{-0.04}$	$12.92^{+1.49}_{-0.52}$	$0.70^{+0.03}_{-0.04}$	37	$17.3^{+0.2}_{-0.2}$
GW240414_054515	$65.0^{+8.4}_{-6.3}$	$27.1^{+3.6}_{-2.8}$	$38.8^{+12.1}_{-7.2}$	$25.9^{+6.9}_{-8.1}$	$0.03^{+0.22}_{-0.21}$	$1.53^{+0.68}_{-0.58}$	$0.29^{+0.11}_{-0.10}$	$62.2^{+8.0}_{-6.0}$	$0.69^{+0.11}_{-0.12}$	270	$10.7^{+0.2}_{-0.4}$
GW240420_175625	$58.6^{+10.3}_{-8.7}$	$24.7^{+4.6}_{-3.8}$	$34.6^{+10.0}_{-7.2}$	$23.8^{+7.2}_{-7.1}$	$0.00^{+0.23}_{-0.25}$	$2.0^{+1.6}_{-1.1}$	$0.37^{+0.22}_{-0.18}$	$56.0^{+9.8}_{-8.3}$	$0.68^{+0.10}_{-0.11}$	28000	$9.5^{+0.2}_{-0.4}$

Table 3 *continued*

Table 3 *(continued)*

Candidate	M $[M_\odot]$	$\mathcal{M}$ $[M_\odot]$	m_1 $[M_\odot]$	m_2 $[M_\odot]$	$\chi_{\rm eff}$	$D_{\rm L}$ [Gpc]	z	$M_{\rm f}$ $[M_\odot]$	$\chi_{\rm f}$	$\Delta\Omega$ [deg^2]	SNR
GW240426_031451	88^{+18}_{-13}	$37.1^{+8.2}_{-6.3}$	52^{+14}_{-11}	36^{+11}_{-12}	$-0.05^{+0.24}_{-0.28}$	$4.0^{+2.6}_{-2.0}$	$0.65^{+0.33}_{-0.28}$	84^{+17}_{-13}	$0.67^{+0.11}_{-0.13}$	3200	$9.1^{+0.3}_{-0.5}$
GW240428_225440	$34.6^{+2.3}_{-1.5}$	$14.72^{+0.72}_{-0.48}$	$19.8^{+4.9}_{-2.6}$	$14.7^{+2.2}_{-2.9}$	$0.03^{+0.10}_{-0.08}$	$0.84^{+0.20}_{-0.28}$	$0.17^{+0.04}_{-0.05}$	$33.0^{+2.3}_{-1.4}$	$0.69^{+0.04}_{-0.04}$	200	$15.6^{+0.2}_{-0.3}$
GW240501_033534	66^{+14}_{-10}	$28.0^{+6.4}_{-4.4}$	$38.6^{+11.6}_{-8.0}$	$27.7^{+8.6}_{-8.2}$	$0.04^{+0.26}_{-0.28}$	$4.7^{+2.7}_{-2.2}$	$0.74^{+0.33}_{-0.30}$	$63.1^{+13.4}_{-9.5}$	$0.70^{+0.10}_{-0.12}$	1700	$9.7^{+0.4}_{-0.5}$
GW240505_133552	$54.0^{+11.9}_{-7.7}$	$23.0^{+5.3}_{-3.4}$	$31.0^{+9.2}_{-5.9}$	$23.1^{+6.8}_{-6.7}$	$-0.13^{+0.25}_{-0.30}$	$4.7^{+2.6}_{-2.1}$	$0.74^{+0.32}_{-0.29}$	$51.8^{+11.3}_{-7.3}$	$0.65^{+0.10}_{-0.13}$	2100	$8.2^{+0.3}_{-0.6}$
GW240507_041632	$39.9^{+7.8}_{-6.9}$	$13.8^{+1.9}_{-1.4}$	$31.3^{+9.2}_{-11.6}$	$8.5^{+6.3}_{-1.9}$	$0.01^{+0.20}_{-0.23}$	$1.45^{+0.90}_{-0.50}$	$0.28^{+0.14}_{-0.09}$	$38.9^{+8.0}_{-7.2}$	$0.55^{+0.19}_{-0.13}$	680	$9.7^{+0.5}_{-0.7}$
GW240511_031507	$72.6^{+7.4}_{-5.8}$	$31.1^{+3.3}_{-2.6}$	$40.5^{+7.4}_{-5.1}$	$32.2^{+5.5}_{-6.6}$	$0.05^{+0.17}_{-0.16}$	$1.99^{+0.75}_{-0.76}$	$0.36^{+0.11}_{-0.12}$	$69.1^{+6.8}_{-5.5}$	$0.71^{+0.07}_{-0.07}$	120	$15.6^{+0.2}_{-0.3}$
GW240512_024139	$20.7^{+2.8}_{-1.5}$	$8.62^{+0.65}_{-0.39}$	$12.6^{+4.8}_{-2.5}$	$8.0^{+1.8}_{-2.1}$	$0.14^{+0.13}_{-0.07}$	$1.17^{+0.34}_{-0.49}$	$0.23^{+0.06}_{-0.09}$	$19.7^{+3.0}_{-1.5}$	$0.72^{+0.06}_{-0.04}$	190	$10.8^{+0.3}_{-0.5}$
GW240513_183302	$41.4^{+4.3}_{-3.2}$	$17.4^{+1.8}_{-1.1}$	$24.4^{+6.0}_{-4.2}$	$16.9^{+3.6}_{-3.6}$	$0.14^{+0.13}_{-0.14}$	$2.25^{+0.69}_{-0.80}$	$0.40^{+0.10}_{-0.13}$	$39.4^{+4.2}_{-3.1}$	$0.74^{+0.06}_{-0.06}$	33	$13.6^{+0.2}_{-0.4}$
GW240514_121713	$82.7^{+11.2}_{-6.8}$	$35.4^{+5.2}_{-3.7}$	$46.8^{+9.3}_{-6.3}$	$36.7^{+7.5}_{-10.6}$	$0.01^{+0.17}_{-0.18}$	$2.59^{+0.82}_{-1.04}$	$0.45^{+0.12}_{-0.16}$	$78.9^{+10.4}_{-6.3}$	$0.69^{+0.08}_{-0.09}$	190	$16.2^{+0.2}_{-0.3}$
GW240515_005301	$56.3^{+10.9}_{-8.1}$	$22.4^{+4.8}_{-2.7}$	$37.1^{+11.4}_{-9.9}$	$18.5^{+8.9}_{-4.5}$	$0.47^{+0.17}_{-0.19}$	$3.8^{+1.8}_{-1.9}$	$0.63^{+0.24}_{-0.27}$	$53.2^{+10.3}_{-8.0}$	$0.84^{+0.06}_{-0.09}$	1700	$10.3^{+0.3}_{-0.4}$
GW240519_012815	104^{+18}_{-19}	$43.1^{+8.3}_{-9.3}$	65^{+19}_{-16}	39^{+13}_{-16}	$-0.04^{+0.26}_{-0.31}$	$1.74^{+1.83}_{-0.82}$	$0.32^{+0.27}_{-0.14}$	100^{+17}_{-18}	$0.65^{+0.11}_{-0.15}$	2300	$10.6^{+0.4}_{-0.6}$
GW240520_213616	$19.6^{+2.1}_{-1.4}$	$8.28^{+0.62}_{-0.52}$	$11.4^{+3.6}_{-1.9}$	$8.0^{+1.5}_{-1.8}$	$-0.00^{+0.12}_{-0.08}$	$1.40^{+0.53}_{-0.50}$	$0.27^{+0.08}_{-0.09}$	$18.7^{+2.1}_{-1.4}$	$0.67^{+0.04}_{-0.04}$	350	$10.5^{+0.3}_{-0.5}$
GW240525_031210	$52.8^{+12.4}_{-9.2}$	$22.1^{+5.2}_{-3.8}$	$31.1^{+12.1}_{-7.2}$	$21.4^{+7.1}_{-6.8}$	$0.17^{+0.25}_{-0.26}$	$4.5^{+3.0}_{-2.2}$	$0.72^{+0.37}_{-0.30}$	$50.2^{+11.7}_{-8.8}$	$0.75^{+0.10}_{-0.13}$	2000	$8.0^{+0.5}_{-0.7}$
GW240526_093944	$23.2^{+4.3}_{-3.2}$	$9.5^{+1.3}_{-1.0}$	$14.5^{+6.1}_{-3.6}$	$8.4^{+2.5}_{-2.3}$	$0.22^{+0.14}_{-0.12}$	$1.94^{+1.10}_{-0.94}$	$0.35^{+0.16}_{-0.16}$	$22.1^{+4.4}_{-3.1}$	$0.76^{+0.08}_{-0.06}$	900	$8.4^{+0.5}_{-0.7}$
GW240527_183429	84^{+22}_{-13}	$34.5^{+10.8}_{-6.7}$	52^{+17}_{-12}	33^{+15}_{-15}	$0.31^{+0.27}_{-0.33}$	$6.4^{+3.5}_{-3.1}$	$0.96^{+0.40}_{-0.40}$	80^{+20}_{-12}	$0.79^{+0.09}_{-0.16}$	1100	$9.4^{+0.3}_{-0.5}$
GW240527_230910	$37.5^{+7.0}_{-5.1}$	$14.07^{+0.76}_{-0.63}$	$27.6^{+8.9}_{-9.6}$	$10.0^{+4.9}_{-2.1}$	$-0.03^{+0.20}_{-0.24}$	$1.19^{+0.32}_{-0.32}$	$0.23^{+0.05}_{-0.06}$	$36.4^{+7.1}_{-5.3}$	$0.58^{+0.10}_{-0.08}$	28	$10.7^{+0.3}_{-0.4}$
GW240530_012417	$22.6^{+5.4}_{-2.4}$	$9.26^{+0.78}_{-0.75}$	$14.1^{+8.4}_{-3.3}$	$8.3^{+2.1}_{-3.0}$	$0.04^{+0.25}_{-0.11}$	$1.01^{+0.63}_{-0.50}$	$0.20^{+0.11}_{-0.09}$	$21.6^{+5.6}_{-2.3}$	$0.68^{+0.07}_{-0.05}$	640	$10.6^{+0.5}_{-0.6}$
GW240531_040326	$34.0^{+6.4}_{-4.3}$	$14.4^{+2.6}_{-1.8}$	$19.5^{+7.4}_{-3.7}$	$14.3^{+3.5}_{-4.3}$	$0.14^{+0.22}_{-0.21}$	$3.0^{+1.6}_{-1.5}$	$0.52^{+0.22}_{-0.23}$	$32.3^{+6.1}_{-4.1}$	$0.74^{+0.09}_{-0.09}$	930	$8.5^{+0.4}_{-0.6}$
GW240531_075248	$55.6^{+13.0}_{-9.1}$	$23.4^{+5.6}_{-3.8}$	$33.0^{+10.4}_{-7.6}$	$22.6^{+7.6}_{-6.4}$	$0.04^{+0.26}_{-0.27}$	$4.1^{+2.8}_{-2.2}$	$0.67^{+0.35}_{-0.32}$	$53.1^{+12.2}_{-8.7}$	$0.70^{+0.11}_{-0.13}$	1700	$8.6^{+0.4}_{-0.5}$
GW240601_061200	85^{+23}_{-20}	$35.3^{+9.7}_{-7.9}$	52^{+20}_{-16}	32^{+12}_{-11}	$-0.08^{+0.27}_{-0.31}$	$5.1^{+4.4}_{-2.6}$	$0.79^{+0.52}_{-0.35}$	82^{+22}_{-19}	$0.65^{+0.12}_{-0.17}$	2600	$8.3^{+0.5}_{-0.7}$
GW240601_231004	$18.6^{+2.4}_{-1.5}$	$7.80^{+0.65}_{-0.51}$	$10.6^{+4.8}_{-1.7}$	$7.7^{+1.5}_{-2.4}$	$0.09^{+0.16}_{-0.07}$	$1.27^{+0.53}_{-0.54}$	$0.25^{+0.09}_{-0.10}$	$17.7^{+2.6}_{-1.4}$	$0.72^{+0.06}_{-0.05}$	810	$9.8^{+0.3}_{-0.5}$
GW240612_081540	92^{+27}_{-18}	$38.5^{+12.2}_{-8.5}$	55^{+21}_{-13}	38^{+16}_{-16}	$0.07^{+0.34}_{-0.34}$	$6.2^{+4.1}_{-3.1}$	$0.93^{+0.47}_{-0.40}$	88^{+25}_{-17}	$0.71^{+0.13}_{-0.15}$	2800	$7.4^{+0.3}_{-0.6}$
GW240615_113620	$60.4^{+3.5}_{-2.5}$	$25.9^{+1.7}_{-1.2}$	$34.0^{+5.4}_{-3.7}$	$26.4^{+4.0}_{-4.8}$	$-0.07^{+0.11}_{-0.13}$	$1.56^{+0.29}_{-0.45}$	$0.29^{+0.05}_{-0.08}$	$57.8^{+3.3}_{-2.4}$	$0.66^{+0.05}_{-0.06}$	6	$23.8^{+0.1}_{-0.2}$
GW240615_160735	$48.5^{+8.5}_{-5.9}$	$20.4^{+4.0}_{-2.4}$	$28.5^{+7.9}_{-5.6}$	$20.0^{+5.7}_{-5.6}$	$0.28^{+0.20}_{-0.24}$	$4.0^{+1.9}_{-1.9}$	$0.65^{+0.24}_{-0.27}$	$45.9^{+8.0}_{-5.6}$	$0.78^{+0.08}_{-0.11}$	1100	$9.9^{+0.3}_{-0.5}$
GW240618_071627	105^{+30}_{-24}	43^{+13}_{-10}	65^{+24}_{-19}	40^{+17}_{-15}	$0.00^{+0.30}_{-0.32}$	$5.5^{+5.1}_{-2.9}$	$0.84^{+0.59}_{-0.39}$	101^{+28}_{-23}	$0.68^{+0.13}_{-0.17}$	5400	$8.1^{+0.4}_{-0.6}$
GW240621_195059	$66.0^{+4.6}_{-2.8}$	$28.4^{+2.2}_{-1.4}$	$36.8^{+4.4}_{-3.7}$	$29.7^{+4.1}_{-5.2}$	$-0.00^{+0.10}_{-0.10}$	$1.21^{+0.26}_{-0.43}$	$0.23^{+0.04}_{-0.08}$	$62.9^{+4.2}_{-2.6}$	$0.68^{+0.04}_{-0.04}$	32	$27.6^{+0.1}_{-0.2}$
GW240621_200935	73^{+17}_{-12}	$31.1^{+7.6}_{-5.3}$	$41.6^{+11.6}_{-8.3}$	$31.6^{+9.8}_{-9.5}$	$-0.09^{+0.23}_{-0.28}$	$4.8^{+3.0}_{-2.4}$	$0.75^{+0.36}_{-0.32}$	70^{+16}_{-11}	$0.67^{+0.10}_{-0.12}$	1600	$8.9^{+0.3}_{-0.5}$
GW240621_214041	76^{+24}_{-16}	$32.1^{+10.3}_{-6.7}$	45^{+17}_{-11}	32^{+13}_{-11}	$0.00^{+0.26}_{-0.28}$	$6.8^{+4.8}_{-3.4}$	$1.00^{+0.54}_{-0.44}$	73^{+22}_{-15}	$0.69^{+0.11}_{-0.13}$	3200	$7.5^{+0.4}_{-0.6}$
GW240622_004008	$30.2^{+4.5}_{-2.9}$	$12.50^{+0.98}_{-0.91}$	$18.6^{+7.6}_{-4.0}$	$11.3^{+2.9}_{-3.2}$	$0.25^{+0.13}_{-0.10}$	$1.47^{+0.60}_{-0.53}$	$0.28^{+0.10}_{-0.09}$	$28.7^{+4.8}_{-2.8}$	$0.77^{+0.07}_{-0.05}$	280	$12.3^{+0.3}_{-0.4}$
GW240627_131622	$20.1^{+3.8}_{-2.2}$	$8.08^{+0.72}_{-0.57}$	$13.2^{+5.7}_{-3.5}$	$6.7^{+2.4}_{-1.8}$	$0.00^{+0.19}_{-0.16}$	$1.35^{+0.62}_{-0.57}$	$0.26^{+0.10}_{-0.10}$	$19.3^{+4.0}_{-2.2}$	$0.65^{+0.08}_{-0.08}$	890	$9.2^{+0.5}_{-0.6}$
GW240629_145256	$18.9^{+1.8}_{-1.1}$	$8.01^{+0.61}_{-0.35}$	$11.1^{+3.0}_{-1.7}$	$7.8^{+1.4}_{-1.6}$	$0.04^{+0.11}_{-0.06}$	$1.28^{+0.34}_{-0.50}$	$0.25^{+0.06}_{-0.09}$	$18.1^{+1.8}_{-1.1}$	$0.69^{+0.03}_{-0.04}$	260	$12.3^{+0.3}_{-0.4}$
GW240630_101703	$50.2^{+8.0}_{-5.8}$	$21.4^{+3.5}_{-2.5}$	$28.6^{+7.6}_{-4.8}$	$21.6^{+5.0}_{-5.3}$	$-0.04^{+0.23}_{-0.27}$	$3.2^{+1.5}_{-1.4}$	$0.54^{+0.21}_{-0.20}$	$48.0^{+7.5}_{-5.5}$	$0.69^{+0.10}_{-0.11}$	700	$10.1^{+0.3}_{-0.5}$
GW240703_191355	$61.2^{+8.6}_{-9.3}$	$26.2^{+3.8}_{-4.0}$	$34.4^{+8.5}_{-6.2}$	$26.4^{+5.9}_{-6.7}$	$0.05^{+0.21}_{-0.20}$	$1.88^{+1.54}_{-0.86}$	$0.34^{+0.23}_{-0.14}$	$58.3^{+8.0}_{-8.8}$	$0.71^{+0.09}_{-0.08}$	5500	$10.1^{+0.3}_{-0.6}$
GW240705_053215	$81.9^{+12.8}_{-8.1}$	$34.9^{+5.7}_{-3.6}$	$47.1^{+9.7}_{-7.7}$	$35.3^{+8.0}_{-8.2}$	$-0.03^{+0.20}_{-0.21}$	$3.7^{+1.4}_{-1.6}$	$0.61^{+0.18}_{-0.23}$	$78.2^{+12.1}_{-7.7}$	$0.69^{+0.10}_{-0.09}$	270	$14.3^{+0.2}_{-0.3}$
GW240716_034900	$66.8^{+8.8}_{-7.8}$	$28.1^{+3.9}_{-3.3}$	$40.3^{+8.8}_{-8.0}$	$26.5^{+6.7}_{-6.4}$	$-0.02^{+0.22}_{-0.25}$	$1.86^{+1.39}_{-0.93}$	$0.34^{+0.21}_{-0.16}$	$63.9^{+8.4}_{-7.5}$	$0.67^{+0.10}_{-0.13}$	10000	$13.0^{+0.3}_{-0.4}$
GW240824_205609	107^{+37}_{-27}	43^{+17}_{-12}	70^{+32}_{-24}	37^{+20}_{-17}	$0.08^{+0.35}_{-0.35}$	$5.3^{+5.4}_{-3.0}$	$0.81^{+0.62}_{-0.41}$	103^{+36}_{-26}	$0.69^{+0.15}_{-0.20}$	3000	$7.8^{+0.5}_{-0.7}$
GW240825_055146	$21.3^{+3.8}_{-2.1}$	$8.77^{+0.77}_{-0.61}$	$13.2^{+5.8}_{-3.0}$	$7.9^{+2.0}_{-2.2}$	$0.07^{+0.19}_{-0.13}$	$1.25^{+0.53}_{-0.55}$	$0.24^{+0.09}_{-0.10}$	$20.3^{+3.9}_{-2.0}$	$0.69^{+0.07}_{-0.06}$	510	$9.7^{+0.4}_{-0.6}$
GW240830_211120	$19.8^{+2.3}_{-1.6}$	$8.33^{+0.66}_{-0.54}$	$11.9^{+3.6}_{-2.3}$	$7.8^{+1.6}_{-1.7}$	$0.07^{+0.13}_{-0.07}$	$1.14^{+0.50}_{-0.49}$	$0.22^{+0.08}_{-0.09}$	$18.9^{+2.3}_{-1.6}$	$0.69^{+0.04}_{-0.04}$	460	$10.7^{+0.4}_{-0.5}$
GW240902_143306	$42.7^{+8.2}_{-5.8}$	$18.2^{+3.6}_{-2.6}$	$24.4^{+6.8}_{-4.4}$	$18.3^{+4.9}_{-5.2}$	$-0.03^{+0.28}_{-0.30}$	$2.9^{+1.7}_{-1.3}$	$0.49^{+0.24}_{-0.20}$	$40.8^{+7.5}_{-5.5}$	$0.69^{+0.11}_{-0.12}$	910	$9.6^{+0.4}_{-0.5}$
GW240907_153833	67^{+14}_{-12}	$28.3^{+6.5}_{-5.0}$	$38.0^{+11.3}_{-8.0}$	$28.3^{+8.7}_{-8.5}$	$0.04^{+0.26}_{-0.26}$	$4.5^{+3.1}_{-2.1}$	$0.71^{+0.38}_{-0.29}$	63^{+14}_{-11}	$0.71^{+0.10}_{-0.10}$	1600	$9.1^{+0.3}_{-0.5}$
GW240908_082628	68^{+12}_{-14}	$28.6^{+5.6}_{-5.8}$	$39.8^{+11.8}_{-9.4}$	$27.7^{+8.4}_{-9.2}$	$0.14^{+0.24}_{-0.25}$	$3.1^{+2.6}_{-1.3}$	$0.53^{+0.34}_{-0.20}$	65^{+11}_{-13}	$0.73^{+0.10}_{-0.13}$	160	$10.0^{+0.3}_{-0.6}$
GW240908_125134	77^{+19}_{-15}	$32.5^{+8.6}_{-6.6}$	45^{+15}_{-11}	32^{+11}_{-11}	$-0.09^{+0.24}_{-0.30}$	$4.7^{+3.5}_{-2.3}$	$0.74^{+0.42}_{-0.31}$	74^{+18}_{-14}	$0.66^{+0.10}_{-0.14}$	1100	$8.3^{+0.3}_{-0.6}$
GW240910_103535	$17.3^{+1.8}_{-1.1}$	$7.16^{+0.39}_{-0.19}$	$10.9^{+3.1}_{-2.4}$	$6.3^{+1.7}_{-1.3}$	$0.12^{+0.12}_{-0.07}$	$0.74^{+0.17}_{-0.31}$	$0.15^{+0.03}_{-0.06}$	$16.6^{+1.9}_{-1.1}$	$0.70^{+0.04}_{-0.04}$	440	$17.4^{+0.2}_{-0.2}$
GW240915_001357	$18.80^{+3.10}_{-0.87}$	$7.95^{+0.37}_{-0.21}$	$10.9^{+5.5}_{-1.7}$	$7.7^{+1.3}_{-2.3}$	$0.13^{+0.16}_{-0.05}$	$0.92^{+0.19}_{-0.29}$	$0.18^{+0.03}_{-0.05}$	$17.88^{+3.22}_{-0.86}$	$0.72^{+0.04}_{-0.03}$	16	$16.2^{+0.2}_{-0.3}$
GW240915_105151	$19.4^{+4.4}_{-1.3}$	$8.07^{+0.40}_{-0.32}$	$11.6^{+7.3}_{-2.2}$	$7.5^{+1.7}_{-2.6}$	$0.07^{+0.22}_{-0.09}$	$0.63^{+0.26}_{-0.28}$	$0.13^{+0.05}_{-0.05}$	$18.5^{+4.6}_{-1.2}$	$0.70^{+0.06}_{-0.04}$	4400	$13.7^{+0.3}_{-0.4}$
GW240916_184352	$18.7^{+2.4}_{-1.7}$	$7.89^{+0.80}_{-0.62}$	$10.7^{+4.2}_{-1.7}$	$7.8^{+1.5}_{-2.2}$	$0.05^{+0.14}_{-0.09}$	$1.28^{+0.63}_{-0.64}$	$0.25^{+0.10}_{-0.11}$	$17.8^{+2.5}_{-1.6}$	$0.70^{+0.05}_{-0.05}$	1500	$9.1^{+0.3}_{-0.5}$
GW240919_061559	$67.8^{+7.0}_{-5.9}$	$29.0^{+3.2}_{-2.6}$	$38.3^{+6.6}_{-5.5}$	$29.6^{+5.4}_{-5.9}$	$-0.02^{+0.16}_{-0.17}$	$1.87^{+0.82}_{-0.74}$	$0.34^{+0.12}_{-0.12}$	$64.7^{+6.5}_{-5.6}$	$0.68^{+0.07}_{-0.06}$	21	$16.2^{+0.2}_{-0.3}$
GW240920_073424	$38.2^{+5.6}_{-3.9}$	$15.6^{+1.5}_{-1.3}$	$24.7^{+7.6}_{-5.6}$	$13.4^{+3.3}_{-3.2}$	$-0.09^{+0.19}_{-0.16}$	$1.44^{+0.62}_{-0.55}$	$0.27^{+0.10}_{-0.09}$	$36.7^{+5.6}_{-3.8}$	$0.64^{+0.11}_{-0.09}$	420	$13.3^{+0.3}_{-0.4}$
GW240920_124024	$68.8^{+3.7}_{-2.6}$	$29.8^{+1.7}_{-1.2}$	$37.1^{+4.0}_{-2.8}$	$31.9^{+3.0}_{-3.9}$	$-0.04^{+0.08}_{-0.09}$	$1.09^{+0.22}_{-0.32}$	$0.21^{+0.04}_{-0.06}$	$65.6^{+3.5}_{-2.4}$	$0.68^{+0.04}_{-0.03}$	160	$37.0^{+0.1}_{-0.1}$
GW240921_201835	$44.8^{+7.5}_{-7.0}$	$15.62^{+0.76}_{-1.52}$	$34.9^{+8.9}_{-9.4}$	$9.8^{+3.0}_{-1.7}$	$0.00^{+0.17}_{-0.22}$	$0.92^{+0.76}_{-0.30}$	$0.18^{+0.13}_{-0.06}$	$43.7^{+7.6}_{-7.2}$	$0.52^{+0.08}_{-0.06}$	1800	$11.1^{+0.4}_{-0.7}$
GW240922_142106	$19.3^{+2.2}_{-1.2}$	$8.12^{+0.63}_{-0.37}$	$11.5^{+3.9}_{-2.0}$	$7.8^{+1.5}_{-1.8}$	$0.07^{+0.12}_{-0.06}$	$1.23^{+0.34}_{-0.50}$	$0.24^{+0.06}_{-0.09}$	$18.4^{+2.3}_{-1.2}$	$0.70^{+0.04}_{-0.03}$	200	$12.4^{+0.3}_{-0.4}$
GW240923_204006	$79.9^{+16.2}_{-9.6}$	$34.1^{+7.3}_{-4.8}$	$46.1^{+10.3}_{-7.9}$	$34.9^{+9.9}_{-10.6}$	$0.01^{+0.20}_{-0.21}$	$4.0^{+1.8}_{-1.9}$	$0.65^{+0.24}_{-0.27}$	$76.3^{+15.1}_{-9.1}$	$0.70^{+0.08}_{-0.10}$	440	$11.7^{+0.2}_{-0.4}$

Table 3 *continued*

Table 3 *(continued)*

Candidate	M $[M_\odot]$	$\mathcal{M}$ $[M_\odot]$	m_1 $[M_\odot]$	m_2 $[M_\odot]$	$\chi_{\rm eff}$	$D_{\rm L}$ [Gpc]	z	$M_{\rm f}$ $[M_\odot]$	$\chi_{\rm f}$	$\Delta\Omega$ [deg^2]	SNR
GW240924_000316	80^{+19}_{-14}	$34.2^{+8.4}_{-6.3}$	$46.0^{+14.3}_{-9.9}$	34^{+11}_{-10}	$0.10^{+0.23}_{-0.24}$	$3.7^{+2.6}_{-1.7}$	$0.61^{+0.34}_{-0.25}$	76^{+18}_{-14}	$0.73^{+0.10}_{-0.11}$	800	$9.9^{+0.4}_{-0.5}$
GW240925_005809	$16.01^{+0.62}_{-0.40}$	$6.85^{+0.23}_{-0.07}$	$8.87^{+1.83}_{-0.88}$	$7.09^{+0.78}_{-1.24}$	$0.02^{+0.07}_{-0.02}$	$0.36^{+0.06}_{-0.17}$	$0.08^{+0.01}_{-0.03}$	$15.26^{+0.65}_{-0.40}$	$0.69^{+0.02}_{-0.02}$	26	$31.9^{+0.1}_{-0.1}$
GW240930_035959	$36.8^{+3.8}_{-3.4}$	$14.50^{+0.77}_{-0.98}$	$25.5^{+5.0}_{-4.8}$	$11.2^{+2.1}_{-1.8}$	$-0.05^{+0.14}_{-0.13}$	$0.95^{+0.49}_{-0.29}$	$0.19^{+0.08}_{-0.05}$	$35.5^{+3.8}_{-3.4}$	$0.58^{+0.05}_{-0.04}$	370	$15.2^{+0.2}_{-0.3}$
GW240930_234614	$58.0^{+12.3}_{-9.2}$	$23.9^{+4.9}_{-3.7}$	$35.8^{+14.0}_{-8.9}$	$21.9^{+7.2}_{-7.2}$	$0.04^{+0.27}_{-0.30}$	$3.6^{+2.6}_{-2.0}$	$0.60^{+0.33}_{-0.30}$	$55.5^{+12.0}_{-8.9}$	$0.71^{+0.11}_{-0.15}$	1000	$9.0^{+0.7}_{-0.6}$
GW241002_030559	$67.2^{+8.8}_{-7.7}$	$28.8^{+3.9}_{-3.4}$	$37.3^{+8.4}_{-5.5}$	$29.9^{+5.6}_{-7.1}$	$-0.10^{+0.20}_{-0.23}$	$1.46^{+0.95}_{-0.68}$	$0.28^{+0.15}_{-0.12}$	$64.2^{+8.2}_{-7.2}$	$0.66^{+0.08}_{-0.09}$	720	$11.4^{+0.3}_{-0.4}$
GW241006_015333	$44.9^{+4.2}_{-3.0}$	$19.4^{+1.8}_{-1.3}$	$24.6^{+4.2}_{-2.8}$	$20.3^{+2.8}_{-3.1}$	$0.07^{+0.13}_{-0.13}$	$1.85^{+0.65}_{-0.71}$	$0.34^{+0.10}_{-0.12}$	$42.7^{+4.0}_{-2.9}$	$0.71^{+0.05}_{-0.04}$	240	$16.4^{+0.2}_{-0.3}$
GW241007_082943	$63.2^{+15.7}_{-9.8}$	$26.7^{+6.8}_{-4.3}$	$36.6^{+13.5}_{-7.7}$	$26.6^{+8.4}_{-7.9}$	$0.11^{+0.26}_{-0.26}$	$4.0^{+2.3}_{-2.0}$	$0.65^{+0.29}_{-0.29}$	$60.1^{+14.9}_{-9.3}$	$0.74^{+0.10}_{-0.12}$	980	$9.3^{+0.3}_{-0.5}$
GW241009_022835	64^{+19}_{-13}	$27.1^{+8.2}_{-5.6}$	$37.1^{+14.1}_{-8.9}$	$26.8^{+10.2}_{-9.5}$	$0.09^{+0.26}_{-0.25}$	$5.6^{+3.8}_{-2.8}$	$0.85^{+0.45}_{-0.37}$	61^{+18}_{-12}	$0.73^{+0.10}_{-0.12}$	2400	$7.8^{+0.4}_{-0.6}$
GW241009_084816	$21.0^{+2.3}_{-1.9}$	$8.78^{+0.67}_{-0.65}$	$12.7^{+4.0}_{-2.5}$	$8.1^{+1.9}_{-1.9}$	$-0.05^{+0.14}_{-0.08}$	$1.13^{+0.58}_{-0.48}$	$0.22^{+0.10}_{-0.09}$	$20.1^{+2.4}_{-1.9}$	$0.67^{+0.06}_{-0.04}$	430	$11.8^{+0.3}_{-0.4}$
GW241009_220455	$58.9^{+9.3}_{-10.9}$	$25.2^{+4.0}_{-5.1}$	$33.2^{+8.1}_{-6.6}$	$25.5^{+5.9}_{-8.1}$	$0.11^{+0.23}_{-0.25}$	$2.9^{+2.2}_{-1.3}$	$0.50^{+0.30}_{-0.20}$	$56.0^{+8.7}_{-10.2}$	$0.73^{+0.09}_{-0.11}$	90	$9.2^{+0.3}_{-0.8}$
GW241011_233834	$25.5^{+2.0}_{-1.5}$	$9.09^{+0.08}_{-0.08}$	$19.5^{+2.6}_{-2.0}$	$5.96^{+0.58}_{-0.58}$	$0.50^{+0.06}_{-0.04}$	$0.21^{+0.04}_{-0.04}$	$0.05^{+0.01}_{-0.01}$	$24.4^{+2.1}_{-1.5}$	$0.84^{+0.02}_{-0.02}$	49	$35.8^{+0.1}_{-0.1}$
GW241101_220523	$60.2^{+12.7}_{-9.2}$	$23.6^{+5.8}_{-3.1}$	41^{+13}_{-12}	$19.3^{+9.8}_{-5.7}$	$0.15^{+0.33}_{-0.29}$	$2.2^{+1.4}_{-1.0}$	$0.39^{+0.21}_{-0.17}$	$57.7^{+11.9}_{-9.0}$	$0.70^{+0.16}_{-0.17}$	8700	$10.6^{+0.3}_{-0.5}$
GW241102_124058	$19.01^{+1.45}_{-0.47}$	$8.12^{+0.17}_{-0.09}$	$10.9^{+3.2}_{-1.4}$	$8.0^{+1.2}_{-1.7}$	$0.06^{+0.11}_{-0.04}$	$0.39^{+0.06}_{-0.11}$	$0.08^{+0.01}_{-0.02}$	$18.10^{+1.54}_{-0.46}$	$0.70^{+0.03}_{-0.04}$	23	$21.6^{+0.1}_{-0.2}$
GW241102_144729	$75.1^{+13.6}_{-9.8}$	$31.5^{+6.5}_{-4.8}$	$44.4^{+12.3}_{-8.6}$	$31.0^{+9.9}_{-11.1}$	$-0.09^{+0.21}_{-0.27}$	$3.4^{+2.0}_{-1.6}$	$0.57^{+0.26}_{-0.23}$	$72.0^{+12.7}_{-9.4}$	$0.65^{+0.09}_{-0.15}$	880	$11.3^{+0.3}_{-0.5}$
GW241109_033317	74^{+16}_{-11}	$31.4^{+7.0}_{-5.2}$	$42.4^{+11.3}_{-8.5}$	$31.7^{+9.3}_{-9.4}$	$0.01^{+0.22}_{-0.24}$	$2.7^{+2.0}_{-1.5}$	$0.46^{+0.28}_{-0.24}$	70^{+15}_{-11}	$0.70^{+0.10}_{-0.10}$	7200	$10.4^{+0.3}_{-0.5}$
GW241109_115924	$12.51^{+1.51}_{-0.68}$	$5.29^{+0.28}_{-0.20}$	$7.3^{+2.8}_{-1.1}$	$5.14^{+0.90}_{-1.26}$	$0.01^{+0.16}_{-0.05}$	$0.60^{+0.23}_{-0.29}$	$0.12^{+0.04}_{-0.06}$	$11.94^{+1.58}_{-0.66}$	$0.68^{+0.04}_{-0.04}$	12000	$11.6^{+0.2}_{-0.4}$
GW241110_124123	$24.5^{+3.5}_{-2.2}$	$9.84^{+0.50}_{-0.42}$	$16.4^{+5.1}_{-4.1}$	$8.0^{+2.2}_{-1.6}$	$-0.31^{+0.23}_{-0.18}$	$0.74^{+0.26}_{-0.26}$	$0.15^{+0.05}_{-0.05}$	$23.7^{+3.6}_{-2.2}$	$0.52^{+0.07}_{-0.06}$	100	$9.9^{+0.3}_{-0.5}$
GW241111_111552	$45.4^{+5.9}_{-3.7}$	$19.5^{+2.7}_{-1.6}$	$25.3^{+4.4}_{-3.3}$	$20.5^{+3.9}_{-4.2}$	$0.10^{+0.15}_{-0.14}$	$1.55^{+0.58}_{-0.74}$	$0.29^{+0.09}_{-0.13}$	$43.2^{+5.4}_{-3.4}$	$0.72^{+0.06}_{-0.06}$	490	$15.1^{+0.2}_{-0.3}$
GW241113_163507	$33.9^{+3.9}_{-3.0}$	$14.4^{+1.5}_{-1.1}$	$19.3^{+5.4}_{-3.0}$	$14.4^{+2.7}_{-3.3}$	$0.50^{+0.11}_{-0.11}$	$1.36^{+0.67}_{-0.63}$	$0.26^{+0.11}_{-0.11}$	$31.7^{+3.7}_{-2.8}$	$0.85^{+0.04}_{-0.04}$	14000	$12.0^{+0.2}_{-0.3}$
GW241114_024711	$71.9^{+9.9}_{-9.5}$	$29.2^{+4.7}_{-4.3}$	$47.0^{+9.7}_{-11.0}$	$25.0^{+8.2}_{-7.3}$	$0.12^{+0.21}_{-0.24}$	$2.6^{+1.6}_{-1.0}$	$0.45^{+0.22}_{-0.16}$	$68.9^{+9.4}_{-9.3}$	$0.74^{+0.09}_{-0.14}$	200	$11.1^{+0.4}_{-0.5}$
GW241114_235258	$19.1^{+2.9}_{-1.3}$	$8.04^{+0.50}_{-0.37}$	$11.3^{+5.2}_{-1.9}$	$7.7^{+1.5}_{-2.2}$	$0.06^{+0.18}_{-0.08}$	$0.79^{+0.30}_{-0.35}$	$0.16^{+0.05}_{-0.07}$	$18.2^{+3.0}_{-1.2}$	$0.69^{+0.05}_{-0.04}$	11000	$12.2^{+0.2}_{-0.4}$
GW241116_151753	99^{+48}_{-30}	$34.0^{+18.8}_{-9.6}$	70^{+57}_{-28}	24^{+26}_{-13}	$0.28^{+0.34}_{-0.48}$	$5.7^{+5.6}_{-2.9}$	$0.87^{+0.64}_{-0.39}$	95^{+48}_{-29}	$0.78^{+0.14}_{-0.27}$	3300	$8.4^{+0.6}_{-0.6}$
GW241124_024914	70^{+26}_{-15}	$28.4^{+8.6}_{-6.1}$	42^{+32}_{-12}	26^{+11}_{-11}	$0.04^{+0.33}_{-0.29}$	$4.5^{+4.0}_{-2.3}$	$0.72^{+0.48}_{-0.31}$	67^{+26}_{-15}	$0.68^{+0.14}_{-0.19}$	3900	$7.9^{+0.5}_{-0.6}$
GW241125_010116	106^{+23}_{-22}	45^{+10}_{-10}	60^{+14}_{-13}	47^{+14}_{-17}	$0.09^{+0.27}_{-0.27}$	$4.7^{+3.9}_{-2.2}$	$0.74^{+0.47}_{-0.30}$	101^{+22}_{-20}	$0.73^{+0.10}_{-0.11}$	2400	$9.8^{+0.4}_{-0.5}$
GW241127_061008	$85.3^{+6.0}_{-5.6}$	$30.8^{+3.6}_{-2.0}$	$63.8^{+8.7}_{-7.7}$	$20.8^{+6.5}_{-3.4}$	$-0.16^{+0.13}_{-0.14}$	$1.08^{+0.22}_{-0.18}$	$0.21^{+0.04}_{-0.03}$	$83.0^{+6.2}_{-5.4}$	$0.56^{+0.09}_{-0.10}$	83	$31.2^{+0.1}_{-0.2}$
GW241129_021832	$53.3^{+6.1}_{-4.2}$	$22.7^{+2.8}_{-1.7}$	$30.4^{+6.8}_{-4.5}$	$23.0^{+4.5}_{-4.8}$	$0.17^{+0.16}_{-0.16}$	$2.55^{+0.74}_{-0.91}$	$0.45^{+0.11}_{-0.14}$	$50.6^{+5.7}_{-3.9}$	$0.75^{+0.08}_{-0.08}$	350	$14.9^{+0.2}_{-0.3}$
GW241130_034908	$54.2^{+6.7}_{-5.1}$	$23.3^{+2.9}_{-2.2}$	$29.9^{+5.8}_{-4.1}$	$24.3^{+4.1}_{-4.1}$	$0.05^{+0.15}_{-0.15}$	$1.99^{+0.99}_{-0.93}$	$0.36^{+0.15}_{-0.15}$	$51.6^{+6.3}_{-4.9}$	$0.71^{+0.06}_{-0.05}$	450	$13.3^{+0.3}_{-0.4}$
GW241130_110422	$17.8^{+3.4}_{-1.7}$	$7.31^{+0.64}_{-0.48}$	$11.1^{+5.2}_{-2.5}$	$6.5^{+1.8}_{-1.9}$	$0.04^{+0.20}_{-0.10}$	$1.32^{+0.53}_{-0.57}$	$0.25^{+0.09}_{-0.10}$	$17.0^{+3.5}_{-1.7}$	$0.67^{+0.05}_{-0.05}$	1300	$9.2^{+0.3}_{-0.5}$
GW241201_055758	80^{+24}_{-16}	$33.5^{+10.7}_{-7.5}$	47^{+19}_{-12}	33^{+13}_{-13}	$0.13^{+0.36}_{-0.36}$	$7.1^{+4.7}_{-3.8}$	$1.03^{+0.53}_{-0.48}$	76^{+23}_{-15}	$0.74^{+0.13}_{-0.15}$	4100	$7.6^{+0.4}_{-0.6}$
GW241210_060606	$50.2^{+9.4}_{-5.7}$	$21.3^{+4.1}_{-2.4}$	$29.0^{+8.2}_{-5.2}$	$21.4^{+5.5}_{-5.5}$	$0.04^{+0.22}_{-0.19}$	$2.6^{+1.2}_{-1.2}$	$0.45^{+0.17}_{-0.19}$	$47.9^{+8.8}_{-5.5}$	$0.70^{+0.10}_{-0.09}$	900	$11.7^{+0.3}_{-0.4}$
GW241210_120900	64^{+15}_{-12}	$26.3^{+6.4}_{-4.9}$	40^{+15}_{-11}	$23.6^{+9.2}_{-8.0}$	$-0.07^{+0.24}_{-0.30}$	$3.6^{+3.0}_{-1.8}$	$0.59^{+0.38}_{-0.26}$	62^{+14}_{-12}	$0.64^{+0.11}_{-0.17}$	3500	$8.3^{+0.3}_{-0.6}$
GW241225_042553	$20.6^{+1.7}_{-1.1}$	$8.65^{+0.42}_{-0.26}$	$12.4^{+3.0}_{-2.3}$	$8.1^{+1.5}_{-1.5}$	$0.12^{+0.09}_{-0.05}$	$0.66^{+0.19}_{-0.27}$	$0.14^{+0.04}_{-0.05}$	$19.6^{+1.8}_{-1.1}$	$0.72^{+0.06}_{-0.04}$	3800	$17.0^{+0.2}_{-0.3}$
GW241225_082815	98^{+14}_{-11}	$41.8^{+6.1}_{-5.2}$	$55.7^{+11.0}_{-8.5}$	$42.2^{+8.4}_{-9.4}$	$-0.17^{+0.20}_{-0.22}$	$1.88^{+1.08}_{-0.88}$	$0.34^{+0.16}_{-0.15}$	94^{+13}_{-11}	$0.67^{+0.08}_{-0.11}$	960	$17.7^{+0.3}_{-0.3}$
GW241229_155844	85^{+27}_{-19}	$35.0^{+12.3}_{-8.5}$	52^{+22}_{-15}	33^{+16}_{-15}	$0.05^{+0.31}_{-0.32}$	$6.8^{+5.2}_{-3.4}$	$1.00^{+0.59}_{-0.44}$	82^{+26}_{-18}	$0.69^{+0.13}_{-0.18}$	3500	$7.6^{+0.4}_{-0.6}$
GW241230_084504	$75.6^{+12.9}_{-8.9}$	$32.4^{+5.7}_{-4.0}$	$42.4^{+9.5}_{-6.7}$	$33.5^{+7.7}_{-8.3}$	$-0.14^{+0.21}_{-0.23}$	$2.9^{+1.4}_{-1.3}$	$0.50^{+0.19}_{-0.20}$	$72.4^{+12.1}_{-8.4}$	$0.65^{+0.08}_{-0.10}$	12000	$11.8^{+0.2}_{-0.3}$
GW241230_233618	116^{+23}_{-18}	$49.3^{+10.8}_{-9.7}$	68^{+17}_{-14}	49^{+16}_{-19}	$-0.14^{+0.25}_{-0.29}$	$2.7^{+2.1}_{-1.3}$	$0.47^{+0.29}_{-0.20}$	112^{+22}_{-18}	$0.64^{+0.11}_{-0.16}$	450	$11.6^{+0.3}_{-0.4}$
GW241231_054133	$19.6^{+2.0}_{-1.2}$	$8.08^{+0.43}_{-0.22}$	$12.4^{+3.3}_{-2.8}$	$7.1^{+2.0}_{-1.3}$	$0.08^{+0.12}_{-0.08}$	$0.91^{+0.19}_{-0.33}$	$0.18^{+0.03}_{-0.06}$	$18.7^{+2.1}_{-1.3}$	$0.68^{+0.04}_{-0.05}$	130	$16.9^{+0.2}_{-0.3}$
GW250101_011205	$50.8^{+9.3}_{-6.6}$	$21.5^{+4.1}_{-3.3}$	$30.0^{+8.8}_{-5.8}$	$21.1^{+5.9}_{-7.2}$	$-0.05^{+0.24}_{-0.31}$	$3.2^{+1.7}_{-1.5}$	$0.54^{+0.23}_{-0.23}$	$48.7^{+8.8}_{-6.2}$	$0.67^{+0.10}_{-0.17}$	530	$9.1^{+0.4}_{-0.6}$
GW250104_015122	80^{+18}_{-11}	$33.9^{+8.1}_{-5.2}$	$45.8^{+11.0}_{-8.8}$	$34.5^{+10.7}_{-9.9}$	$0.11^{+0.22}_{-0.23}$	$4.8^{+2.5}_{-2.3}$	$0.76^{+0.31}_{-0.32}$	76^{+17}_{-11}	$0.73^{+0.09}_{-0.10}$	1800	$11.0^{+0.3}_{-0.4}$
GW250108_152221	90^{+17}_{-13}	$37.6^{+7.7}_{-5.5}$	54^{+15}_{-12}	36^{+10}_{-10}	$0.05^{+0.28}_{-0.28}$	$3.8^{+2.4}_{-1.9}$	$0.63^{+0.30}_{-0.28}$	86^{+17}_{-12}	$0.70^{+0.12}_{-0.15}$	770	$10.3^{+0.3}_{-0.4}$
GW250109_010541	$64.9^{+14.7}_{-8.6}$	$27.4^{+6.4}_{-3.9}$	$37.5^{+14.7}_{-7.1}$	$27.4^{+8.0}_{-8.9}$	$-0.11^{+0.27}_{-0.29}$	$3.4^{+1.7}_{-1.7}$	$0.56^{+0.22}_{-0.25}$	$62.2^{+14.0}_{-8.2}$	$0.66^{+0.12}_{-0.12}$	520	$11.2^{+0.3}_{-0.4}$
GW250109_074552	$69.2^{+10.5}_{-8.6}$	$29.6^{+4.7}_{-3.8}$	$39.0^{+8.3}_{-6.3}$	$30.2^{+6.8}_{-7.2}$	$0.07^{+0.20}_{-0.20}$	$2.3^{+1.4}_{-1.1}$	$0.41^{+0.20}_{-0.18}$	$65.9^{+9.8}_{-8.1}$	$0.72^{+0.08}_{-0.09}$	7500	$10.9^{+0.3}_{-0.5}$
GW250114_082203	$66.0^{+1.1}_{-1.2}$	$28.71^{+0.50}_{-0.51}$	$33.76^{+1.28}_{-0.90}$	$32.26^{+0.95}_{-1.47}$	$-0.03^{+0.04}_{-0.05}$	$0.40^{+0.08}_{-0.07}$	$0.09^{+0.02}_{-0.01}$	$62.9^{+1.0}_{-1.1}$	$0.68^{+0.01}_{-0.01}$	42	$76.9^{+0.0}_{-0.1}$
GW250116_015318	56^{+16}_{-11}	$23.0^{+6.9}_{-5.0}$	$34.2^{+14.5}_{-9.3}$	$21.3^{+8.8}_{-8.3}$	$0.15^{+0.31}_{-0.33}$	$5.2^{+3.9}_{-2.5}$	$0.80^{+0.47}_{-0.33}$	53^{+15}_{-11}	$0.73^{+0.12}_{-0.19}$	3000	$7.6^{+0.4}_{-0.6}$
GW250118_023225	74^{+20}_{-13}	$31.1^{+8.9}_{-6.0}$	44^{+15}_{-10}	31^{+11}_{-11}	$0.04^{+0.28}_{-0.31}$	$5.8^{+3.8}_{-2.9}$	$0.88^{+0.45}_{-0.39}$	71^{+19}_{-13}	$0.70^{+0.11}_{-0.14}$	2400	$8.8^{+0.3}_{-0.5}$
GW250118_055802	$17.5^{+4.7}_{-1.6}$	$7.36^{+0.45}_{-0.63}$	$10.3^{+7.5}_{-1.8}$	$6.9^{+1.5}_{-2.6}$	$0.11^{+0.24}_{-0.09}$	$0.94^{+0.63}_{-0.38}$	$0.19^{+0.11}_{-0.07}$	$16.6^{+4.9}_{-1.5}$	$0.72^{+0.06}_{-0.05}$	710	$9.6^{+0.4}_{-0.8}$
GW250118_170523	$67.8^{+7.9}_{-6.7}$	$29.0^{+3.5}_{-2.9}$	$38.1^{+8.1}_{-5.6}$	$29.6^{+5.4}_{-6.3}$	$0.12^{+0.18}_{-0.19}$	$1.91^{+0.80}_{-0.74}$	$0.35^{+0.12}_{-0.12}$	$64.4^{+7.3}_{-6.2}$	$0.73^{+0.07}_{-0.07}$	800	$13.1^{+0.2}_{-0.4}$
GW250119_025138	$59.9^{+8.8}_{-5.4}$	$25.7^{+4.0}_{-2.5}$	$33.8^{+6.3}_{-4.8}$	$26.7^{+5.6}_{-6.3}$	$0.06^{+0.18}_{-0.18}$	$3.1^{+1.1}_{-1.3}$	$0.52^{+0.15}_{-0.19}$	$57.1^{+8.2}_{-5.0}$	$0.72^{+0.08}_{-0.08}$	590	$13.7^{+0.2}_{-0.3}$
GW250119_190238	$21.64^{+0.55}_{-1.03}$	$9.38^{+0.14}_{-0.48}$	$11.54^{+1.95}_{-0.81}$	$9.95^{+0.77}_{-1.56}$	$0.09^{+0.05}_{-0.03}$	$0.31^{+0.29}_{-0.07}$	$0.07^{+0.06}_{-0.01}$	$20.56^{+0.57}_{-0.97}$	$0.71^{+0.02}_{-0.02}$	14	$20.4^{+0.2}_{-0.3}$

NOTE—The columns show the source-frame total mass M, source-frame chirp mass $\mathcal{M}$, source-frame component masses m_i, effective inspiral spin $\chi_{\rm eff}$, luminosity distance $D_{\rm L}$, redshift z, source-frame remnant mass $M_{\rm f}$, remnant spin $\chi_{\rm f}$, localization area $\Delta\Omega$, and SNR.

Highlights from the new candidates in GWTC-5.0 include:

- GW240925_005809 is a BBH signal with a network SNR of 31.9, enabling informative astrophysical measurements of GW detector calibration (Abac et al. 2026a). The LHO calibration inferred from the astrophysical signal is consistent with in-situ measurements, demonstrating the viability of the method as a complement to standard calibration techniques.

- GW241011_233834 is an unequal-mass BH merger, where the primary mass is about twice as massive as the secondary (Abac et al. 2025c). The primary object has a well-measured spin magnitude and its orientations that are not aligned with its orbit. These observations suggest that the primary black hole might be an outcome of a hierarchical merger and it points to the possibility that the system formed in a dense environment (Abac et al. 2025c). However, given systematics in contemporary astrophysical formation modeling, we cannot rule out other scenarios. This BBH is probably also the closest of the new O4b candidates, with a luminosity distance of $0.21^{+0.04}_{-0.04}$ Gpc.

- GW241110_124123 is another unequal-mass BH merger, with a spinning primary about twice as massive as the secondary, and might also be a result of a hierarchical merger in a dense environment (Abac et al. 2025c). However, as with GW241011_233834, we cannot rule out other scenarios.

- GW240615_113620 is the most precisely localized GW source to date (Abbott et al. 2019a, 2024; Abac et al. 2026a), with a 90% credible area of 6 deg^2.

- GW250114_082203 is a BBH signal with the highest network SNR ever observed, 76.9. This unprecedented loud signal allows us to not just measure the source properties with high precision, but also to perform detailed tests of general relativity through the BH area theorem and quasi-normal modes (Abac et al. 2025b, 2026b).

In Sections 3.1–3.3 we give further details of our inferences on masses, spins, and locations of the sources for our higher-purity candidates from O4b, highlighting sources that lie at the extremes of the parameter space. Unlike GWTC-4.0, we do not discuss matter effects in this paper since we do not find any probable new BNS or NSBH candidates in O4b. In Section 3.4 we discuss the subset of candidates which display multiple modes in their inferred source parameters. This multimodality complicates the interpretation of sources where it is present (Abbott et al. 2023a), and it is not usually possible to isolate the probable reason for multiple modes. Systematic uncertainties in our modeling affect our parameter inference for some candidates. In Section 3.5 we discuss these cases in greater detail, and present an analysis of the consistency between model-based and minimally modeled waveform reconstructions for a number of candidates.

3.1. *Masses*

The masses of a compact binary source of GWs are often the most well-constrained parameters as they are the primary determinant of the phase evolution of the signal (Abac et al. 2026a,b). The component masses are of particular interest since they indicate whether the compact objects are likely to be BHs or NSs; however, combinations of the two masses such as the chirp mass $\mathcal{M}$ or total mass M are often more precisely measured than the individual masses (e.g., Abac et al. 2026a). For example, the chirp mass is the dominant parameter controlling the rate of binary inspiral, and so it is measured well in lower-mass systems where many cycles of inspiral can be observed (Kafka 1988; Finn & Chernoff 1993; Cutler et al. 1993; Cutler & Flanagan 1994). Meanwhile, the mass ratio $q \equiv m_2/m_1 \leq 1$ is generally less well measured (Cutler et al. 1993; Cutler & Flanagan 1994; Poisson & Will 1995).

The detectors measure the redshifted masses $(1+z)m_i$, where z is the source redshift (Krolak & Schutz 1987). To recover the source-frame masses, we combine the measured redshifted masses with the inferred luminosity distance using an assumed cosmology (Ade et al. 2016). Due to the uncertainties in our estimation of the luminosity distance, source-frame mass parameters are generally less well constrained than their redshifted values. By default we report source-frame mass values, using agnostic priors as described above. Figure 2 shows the marginalized one-dimensional posteriors for the chirp mass $\mathcal{M}$ and mass ratio q of each of the O4b candidates analyzed here. Figure 3 shows the marginalized two-dimensional posteriors for the individual component masses, m_1 and m_2, as well as for the total mass M and mass ratio q. Similarly, Figure 4 shows the marginalized two-dimensional posteriors in $\mathcal{M}$ and effective inspiral spin χ_{eff}, described in Section 3.2. These inferred source-mass distributions for our newly added candidates span a wide range of total masses.

We use the inferred component masses to classify the probable nature of the binary components. For example, if one component has a mass above the maximum possible mass of a NS, we infer it to be a BH, even in the absence of other constraints on the presence of matter in the binary. Overall, we find that of the new candidates in GWTC-5.0 with a FAR $< 1\,\mathrm{yr}^{-1}$, all are consistent with being a BBH, and we do not identify any new significant BNS or NSBH candidates in O4b.

For lower mass systems, the chirp mass is the best-measured mass parameter, while for the most massive systems the total mass plays an important role. Since the chirp mass is lower for asymmetric binaries at a fixed total mass, the systems with the largest and smallest chirp masses do not necessarily correspond to the most and least massive binaries. Nevertheless, we find that the source binaries of GW241230_233618 and GW241109_115924 lie at the extremes for both mass parameters.

GW241230_233618 probably has the largest chirp mass of the candidates we analyze, with $\mathcal{M} = 49.3^{+10.8}_{-9.7}\,M_\odot$, as well as the largest total mass with $M = 116^{+23}_{-18}\,M_\odot$

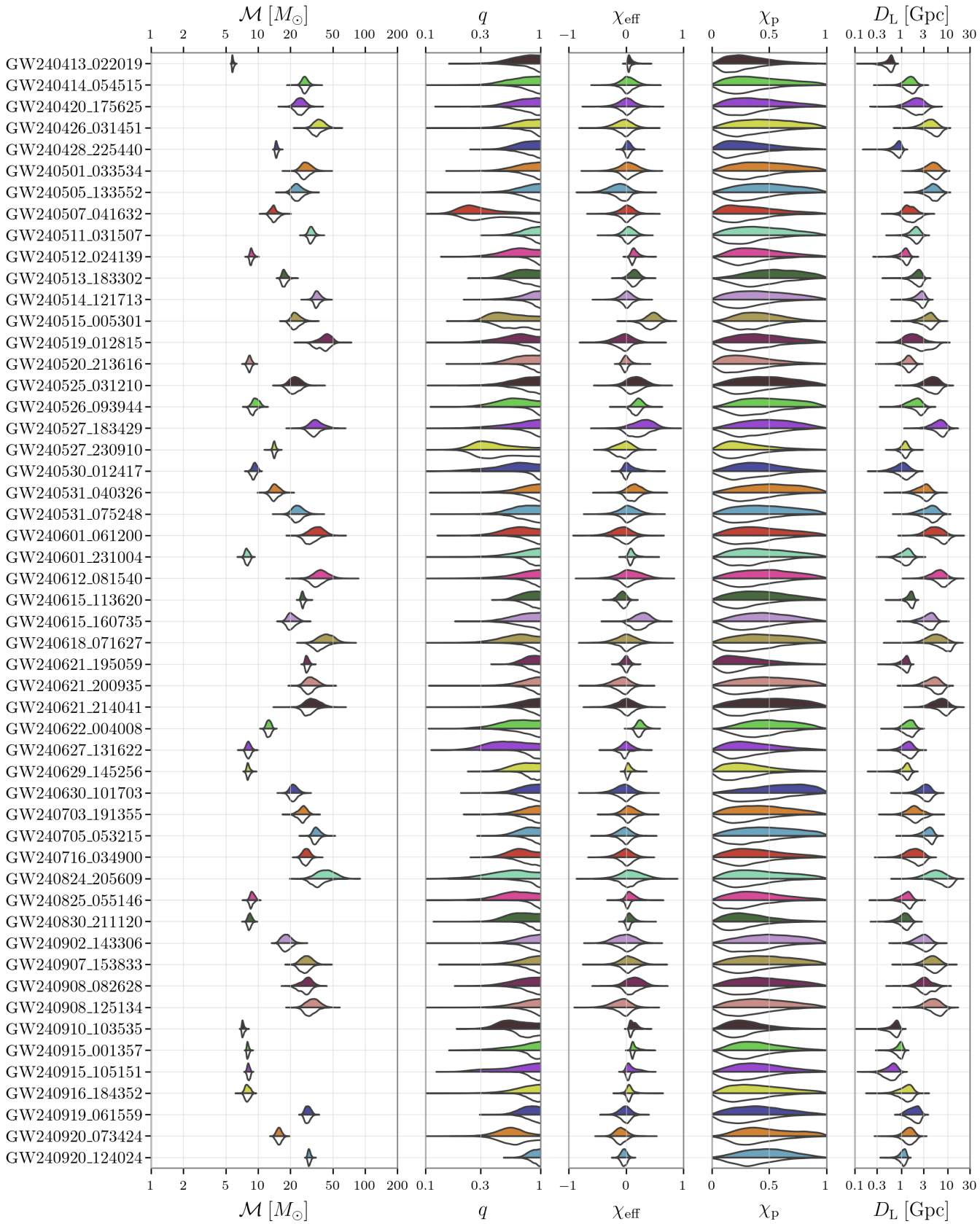
$\mathcal{M}$ [$M_\odot$]
q
$\chi_{\rm eff}$
$\chi_{\rm p}$
$D_{\rm L}$ [Gpc]
GW240413_022019
GW240414_054515
GW240420_175625
GW240426_031451
GW240428_225440
GW240501_033534
GW240505_133552
GW240507_041632
GW240511_031507
GW240512_024139
GW240513_183302
GW240514_121713
GW240515_005301
GW240519_012815
GW240520_213616
GW240525_031210
GW240526_093944
GW240527_183429
GW240527_230910
GW240530_012417
GW240531_040326
GW240531_075248
GW240601_061200
GW240601_231004
GW240612_081540
GW240615_113620
GW240615_160735
GW240618_071627
GW240621_195059
GW240621_200935
GW240621_214041
GW240622_004008
GW240627_131622
GW240629_145256
GW240630_101703
GW240703_191355
GW240705_053215
GW240716_034900
GW240824_205609
GW240825_055146
GW240830_211120
GW240902_143306
GW240907_153833
GW240908_082628
GW240908_125134
GW240910_103535
GW240915_001357
GW240915_105151
GW240916_184352
GW240919_061559
GW240920_073424
GW240920_124024

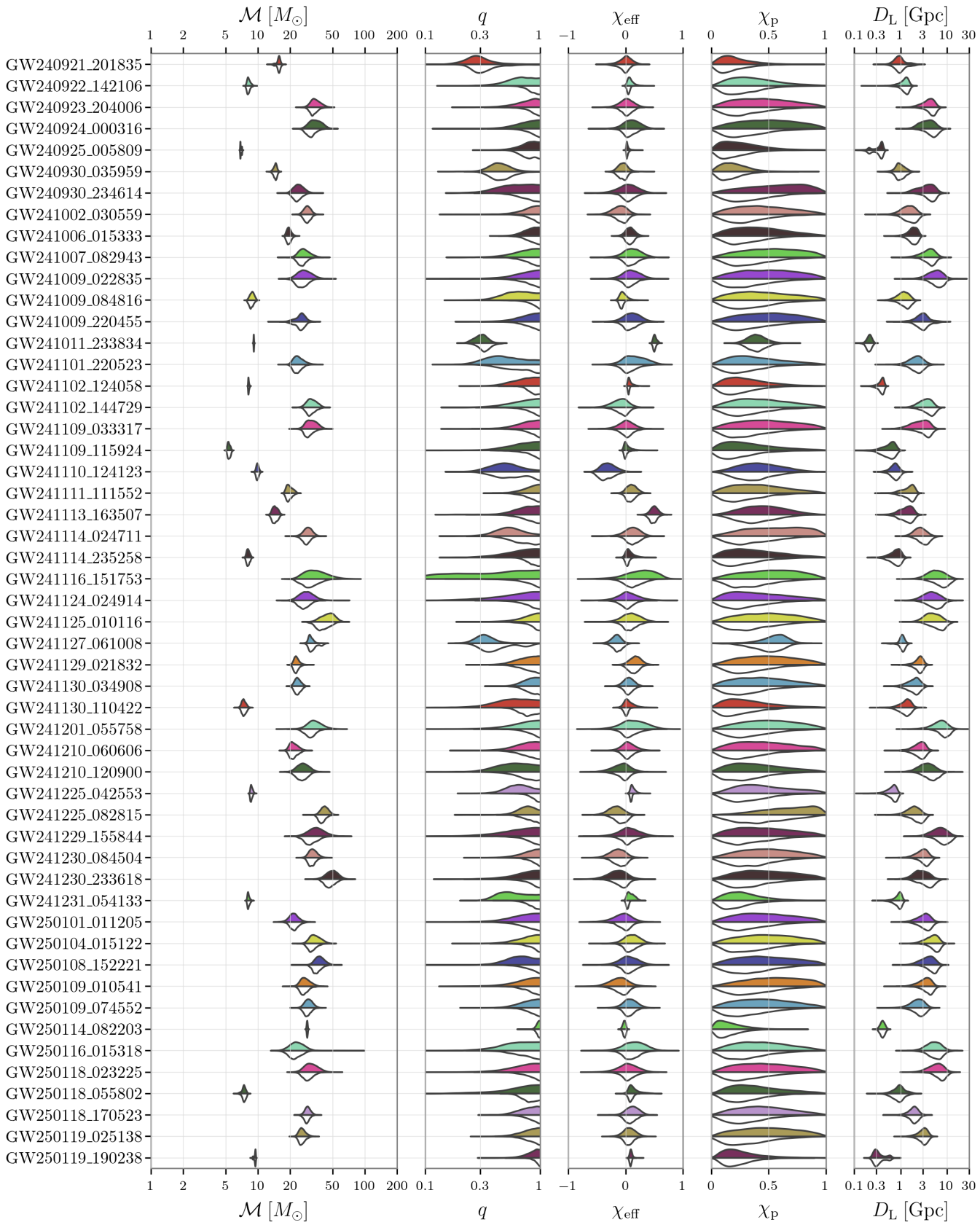

Figure 2. The marginal probability distributions for the source frame chirp mass $\mathcal{M}$, mass ratio q, effective inspiral spin $\chi_{\rm eff}$, effective precession spin $\chi_{\rm p}$, and luminosity distance $D_{\rm L}$ for O4b candidates with a FAR $< 1\,{\rm yr}^{-1}$. The height of each region is proportional to the marginal posterior probability at that value for each candidate. In addition to the upper colored region of each posterior distribution derived from the default agnostic prior (Abac et al. 2026b), we also reweight the inferred posterior distribution of our BBH candidates using a population-informed prior (default strongly-parameterised models, Table 1 of Abac et al. 2026d), and show these population-informed measurements in the lower unfilled region.

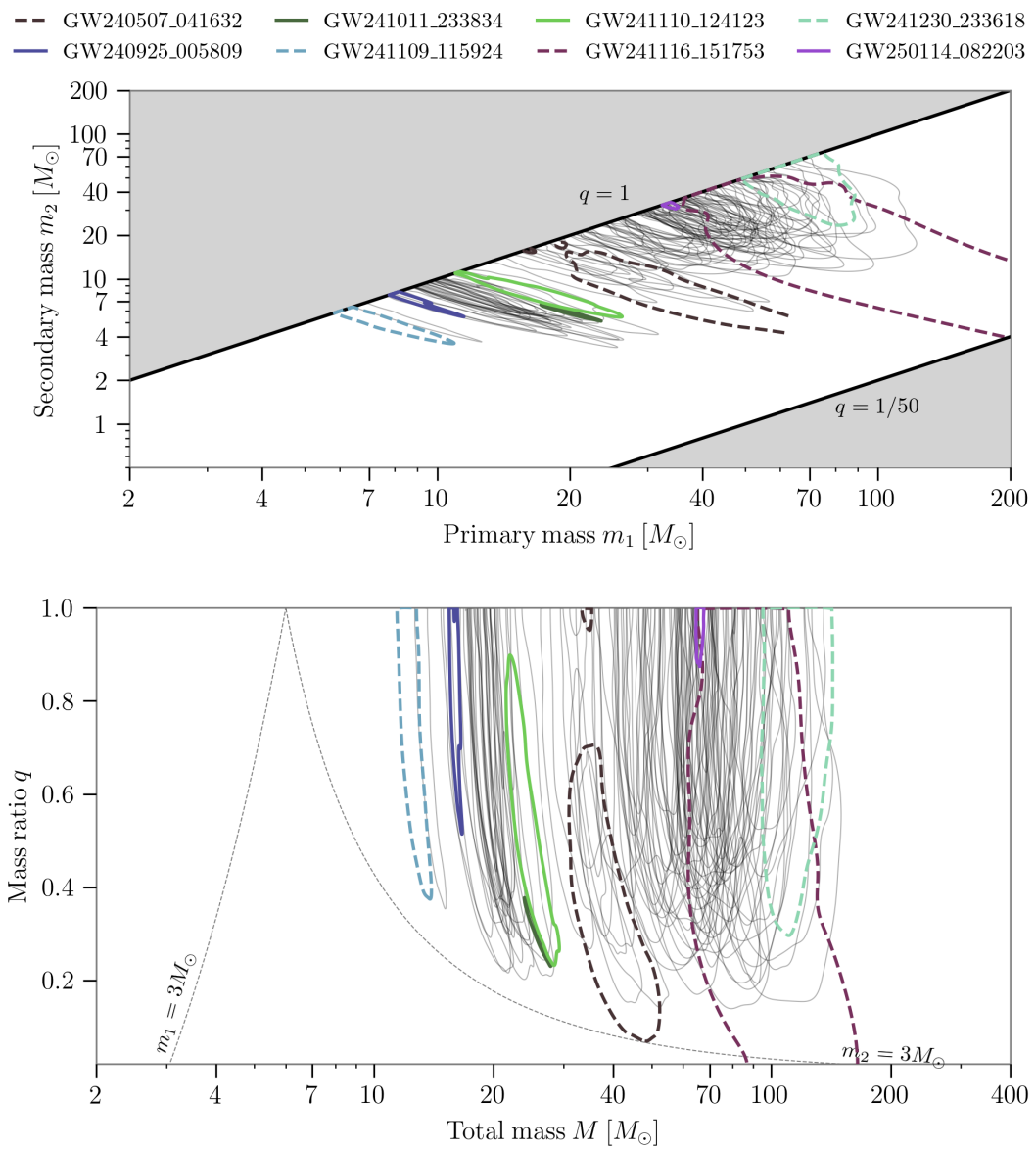

Figure 3. Credible-region contours for the O4b candidates with a FAR $< 1\,\mathrm{yr}^{-1}$, using the default agnostic prior. *Top*: Credible-region contours for the inferred primary and secondary component masses m_1 and m_2. The upper shaded region denotes the area excluded by the convention $m_1 \geq m_2$. The lower shaded region denotes the most-extreme mass-ratio prior used by parameter-estimation analyses. *Bottom:* Credible-region contours for the inferred total mass M and mass ratio q. Each contour indicates the 90% credible region for a given candidate. We use colors to highlight candidates: GW240507_041632, GW240925_005809, GW241011_233834, GW241109_115924, GW241110_124123, GW241116_151753, GW241230_233618 and GW250114_082203.

as highlighted in Figures 3 and 4. This is still less massive than the source of the most massive candidate in O4a, GW231123_135430, with $M = 236^{+29}_{-48}\,M_\odot$ (Abac et al. 2025e). In addition to GW241230_233618, three additional signals, GW240519_012815, GW240618_071627 and GW241125_010116, have sources with remnant mass $M_\mathrm{f} \geq 100\,M_\odot$ with a probability of more than 50%, and may thus be considered intermediate-mass BHs. The source of GW241109_115924 probably has the smallest chirp mass, $\mathcal{M} = 5.29^{+0.28}_{-0.20}\,M_\odot$, as well as the smallest total mass with $M = 12.51^{+1.51}_{-0.68}\,M_\odot$.

The individual components of our BBHs span masses between $5.14^{+0.90}_{-1.26}\,M_\odot$ and $70^{+57}_{-28}\,M_\odot$, with primary masses ranging from $7.3^{+2.8}_{-1.1}\,M_\odot$ for GW241109_115924 to $70^{+57}_{-28}\,M_\odot$ for GW241116_151753, and secondary masses ranging from $5.14^{+0.90}_{-1.26}\,M_\odot$ to $49^{+16}_{-19}\,M_\odot$ for GW241109_115924 and GW241230_233618, respectively.

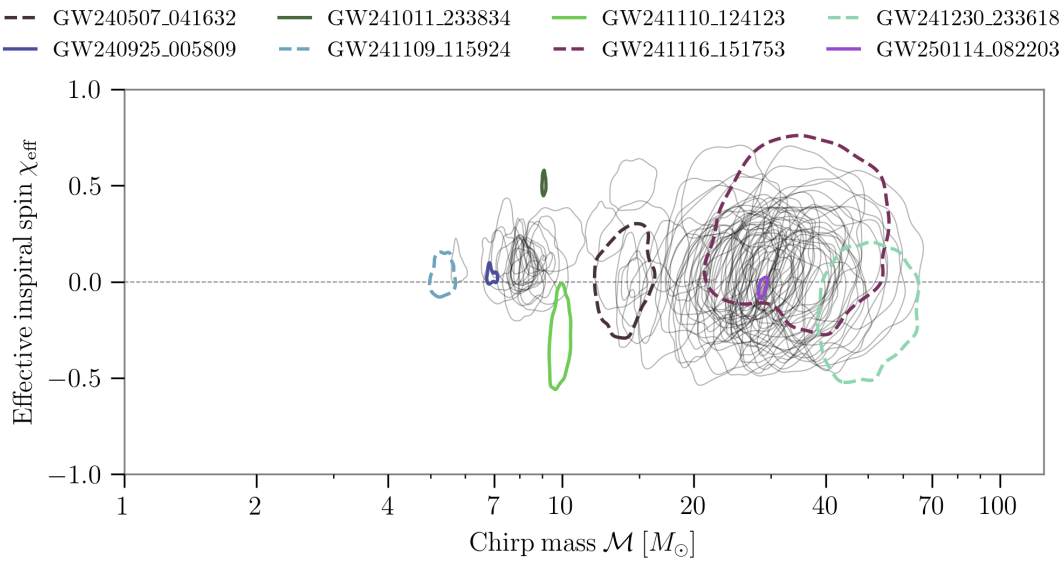

Figure 4. Credible-region contours in the chirp mass $\mathcal{M}$ and effective inspiral spin $\chi_{\rm eff}$ plane for the O4b candidates with a FAR $< 1\,{\rm yr}^{-1}$, using the default agnostic prior. Each contour indicates the 90% credible region for a given candidate. We use colors to highlight candidates GW240507_041632, GW240925_005809, GW241011_233834, GW241109_115924, GW241110_124123, GW241116_151753, GW241230_233618 and GW250114_082203.

The BBH mass distribution inferred using all the candidates in GWTC-5.0 is discussed in depth in Abac et al. (2026d).

The sources of several candidates have notable posterior support for unequal masses relative to our default agnostic prior. GW240507_041632 has the most support with a mass ratio of $q = 0.27^{+0.47}_{-0.10}$. In addition, GW241116_151753 has mass ratio of $q = 0.37^{+0.55}_{-0.27}$; the apparent support for unequal masses in this result could be attributed to the uninformative nature of the posterior as well as the presence of non-negligible waveform systematics, as discussed further in Section 3.5. Along with these two candidates highlighted in Figures 3 and 4, other unequal-mass systems include GW240921_201835, GW240930_035959 and GW241127_061008. Additionally, GW241110_124123 and GW241011_233834, whose component spins will be discussed below, have support for asymmetric masses, with $q = 0.49^{+0.34}_{-0.19}$ and $q = 0.31^{+0.07}_{-0.06}$, respectively (Abac et al. 2025c).

3.2. *Spins*

Compared to the masses, spins have a weaker impact on the GW emission and are more difficult to measure from observations (Poisson & Will 1995; Baird et al. 2013; Pratten et al. 2020; Chatziioannou et al. 2015; Vitale et al. 2014; Farr et al. 2016; Vitale et al. 2017a; Abbott et al. 2016c; García-Bellido et al. 2021; Green et al. 2021; Hoy et al. 2025). The component spins of compact binaries, $\boldsymbol{\chi}_1$ and $\boldsymbol{\chi}_2$, are typically poorly constrained since the leading-order spin contribution to the GW signal is determined by mass-weighted combinations of the components (Damour 2001; Blanchet 2014; Pürrer et al. 2016; Ng et al. 2018; Zevin et al. 2020). Here, we focus on two mass-weighted spin parameters: the effective inspiral spin $\chi_{\rm eff}$ and the effective precession spin $\chi_{\rm p}$ (Abac et al. 2026a).

The effective inspiral spin $\chi_{\rm eff}$ (Ajith et al. 2011; Santamaría et al. 2010) is a mass-weighted combination of the components of the spin aligned with the Newtonian orbital angular momentum. It appears in the leading-order spin term due to spin-orbit coupling at 1.5 post-Newtonian order, and is approximately conserved throughout the inspiral (Racine 2008). Positive and negative $\chi_{\rm eff}$ indicate that there is net spin aligned or anti-aligned, respectively, with the orbital angular momentum.

The effective precession spin $\chi_{\rm p}$ (Schmidt et al. 2015) measures the mass-weighted in-plane spin component that contributes to spin precession (Apostolatos et al. 1994; Kidder 1995). It is bounded between 0 and 1, with $\chi_{\rm p} = 0$ indicating no spin precession. This parameter is typically weakly constrained (Vitale et al. 2017a; Pratten et al. 2020; Green et al. 2021; Krishnendu & Ohme 2022), and inferences on $\chi_{\rm p}$ are often dominated by the prior.

The spin orientations θ_i of a binary are of particular interest for the insight they provide into its evolutionary history (Vitale et al. 2017b; Fishbach et al. 2017; Stevenson et al. 2017; Talbot & Thrane 2017; Wysocki et al. 2019; Zevin et al. 2021). Compact binaries form via a myriad of channels, but can be broadly classified as either dynamically assembled or formed via isolated binary evolution. Roughly speaking, in dynamically formed binaries the spins are expected to be isotropically oriented, while binaries formed in isolation are expected to have spins preferentially aligned with the orbital axis. Significant support for large $\chi_{\rm p}$ or negative $\chi_{\rm eff}$ is therefore more consistent with dynamically formed binaries than those formed in isolation. Further discussion of the connec-

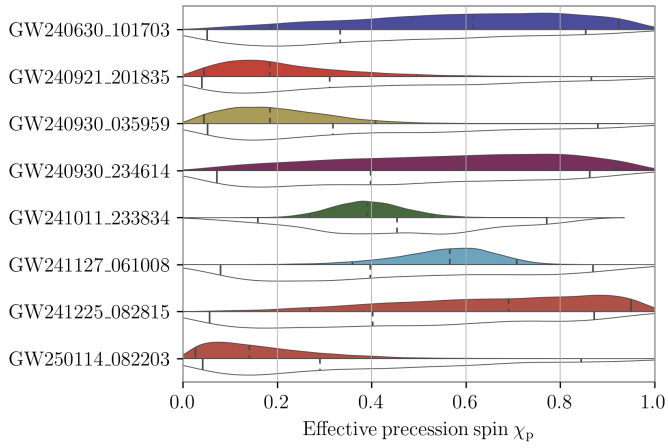

Figure 5. Posterior (upper, coloured); and the effective prior (lower, white) probability distributions for the dimensionless effective precession spin $\chi_{\rm p}$ for candidates GW240630_101703, GW240921_201835, GW240930_035959, GW240930_234614, GW241011_233834, GW241127_061008, GW241225_082815, and GW250114_082203. Vertical lines mark the median and symmetric 90% credible interval for the distributions. These candidates are those with the greatest deviation between the posterior distribution and the effective prior over $\chi_{\rm p}$, out of the new candidates presented here.

tion between spin orientations and compact binary formation channels is given in Abac et al. (2026d).

For most significant O4b candidates, the sources' inferred spins are consistent with $\chi_{\rm eff} = 0$, as seen in Figures 2 and 4. However, some candidates have sources with $\chi_{\rm eff} \geq 0$ with greater than 90% probability. The candidate with the highest and second highest $\chi_{\rm eff}$ values are GW241113_163507 with $\chi_{\rm eff} = 0.50^{+0.11}_{-0.11}$ and GW240515_005301 with $\chi_{\rm eff} = 0.47^{+0.17}_{-0.19}$, respectively. Some other candidates with support for $\chi_{\rm eff} \geq 0$ include GW240527_183429, GW240615_160735, GW240622_004008, GW241011_233834 and GW241116_151753. We find fewer candidates for which, $\chi_{\rm eff} < 0$, with greater than 90% probability: the two candidates with the most negative $\chi_{\rm eff}$ median values are GW241110_124123 and GW241230_233618 with $\chi_{\rm eff} = -0.31^{+0.23}_{-0.18}$ and $\chi_{\rm eff} = -0.14^{+0.25}_{-0.29}$, respectively.

Figure 5 shows the $\chi_{\rm p}$ posterior probability distribution compared to the prior distribution after conditioning on the $\chi_{\rm eff}$ measurement (Abbott et al. 2019a), for a selection of candidates. The $\chi_{\rm p}$ posterior would be the same as the conditioned prior if no information about the in-plane spin components was extractable from the signal; the selected candidates show the greatest differences between these two distributions. For most of the candidates, the $\chi_{\rm p}$ posteriors are broad and uninformative. The two events with the highest $\chi_{\rm p}$ values are GW241225_082815 and GW240630_101703 with values $\chi_{\rm p} = 0.70^{+0.25}_{-0.42}$ and $\chi_{\rm p} = 0.63^{+0.30}_{-0.44}$, respectively.

Figure 6 shows the posterior distribution of the source component spin magnitudes χ_i and tilt angles θ_i inferred for a subset of the analyzed candidates. These candidates are highlighted due to their somewhat-constrained spin posteriors, exceptional nature, or presence of systematic differences in the inferences made with different waveform models (Section 3.5). In particular, GW241011_233834 and GW241127_061008 stand out as exhibiting significant spin in the primary object, with the latter showing strong evidence for an anti-aligned primary spin. In many other cases the component spins of the sources are poorly measured and our posteriors are similar to our priors. For those binaries where $\chi_{\rm eff}$ is constrained to be relatively small, the posteriors of the component spins may be concentrated in the equatorial plane even without positive evidence for precession, due to ruling out spins either relatively aligned or anti-aligned with the orbital angular momentum (Abbott et al. 2017c).

Of the sources analyzed from O4b, GW241113_163507 is inferred to have the highest primary spin magnitude, $\chi_1 = 0.80^{+0.17}_{-0.38}$. Other systems that were inferred to have a high primary spin are the source of GW241225_082815 and GW241011_233834 with primary spin magnitude of $\chi_1 = 0.76^{+0.22}_{-0.60}$ and $0.76^{+0.07}_{-0.07}$, respectively.

The final spin $\chi_{\rm f}$ of the remnant BH following coalescence has contributions from the orbital angular momentum at merger and the spin angular momenta of the binary components. It is determined for our BBH candidates from the inferred component masses and spins, using fits to numerical relativity simulations (Abac et al. 2026b). The candidate with the highest $\chi_{\rm f}$ at 90% probability is GW241113_163507 with $\chi_{\rm f} = 0.85^{+0.04}_{-0.04}$. This probability is quantified by drawing samples many times from the posterior distributions of events, and comparing how often each event has the highest $\chi_{\rm f}$ value.

3.3. *Localization*

As GW detectors continue to improve their sensitivity, we are able to detect GW sources both in our cosmic neighborhood and out to increasingly large distances. Nevertheless, during O4b, several nearby BBH signals were observed. The source which is probably the closest of these is GW241011_233834 (Abac et al. 2025c), with $D_{\rm L} = 0.21^{+0.04}_{-0.04}$ Gpc. However, this credible range of the luminosity distance of the source overlaps with the credible range for GW240925_005809 (Abac et al. 2026a), $D_{\rm L} = 0.36^{+0.06}_{-0.17}$ Gpc. The latter candidate has a large network SNR of 31.9 and is a lower mass BBH with $M = 16.01^{+0.62}_{-0.40}\,M_\odot$. GW250114_082203, the highest-SNR GW candidate detected in O4b, is inferred to be at $D_{\rm L} = 0.40^{+0.08}_{-0.07}$ Gpc.

The farthest source of the candidates analyzed is probably for GW241201_055758, which is inferred to lie at $D_{\rm L} = 7.1^{+4.7}_{-3.8}$ Gpc. As there are several candidates with sources at similar distances, GW241201_055758 has only a 14% probability of having the most-distant source. The next most probable to have the most-distant source is GW241229_155844 at $D_{\rm L} = 6.8^{+5.2}_{-3.4}$ Gpc, with a 14% probability of being the most distant candidate. These distant candidates are at compara-

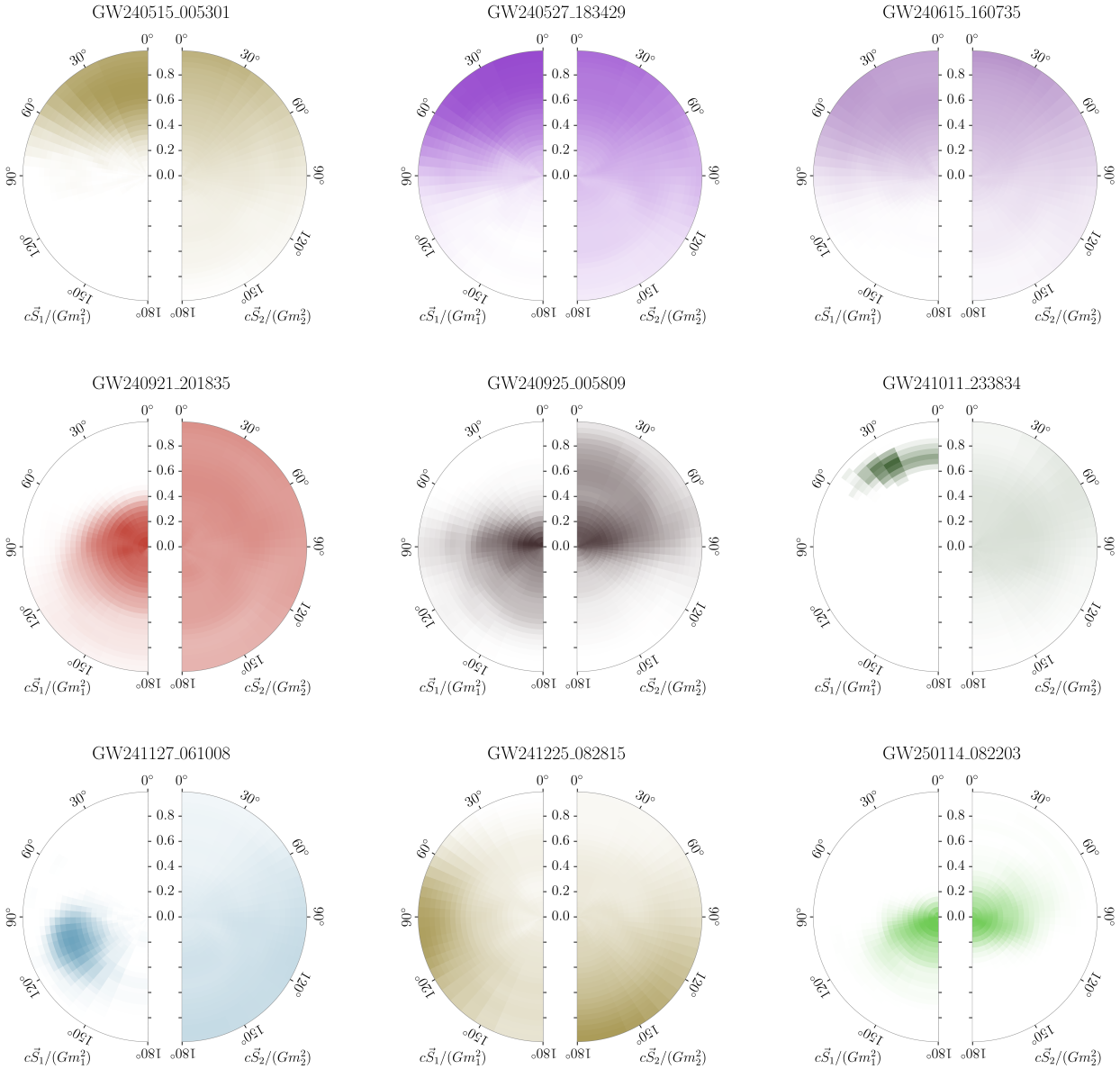

Figure 6. Posterior probability distributions for the dimensionless component spins $\boldsymbol{\chi}_1 = c\mathbf{S}_1/(Gm_1^2)$ and $\boldsymbol{\chi}_2 = c\mathbf{S}_2/(Gm_2^2)$ (with $\mathbf{S}_1$ and $\mathbf{S}_2$ the spin vectors of the components) relative to the orbital plane, marginalized over azimuthal angles, for candidates GW240515_005301, GW240527_183429, GW240615_160735, GW240921_201835, GW240925_005809, GW241011_233834, GW241127_061008, GW241225_082815, and GW250114_082203. In these plots, the histogram bins are constructed linearly in spin magnitude and the cosine of the tilt angles such that they contain equal prior probability.

ble luminosity distances to the farthest sources detected in the O4a with a FAR $< 1\,\mathrm{yr}^{-1}$, for example GW230704_212616 and GW231119_075248 with $D_\mathrm{L} = 7.2^{+6.1}_{-4.2}\,\mathrm{Gpc}$ and $D_\mathrm{L} = 6.7^{+5.5}_{-3.7}\,\mathrm{Gpc}$, respectively (Abac et al. 2025a).

The inferred sky location of each candidate depends largely on the number of observing GW detectors at the time of the detection (Schutz 1986; Fairhurst 2009, 2011; Nissanke et al. 2011; Veitch et al. 2012; Nissanke et al. 2013; Kasliwal & Nissanke 2014; Grover et al. 2014; Singer et al. 2014; Berry et al. 2015; Abbott et al. 2020). Unlike O4a where only the two LIGO detectors were operating, during O4b the Virgo detector was additionally operating with significant sensitivity to CBC signals. As a result, 14 candidates have a source localization covering $100\,\mathrm{deg}^2$ or less (90% credible level), 5 of which are constrained at least as narrowly as GW170817 ($\Delta\Omega = 16\,\mathrm{deg}^2$; Abbott et al. 2019d). In particular, the best localized candidate is GW240615_113620 with $\Delta\Omega = 6\,\mathrm{deg}^2$, which is the best localization of any GW candidate to date (Abbott et al. 2019a, 2021b, 2023a; Abac et al. 2025a, 2026a).

The three-dimensional volume localization (Singer et al. 2016; Del Pozzo et al. 2018), like the sky localization, is drastically improved in O4b as compared to O4a for candidates observed by the three-detector network. Broadly speaking, nearby candidates have the best volume localization, provided they are observed in multiple detectors. The two candidates with the tightest three-dimensional localization from O4b, GW241011_233834 with a 90% credible volume of $59000\ \mathrm{Mpc}^3$ and (GW250119_190238) with a 90% credible volume of $170000\ \mathrm{Mpc}^3$, are the two closest. The highest SNR candidate GW250114_082203 also has comparatively small localization in volume, with a 90% credible volume of $430000\ \mathrm{Mpc}^3$.

3.4. *Multimodality*

A few candidates display multimodal posteriors in this release based on the default priors used, consistent with similar behaviors noted in previous catalogs (Abbott et al. 2023a; Abac et al. 2025a). Such multimodality often reflects the intrinsic complexity of the waveform likelihood surface, particularly in regions where signal models exhibit stronger effects of the higher-order multipole moments (Nitz et al. 2021; Estellés et al. 2022; Mehta et al. 2022; Chia et al. 2022) or spin precession effects (Abbott et al. 2019d, 2020). However, the presence of glitches (Powell 2018; Chatziioannou et al. 2021; Ashton et al. 2022; Soni et al. 2025), noise fluctuations at low SNR (Huang et al. 2018), or the overlap of concurrent signals (Relton & Raymond 2021) can also give rise to multiple posterior modes, though the last remains unlikely at current detector sensitivities. Along with other possible factors, these diverse origins contribute to some degree of multimodality across the catalog.

Most mass posterior distributions are unimodal, as shown in Figure 2. GW240507_041632 and GW240916_184352 are notable exceptions, each exhibiting bimodality in the luminosity distance D_L, and therefore the redshifted chirp mass $(1+z)\mathcal{M}$ posteriors. As redshift uncertainties tend to broaden our mass estimates in the source frame, these bimodalities are less apparent in the source chirp mass $\mathcal{M}$ posterior. Additionally, while the measured redshifted chirp masses of GW240925_005809 and GW250119_190238 are unimodal, there is bimodality in the source frame chirp mass, driven by the bimodality in the inferred redshift (Abac et al. 2026a).

Multimodality in mass parameters can correlate with multiple modes in other parameters, particularly the spin quantities $\chi_{\rm eff}$ and $\chi_{\rm p}$. However, GW240507_041632, GW240916_184352 and GW241116_151753 all have network matched-filter SNRs below 10, and their $\chi_{\rm eff}$ posteriors are consequently too broad to clearly identify any such correlation.

The degree of multimodality can depend on the waveform model and sampler combination used in analysis. For example, for GW241116_151753 in Figure 7 the bimodality in total mass M and mass ratio q is present with IMRPhenomXPHM_SpinTaylor, but is more subtle for the IMRPhenomXPNR and absent with SEOBNRv5PHM.

3.5. *Waveform systematics*

In this subsection, we assess the impact of waveform-model and sampler-related systematics on the inferred source properties of the candidates in our catalog. Consistent with previous analyses (Abbott et al. 2016d, 2019a,d, 2021b), we find that differences between waveform models and sampling methods are generally small compared to the statistical uncertainties, and are often most noticeable in parameters related to the spin.

The results presented here are derived from parameter-estimation analyses employing multiple waveform models and two independent sampling codes, Bilby and RIFT, as described in Abac et al. (2026b). For each BBH candidate, the Bilby sampler is used to analyze the data with the IMRPhenomXPHM_SpinTaylor and the IMRPhenomXPNR waveform models. The NRSur7dq4 model is also used with the Bilby sampler, but is only adopted for candidates with source properties within the calibration domain of the model. The SEOBNRv5PHM model is used with either Bilby or RIFT, depending on the configuration selected for the analysis presented here. Additionally, DINGO (Dax et al. 2021) and BILBY-MCMC (Ashton & Talbot 2021) were used to cross-check results for a selection of candidates. Consequently, variations between posterior distributions from different configurations generally reflect a combination of waveform-model and sampler systematics. Because not all waveform models are used with both samplers for all candidates, and only a single sampler configuration is retained for each candidate in the reported results, it is not possible, in general, to unambiguously disentangle these two sources of systematic uncertainty.

For a small number of candidates, we observe more pronounced differences between posterior distributions obtained with different waveform models and analysis configurations. Most importantly, we find that even in these cases the differences in posteriors do not substantially alter our previous statements about candidates of special interest that stand out due to extreme values of masses, spins or distance.

The overall behavior observed for the O4b candidates is qualitatively consistent with that reported for the O4a candidates in GWTC-4.0 (Abac et al. 2025a), where waveform-dependent differences were likewise generally small compared to the statistical uncertainties, but became more noticeable for high-mass, high-SNR, unequal-mass, or systems with strong spin precession. For new candidates reported in GWTC-4.0, the most pronounced cases included GW231123_135430 and GW231028_153006, both of which combined high total masses with significant spin effects. Similar trends are observed in the present GWTC-5.0 for new O4b candidates.

These systematic differences are expected from the current state of waveform modeling. Numerical-relativity simulations remain relatively sparse in regions of parameter space involving large spins, large mass ratios, and generic spin orientations, particularly for long inspirals. As a consequence waveform models must extrapolate beyond the regions where

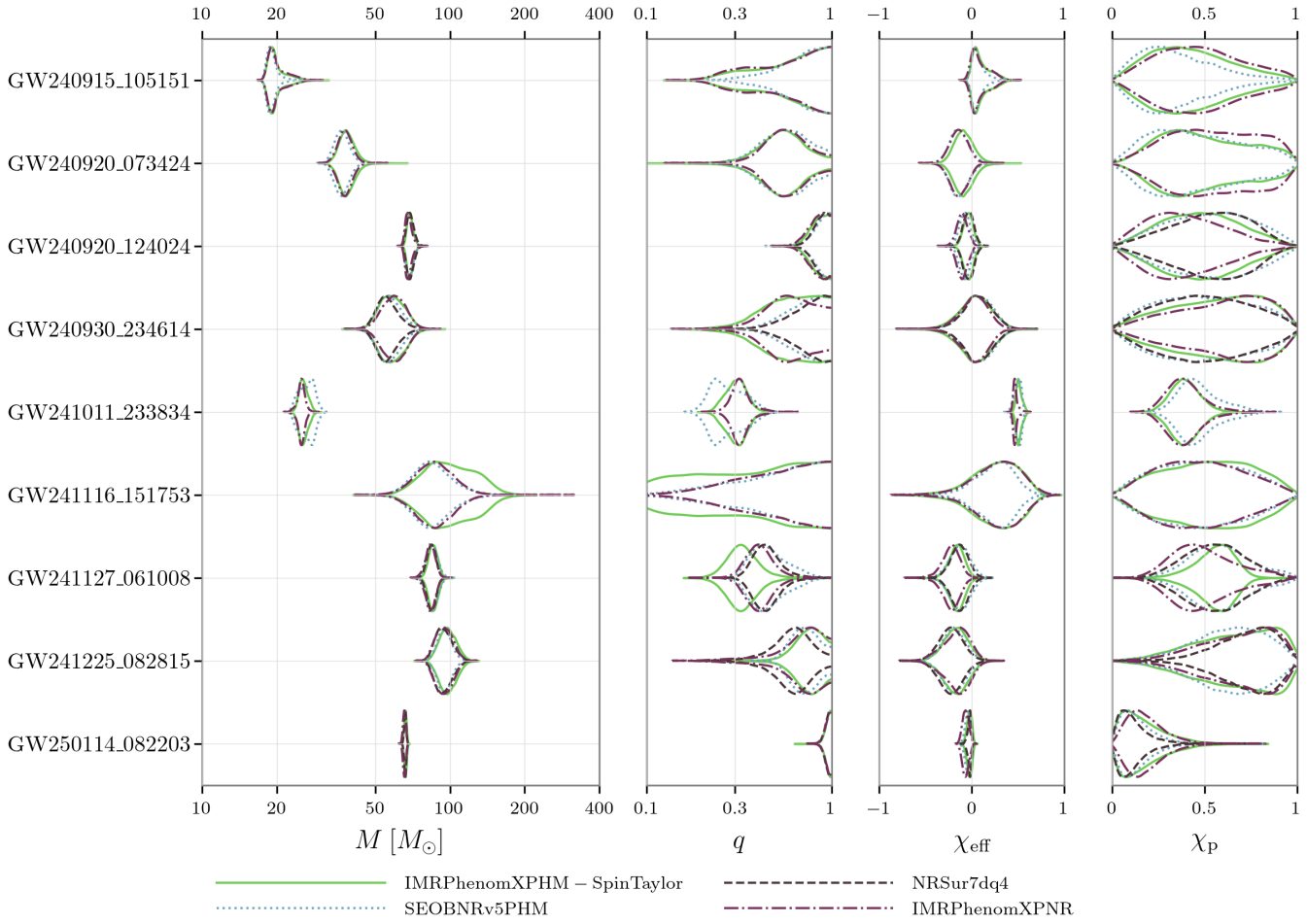

Figure 7. The marginal probability distributions for the (source-frame) total mass M, mass ratio q, effective inspiral spin $\chi_{\rm eff}$, and effective precession spin $\chi_{\rm p}$ for nine O4b candidates which show significant waveform systematics.

they are directly informed by simulations. Among the waveform models considered here, NRSUR7DQ4 is the only one that is fully calibrated to numerical-relativity simulations with spin precession, but its applicability is restricted to a limited region of parameter space. The IMRPHENOMXPNR and SEOBNRV5PHM waveform models employ a limited calibration to numerical-relativity simulations with spin precession, and IMRPHENOMXPHM_SPINTAYLOR lacks any such calibration, but employs a twisting-up approximation together with the stationary-phase approximation to model precession in the frequency domain.

A recent reanalysis of the new candidates first reported in GWTC-4.0 using the IMRPHENOMXPNR waveform model (Hamilton et al. 2026) also found broadly consistent behavior, with the largest discrepancies between waveform models concentrated in high-mass, high-spin, or systems with strong spin precession.

We illustrate the differences we find by plotting selected posterior distributions for all models in Figure 7. In Table 4, we also show the median values and 90% credible intervals for these source parameters as inferred by each waveform model used in our analysis, and each parenthesis indicates which sampler has been used with a given waveform model. The candidates identified as exhibiting the most significant differences in posteriors between analyses are:

- GW240915_105151 is a lower total mass candidate with detector frame mass $21.54^{+5.59}_{-0.69}\,M_\odot$. The analyses with three waveform models differ in their support for high $\chi_{\rm p}$, with SEOBNRV5PHM showing the least support and IMRPHENOMXPNR the most. Several other quantities also show mild deviations between analyses; in particular the analysis with SEOBNRV5PHM shows less support for unequal masses.

- GW240920_073424 was observed with all three detectors. The analyses with three waveform models show only mild systematics in several quantities, the principal discrepancy is that the analysis with IMRPHENOMXPNR supports higher values of $\chi_{\rm p}$.

- GW240920_124024 was observed in the two LIGO detectors, with the second highest SNR in O4b, $37.0^{+0.1}_{-0.1}$, and consequently has generally well-constrained parameters. Glitch mitigation was per-

formed for the LLO detector (Table 10). The total mass and chirp mass are consistent across waveform models. The effective inspiral spin $\chi_{\rm eff}$ is constrained to be close to zero by all models, although IMRPHENOMXPNR favors more negative values. More noticeable differences appear in the effective precession spin $\chi_{\rm p}$, but all $\chi_{\rm p}$ posteriors are broad.

- GW240930_234614 was detected only in the two LIGO detectors, and only by the CWB-BBH pipeline, with a relatively low SNR of $9.0^{+0.7}_{-0.6}$. In this case, parameter-estimation results have been obtained with all four waveform models. Pronounced deviations can be observed in masses, mass ratio, and $\chi_{\rm p}$, where the frequency-domain models show more support for unequal masses while the time-domain models show more support for equal masses. The frequency-domain models also exhibit differences in the inclination, with less support for close to face-on or face-off viewing angle, and correspondingly smaller distance.

- GW241011_233834 was observed in the LHO and Virgo detectors with a high SNR of $35.8^{+0.1}_{-0.1}$, and was previously presented in Abac et al. (2025c), emphasizing the large and well-measured primary spins, non-negligible spin-orbit misalignment with a well constrained $\chi_{\rm p}$, and unequal mass ratio. As already discussed in Abac et al. (2025c), due to the large SNR, high spins, and unequal masses, posteriors show evidence for waveform systematics, as expected, although different waveform models yield qualitatively similar conclusions. The analysis with SEOBNRV5PHM picks up even more unequal masses than the analyses with the frequency-domain models, and finds a broader posterior for the total mass, which extends to higher masses. For the chirp mass, the analysis with IMRPHENOMXPNR prefers smaller values, and the one with IMRPHENOMXPHM_SPINTAYLOR larger ones. The effective inspiral spin $\chi_{\rm eff}$ is well measured by all waveform and sampler combinations with broadly consistent results, however, the posterior distributions vary significantly in shape. The posterior for $\chi_{\rm p}$ with SEOBNRV5PHM is broader and extends to higher values.

- GW241116_151753 is a low SNR ($8.4^{+0.6}_{-0.6}$) candidate observed in all three detectors, with weakly constrained posterior distributions, which has been highlighted above as showing the heaviest component mass in O4b, $m_1 = 70^{+57}_{-28}\,M_\odot$. Multimodality for this candidate has already been discussed above in Sec. 3.4. The candidate has been highlighted above for its support for highly asymmetric masses; however, the posterior for the mass ratio q is broad, and almost flat with IMRPHENOMXPHM_SPINTAYLOR, as illustrated in Figure 3. The total mass is poorly constrained; again the analysis with IMRPHENOMXPHM_SPINTAYLOR disagrees with other results and has support for larger total mass. The inferred luminosity distance also shows variation, and the analysis with IMRPHENOMXPNR favors somewhat larger distances. These differences are consistent with the limited information content of the signal.

- GW241127_061008 was observed in all three detectors, with a high network SNR of $31.2^{+0.1}_{-0.2}$. As illustrated in Figures 2 and 5 for $\chi_{\rm p}$ and in Figure 6 for the component spins, this candidate has well measured spin misalignment with the orbital angular momentum. While the posteriors for different analyses show significant variations, the $\chi_{\rm eff}$ and $\chi_{\rm p}$ results do agree qualitatively. Similarly, the source is confidently identified as having asymmetric masses. Analyses with the frequency-domain waveforms measure negative $\chi_{\rm eff}$, while for the time-domain models $\chi_{\rm eff}$ is higher and not constrained to be negative. Different analyses agree well on the high total mass.

- GW241225_082815 was observed with the LHO and Virgo detectors and has previously been highlighted as having high $\chi_{\rm p}$ and high primary spin χ_1. The candidate also shows support for unequal masses, in particular with NRSUR7DQ4, while the two frequency-domain models show the largest support for equal masses. The analysis with SEOBNRV5PHM shows reduced support for high $\chi_{\rm p}$ compared to the other analyses.

- GW250114_082203 has the largest SNR ever observed and has already been discussed in Abac et al. (2025b). As expected from the high SNR, the analyses for this candidate do show systematic differences, which are most apparent in its spin parameters.

Table 4. Median and 90% symmetric credible interval for selected source properties as inferred by different waveform models and samplers.

Candidate	Model	$\mathcal{M}$ $[M_\odot]$	q	$\chi_{\rm eff}$	$\chi_{\rm p}$	$D_{\rm L}$ [Gpc]
GW240915_105151	IMRPHENOMXPHM_SPINTAYLOR (BILBY)	$8.07^{+0.40}_{-0.32}$	$0.65^{+0.32}_{-0.39}$	$0.07^{+0.22}_{-0.09}$	$0.40^{+0.41}_{-0.29}$	$0.63^{+0.26}_{-0.28}$

Table 4 *continued*

Table 4 *(continued)*

Candidate	Model	$\mathcal{M}$ $[M_\odot]$	q	$\chi_{\rm eff}$	$\chi_{\rm p}$	$D_{\rm L}$ [Gpc]
	NRSur7dq4 (Bilby)	$8.07^{+0.40}_{-0.32}$	$0.65^{+0.32}_{-0.39}$	$0.07^{+0.22}_{-0.09}$	$0.40^{+0.41}_{-0.29}$	$0.63^{+0.26}_{-0.28}$
	SEOBNRv5PHM (RIFT)	$8.03^{+0.40}_{-0.33}$	$0.72^{+0.25}_{-0.35}$	$0.05^{+0.15}_{-0.07}$	$0.31^{+0.40}_{-0.23}$	$0.65^{+0.27}_{-0.28}$
	IMRPhenomXPNR (Bilby)	$8.07^{+0.39}_{-0.31}$	$0.63^{+0.33}_{-0.37}$	$0.06^{+0.21}_{-0.09}$	$0.46^{+0.41}_{-0.32}$	$0.62^{+0.25}_{-0.27}$
GW240920_073424	IMRPhenomXPHM_SpinTaylor (Bilby)	$15.6^{+1.5}_{-1.3}$	$0.54^{+0.31}_{-0.22}$	$-0.09^{+0.19}_{-0.16}$	$0.47^{+0.44}_{-0.30}$	$1.44^{+0.62}_{-0.55}$
	NRSur7dq4 (Bilby)	$15.6^{+1.5}_{-1.3}$	$0.54^{+0.31}_{-0.22}$	$-0.09^{+0.19}_{-0.16}$	$0.47^{+0.44}_{-0.30}$	$1.44^{+0.62}_{-0.55}$
	SEOBNRv5PHM (RIFT)	$15.0^{+1.4}_{-1.1}$	$0.57^{+0.33}_{-0.22}$	$-0.14^{+0.17}_{-0.15}$	$0.43^{+0.44}_{-0.31}$	$1.69^{+0.59}_{-0.61}$
	IMRPhenomXPNR (Bilby)	$15.5^{+1.4}_{-1.3}$	$0.57^{+0.31}_{-0.19}$	$-0.14^{+0.15}_{-0.16}$	$0.55^{+0.37}_{-0.37}$	$1.44^{+0.60}_{-0.51}$
GW240920_124024	IMRPhenomXPHM_SpinTaylor (Bilby)	$29.8^{+1.7}_{-1.2}$	$0.86^{+0.12}_{-0.17}$	$-0.04^{+0.08}_{-0.09}$	$0.47^{+0.35}_{-0.31}$	$1.09^{+0.22}_{-0.32}$
	NRSur7dq4 (Bilby)	$30.0^{+1.9}_{-1.5}$	$0.88^{+0.10}_{-0.15}$	$-0.04^{+0.09}_{-0.09}$	$0.55^{+0.29}_{-0.36}$	$1.08^{+0.22}_{-0.33}$
	SEOBNRv5PHM (Bilby)	$29.7^{+1.9}_{-1.4}$	$0.89^{+0.10}_{-0.18}$	$-0.08^{+0.09}_{-0.09}$	$0.54^{+0.34}_{-0.37}$	$1.06^{+0.24}_{-0.34}$
	IMRPhenomXPNR (Bilby)	$29.4^{+1.8}_{-1.2}$	$0.85^{+0.13}_{-0.18}$	$-0.11^{+0.10}_{-0.09}$	$0.38^{+0.38}_{-0.28}$	$1.06^{+0.22}_{-0.34}$
GW240930_234614	IMRPhenomXPHM_SpinTaylor (Bilby)	$23.9^{+4.9}_{-3.7}$	$0.61^{+0.34}_{-0.29}$	$0.04^{+0.27}_{-0.30}$	$0.59^{+0.32}_{-0.44}$	$3.6^{+2.6}_{-2.0}$
	NRSur7dq4 (Bilby)	$23.6^{+4.9}_{-3.4}$	$0.77^{+0.20}_{-0.30}$	$0.06^{+0.25}_{-0.27}$	$0.49^{+0.39}_{-0.36}$	$4.4^{+2.1}_{-2.1}$
	SEOBNRv5PHM (RIFT)	$24.0^{+5.0}_{-3.6}$	$0.74^{+0.23}_{-0.28}$	$0.07^{+0.25}_{-0.28}$	$0.49^{+0.40}_{-0.37}$	$4.2^{+2.2}_{-2.0}$
	IMRPhenomXPNR (Bilby)	$24.5^{+5.0}_{-3.9}$	$0.60^{+0.34}_{-0.24}$	$0.03^{+0.22}_{-0.27}$	$0.63^{+0.29}_{-0.45}$	$3.4^{+2.3}_{-1.7}$
GW241011_233834	IMRPhenomXPHM_SpinTaylor (Bilby)	$9.09^{+0.08}_{-0.08}$	$0.31^{+0.07}_{-0.06}$	$0.50^{+0.06}_{-0.04}$	$0.38^{+0.13}_{-0.12}$	$0.21^{+0.04}_{-0.04}$
	NRSur7dq4 (Bilby)	$9.09^{+0.08}_{-0.08}$	$0.31^{+0.07}_{-0.06}$	$0.50^{+0.06}_{-0.04}$	$0.38^{+0.13}_{-0.12}$	$0.21^{+0.04}_{-0.04}$
	SEOBNRv5PHM (Bilby)	$9.05^{+0.07}_{-0.07}$	$0.27^{+0.13}_{-0.06}$	$0.50^{+0.05}_{-0.07}$	$0.45^{+0.23}_{-0.14}$	$0.22^{+0.04}_{-0.04}$
	IMRPhenomXPNR (Bilby)	$9.08^{+0.09}_{-0.08}$	$0.32^{+0.09}_{-0.05}$	$0.47^{+0.06}_{-0.03}$	$0.39^{+0.19}_{-0.13}$	$0.20^{+0.04}_{-0.04}$
GW241116_151753	IMRPhenomXPHM_SpinTaylor (Bilby)	$34.0^{+18.8}_{-9.6}$	$0.37^{+0.55}_{-0.27}$	$0.28^{+0.34}_{-0.48}$	$0.53^{+0.35}_{-0.40}$	$5.7^{+5.6}_{-2.9}$
	NRSur7dq4 (Bilby)	$34.0^{+18.8}_{-9.6}$	$0.37^{+0.55}_{-0.27}$	$0.28^{+0.34}_{-0.48}$	$0.53^{+0.35}_{-0.40}$	$5.7^{+5.6}_{-2.9}$
	SEOBNRv5PHM (RIFT)	$32.7^{+14.8}_{-8.2}$	$0.55^{+0.39}_{-0.38}$	$0.27^{+0.28}_{-0.38}$	$0.48^{+0.38}_{-0.36}$	$5.5^{+5.2}_{-2.7}$
	IMRPhenomXPNR (Bilby)	$33.7^{+13.7}_{-9.0}$	$0.54^{+0.40}_{-0.35}$	$0.30^{+0.34}_{-0.47}$	$0.48^{+0.38}_{-0.34}$	$7.2^{+6.0}_{-3.9}$
GW241127_061008	IMRPhenomXPHM_SpinTaylor (Bilby)	$30.8^{+3.6}_{-2.0}$	$0.33^{+0.15}_{-0.08}$	$-0.16^{+0.13}_{-0.14}$	$0.57^{+0.14}_{-0.21}$	$1.08^{+0.22}_{-0.18}$
	NRSur7dq4 (Bilby)	$33.3^{+3.1}_{-3.0}$	$0.44^{+0.17}_{-0.09}$	$-0.13^{+0.14}_{-0.16}$	$0.56^{+0.26}_{-0.26}$	$1.18^{+0.23}_{-0.20}$
	SEOBNRv5PHM (Bilby)	$33.5^{+4.1}_{-3.1}$	$0.45^{+0.25}_{-0.11}$	$-0.13^{+0.17}_{-0.18}$	$0.58^{+0.30}_{-0.24}$	$1.17^{+0.28}_{-0.29}$
	IMRPhenomXPNR (Bilby)	$32.3^{+2.9}_{-3.0}$	$0.41^{+0.15}_{-0.09}$	$-0.22^{+0.14}_{-0.17}$	$0.48^{+0.35}_{-0.22}$	$1.11^{+0.23}_{-0.20}$
GW241225_082815	IMRPhenomXPHM_SpinTaylor (Bilby)	$41.8^{+6.1}_{-5.2}$	$0.76^{+0.20}_{-0.22}$	$-0.17^{+0.21}_{-0.22}$	$0.70^{+0.25}_{-0.42}$	$1.88^{+1.08}_{-0.88}$
	NRSur7dq4 (Bilby)	$39.3^{+6.3}_{-5.6}$	$0.62^{+0.26}_{-0.24}$	$-0.23^{+0.21}_{-0.21}$	$0.74^{+0.19}_{-0.31}$	$1.97^{+1.17}_{-0.95}$
	SEOBNRv5PHM (RIFT)	$40.6^{+4.9}_{-4.1}$	$0.72^{+0.23}_{-0.17}$	$-0.19^{+0.20}_{-0.20}$	$0.65^{+0.26}_{-0.36}$	$1.80^{+1.01}_{-0.79}$
	IMRPhenomXPNR (Bilby)	$40.3^{+6.2}_{-7.5}$	$0.72^{+0.23}_{-0.37}$	$-0.15^{+0.20}_{-0.27}$	$0.72^{+0.22}_{-0.38}$	$1.92^{+1.28}_{-0.99}$
GW250114_082203	IMRPhenomXPHM_SpinTaylor (Bilby)	$28.71^{+0.50}_{-0.51}$	$0.96^{+0.04}_{-0.07}$	$-0.03^{+0.04}_{-0.05}$	$0.14^{+0.27}_{-0.11}$	$0.40^{+0.08}_{-0.07}$
	NRSur7dq4 (Bilby)	$28.70^{+0.43}_{-0.48}$	$0.96^{+0.04}_{-0.07}$	$-0.02^{+0.02}_{-0.04}$	$0.10^{+0.18}_{-0.07}$	$0.41^{+0.08}_{-0.07}$
	SEOBNRv5PHM (Bilby)	$28.63^{+0.50}_{-0.51}$	$0.96^{+0.04}_{-0.08}$	$-0.04^{+0.04}_{-0.05}$	$0.12^{+0.18}_{-0.09}$	$0.39^{+0.08}_{-0.07}$
	IMRPhenomXPNR (Bilby)	$28.49^{+0.60}_{-0.59}$	$0.96^{+0.04}_{-0.08}$	$-0.07^{+0.05}_{-0.05}$	$0.17^{+0.21}_{-0.12}$	$0.39^{+0.08}_{-0.08}$

NOTE—Values are given for a subset of the GW event candidates from O4b with FAR $< 1\,\mathrm{yr}^{-1}$ which show significant waveform systematics. The columns show chirp mass $\mathcal{M}$, mass ratio q, effective inspiral spin $\chi_{\rm eff}$, effective precession spin $\chi_{\rm p}$, and luminosity distance $D_{\rm L}$. Results are shown for different waveform models in each row, where the parenthesis indicates the used sampler.

One possible source of systematic uncertainty in our inferences is signal content that may be absent from our default CBC models. A method for testing for any missing signal content, or even to discover unexpected phenomena, is to estimate the overlap between the modeled reconstructions of our GW signals and the minimally modeled waveform reconstructions (Abac et al. 2026b). We test for missing signal content by selecting a subset of our O4b GW candidates and comparing their signal waveforms generated with the IMRPhenomXPHM_SpinTaylor waveform (Pratten et al. 2021; Colleoni et al. 2025) using the inferred source parameters to reconstructions made with minimal assumptions about the waveform morphology. We select 43 candidates using criteria to optimize performance of the minimally modeled reconstruction methods (Abac et al. 2026b).

To assess the statistical significance of the overlap between these reconstructions, we perform systematic injection studies (Abbott et al. 2019a; Salemi et al. 2019; Ghonge et al. 2020; Abbott et al. 2021b; Johnson-McDaniel et al. 2022). We inject simulated signals with parameters drawn

from the posterior distributions obtained with the IMRPHENOMXPHM_SPINTAYLOR waveform model (LIGO–Virgo–KAGRA Collaboration 2026a,b) into nearby detector data not overlapping the candidate time. These off-source waveforms are then reconstructed using minimally modeled methods. By comparing the overlaps between the on-source reconstruction of the actual candidate and the distribution of off-source overlaps, we compute a p-value indicating the fraction of off-source overlaps smaller than or equal to the on-source overlap.

We use three methods for reconstructing the signals with minimal assumptions about their morphology: BAYESWAVE (Cornish & Littenberg 2015; Littenberg & Cornish 2015; Cornish et al. 2021; Gupta & Cornish 2024) and CWB-2G (Klimenko et al. 2016; Drago et al. 2021), which are designed for generic GW transients, and CWB-BBH (Klimenko 2022), which is optimized specifically for CBC signals. The results, summarized in Table 5 and shown in Figure 8, show no statistically significant deviations between the on-source and off-source reconstructions across all three methods. However, as noted in Abac et al. (2026b), all three pipelines still show some level of biases in their respective tests to assess the p-values.

Table 5. Results of the minimally-modeled waveform consistency tests.

Candidate	BAYESWAVE					CWB-2G					CWB-BBH				
	On-source	Off-source	p-value	SNR	IFOs	On-source	Off-source	p-value	SNR	IFOs	On-source	Off-source	p-value	SNR	IFOs
GW240414_054515	0.73	$0.71^{+0.17}_{-0.68}$	0.53	9.90	HV	0.86	$0.78^{+0.08}_{-0.17}$	0.92	9.93	HV	0.86	$0.81^{+0.07}_{-0.17}$	0.85	10.85	HV
GW240501_033534	–	–	–	–	–	0.84	$0.85^{+0.06}_{-0.11}$	0.44	9.08	HL	0.92	$0.85^{+0.06}_{-0.12}$	0.95	10.39	HL
GW240511_031507	0.94	$0.88^{+0.06}_{-0.10}$	0.92	15.10	HLV	0.79	$0.84^{+0.06}_{-0.09}$	0.19	17.16	HLV	0.93	$0.91^{+0.03}_{-0.06}$	0.83	16.45	HL
GW240513_183302	–	–	–	–	–	0.79	$0.78^{+0.08}_{-0.16}$	0.56	13.24	HLV	0.87	$0.83^{+0.06}_{-0.12}$	0.83	13.79	HL
GW240514_121713	0.96	$0.92^{+0.04}_{-0.10}$	0.96	15.49	HLV	0.93	$0.91^{+0.03}_{-0.07}$	0.79	17.14	HLV	0.94	$0.93^{+0.03}_{-0.05}$	0.70	17.03	HL
GW240515_005301	0.73	$0.67^{+0.19}_{-0.51}$	0.62	7.49	HL	0.75	$0.74^{+0.11}_{-0.18}$	0.55	11.00	HLV	0.74	$0.82^{+0.07}_{-0.16}$	0.18	12.74	HL
GW240519_012815	0.82	$0.81^{+0.11}_{-0.31}$	0.52	9.88	LV	0.83	$0.80^{+0.08}_{-0.15}$	0.65	11.52	LV	0.88	$0.84^{+0.07}_{-0.12}$	0.78	13.01	LV
GW240615_113620	0.97	$0.96^{+0.02}_{-0.03}$	0.78	23.45	HLV	0.94	$0.93^{+0.02}_{-0.03}$	0.83	26.88	HLV	0.97	$0.95^{+0.02}_{-0.02}$	0.98	26.38	HL
GW240615_160735	–	–	–	–	–	0.79	$0.73^{+0.10}_{-0.19}$	0.80	10.31	HLV	0.70	$0.80^{+0.08}_{-0.19}$	0.16	13.08	HL
GW240621_195059	0.96	$0.96^{+0.02}_{-0.05}$	0.46	27.63	HLV	0.95	$0.95^{+0.01}_{-0.03}$	0.46	28.75	HLV	0.93	$0.96^{+0.01}_{-0.02}$	0.03	29.04	HL
GW240621_200935	–	–	–	–	–	0.78	$0.78^{+0.09}_{-0.17}$	0.50	9.22	HLV	0.93	$0.84^{+0.07}_{-0.14}$	0.99	10.78	HL
GW240630_101703	0.76	$0.66^{+0.21}_{-0.62}$	0.69	8.75	HLV	0.75	$0.76^{+0.10}_{-0.18}$	0.49	9.68	HLV	0.84	$0.82^{+0.07}_{-0.16}$	0.67	10.62	HL
GW240703_191355	0.81	$0.67^{+0.19}_{-0.42}$	0.84	7.01	LV	0.86	$0.74^{+0.10}_{-0.20}$	0.97	9.54	LV	0.86	$0.82^{+0.08}_{-0.13}$	0.80	11.50	LV
GW240705_053215	0.94	$0.90^{+0.05}_{-0.10}$	0.85	14.33	HLV	0.93	$0.90^{+0.04}_{-0.06}$	0.79	15.49	HLV	0.90	$0.93^{+0.03}_{-0.06}$	0.17	16.82	HL
GW240716_034900	0.87	$0.82^{+0.09}_{-0.25}$	0.73	11.33	LV	0.86	$0.79^{+0.08}_{-0.13}$	0.92	13.43	LV	–	–	–	–	–
GW240902_143306	–	–	–	–	–	0.74	$0.74^{+0.11}_{-0.17}$	0.51	8.12	HL	0.68	$0.77^{+0.10}_{-0.19}$	0.19	9.56	HL
GW240908_082628	0.81	$0.73^{+0.15}_{-0.55}$	0.69	6.78	HLV	0.89	$0.79^{+0.08}_{-0.18}$	0.98	9.87	HLV	0.92	$0.83^{+0.07}_{-0.14}$	0.98	9.82	HL
GW240919_061559	0.92	$0.90^{+0.05}_{-0.12}$	0.66	15.60	HLV	0.88	$0.88^{+0.04}_{-0.07}$	0.39	16.64	HLV	0.93	$0.91^{+0.03}_{-0.05}$	0.76	16.23	HL
GW240920_124024	0.99	$0.98^{+0.01}_{-0.02}$	0.94	37.58	HL	0.96	$0.97^{+0.01}_{-0.01}$	0.17	37.74	HL	0.97	$0.98^{+0.01}_{-0.01}$	0.06	38.90	HL
GW240923_204006	0.94	$0.85^{+0.07}_{-0.23}$	0.98	10.92	HLV	0.93	$0.85^{+0.07}_{-0.11}$	0.97	12.21	HLV	0.87	$0.90^{+0.04}_{-0.09}$	0.26	14.14	HL
GW240924_000316	–	–	–	–	–	0.83	$0.82^{+0.08}_{-0.18}$	0.63	10.69	HLV	0.85	$0.85^{+0.06}_{-0.12}$	0.49	11.34	HL
GW240930_234614	–	–	–	–	–	0.72	$0.78^{+0.09}_{-0.17}$	0.22	11.01	HL	0.86	$0.81^{+0.09}_{-0.19}$	0.81	11.41	HL
GW241002_030559	0.80	$0.80^{+0.11}_{-0.26}$	0.53	9.24	LV	0.86	$0.79^{+0.09}_{-0.19}$	0.90	11.28	LV	0.91	$0.85^{+0.06}_{-0.13}$	0.94	11.93	LV
GW241006_015333	–	–	–	–	–	0.85	$0.86^{+0.05}_{-0.08}$	0.42	18.00	HLV	0.87	$0.89^{+0.04}_{-0.07}$	0.29	17.64	HL
GW241101_220523	0.76	$0.63^{+0.20}_{-0.58}$	0.78	8.95	LV	0.71	$0.73^{+0.11}_{-0.21}$	0.40	11.55	LV	0.81	$0.80^{+0.09}_{-0.15}$	0.58	11.06	LV
GW241102_144729	0.89	$0.85^{+0.07}_{-0.20}$	0.76	10.11	HLV	0.86	$0.86^{+0.06}_{-0.10}$	0.53	11.55	HLV	0.89	$0.89^{+0.04}_{-0.11}$	0.45	12.69	HL
GW241109_033317	0.75	$0.79^{+0.13}_{-0.34}$	0.43	10.69	LV	0.76	$0.78^{+0.09}_{-0.18}$	0.43	10.62	LV	0.84	$0.82^{+0.08}_{-0.13}$	0.65	12.84	LV
GW241111_111552	–	–	–	–	–	0.91	$0.88^{+0.04}_{-0.07}$	0.87	15.97	HL	0.91	$0.88^{+0.04}_{-0.08}$	0.88	17.00	HL
GW241114_024711	0.83	$0.79^{+0.12}_{-0.72}$	0.60	9.13	HLV	0.87	$0.82^{+0.07}_{-0.13}$	0.87	10.51	HLV	0.91	$0.86^{+0.06}_{-0.11}$	0.91	11.25	HL
GW241127_061008	0.98	$0.98^{+0.01}_{-0.02}$	0.70	31.47	HLV	0.96	$0.96^{+0.01}_{-0.02}$	0.70	30.33	HLV	0.96	$0.97^{+0.01}_{-0.02}$	0.24	31.50	HL
GW241129_021832	0.88	$0.88^{+0.06}_{-0.14}$	0.55	13.69	HLV	0.91	$0.87^{+0.05}_{-0.09}$	0.92	16.57	HLV	0.93	$0.90^{+0.04}_{-0.08}$	0.87	16.83	HL

Table 5 *continued*

Table 5 *(continued)*

Candidate	BAYESWAVE					CWB-2G					CWB-BBH				
	On-source	Off-source	p-value	SNR	IFOs	On-source	Off-source	p-value	SNR	IFOs	On-source	Off-source	p-value	SNR	IFOs
GW241130_034908	0.67	$0.78^{+0.10}_{-0.72}$	0.28	12.21	HLV	0.86	$0.81^{+0.08}_{-0.13}$	0.84	13.21	HLV	0.88	$0.86^{+0.06}_{-0.10}$	0.73	13.25	HL
GW241210_060606	0.88	$0.69^{+0.17}_{-0.69}$	0.98	9.82	HLV	0.83	$0.78^{+0.09}_{-0.16}$	0.82	12.17	HLV	0.89	$0.84^{+0.06}_{-0.14}$	0.89	13.39	HL
GW241225_082815	0.95	$0.94^{+0.03}_{-0.10}$	0.57	17.71	HL	0.94	$0.94^{+0.02}_{-0.04}$	0.55	19.73	HL	0.96	$0.95^{+0.02}_{-0.05}$	0.86	19.60	HL
GW241230_084504	0.94	$0.82^{+0.10}_{-0.25}$	0.98	9.85	LV	0.89	$0.81^{+0.08}_{-0.15}$	0.96	11.69	LV	–	–	–	–	–
GW241230_233618	0.92	$0.91^{+0.06}_{-0.40}$	0.60	11.15	HLV	0.84	$0.88^{+0.06}_{-0.13}$	0.25	11.45	HLV	0.90	$0.91^{+0.04}_{-0.09}$	0.38	12.33	HL
GW250104_015122	0.89	$0.84^{+0.08}_{-0.24}$	0.84	9.64	HLV	0.88	$0.84^{+0.07}_{-0.11}$	0.76	11.92	HLV	0.94	$0.89^{+0.05}_{-0.11}$	0.96	12.10	HL
GW250108_152221	0.92	$0.85^{+0.09}_{-0.71}$	0.81	9.53	HLV	0.89	$0.87^{+0.06}_{-0.11}$	0.67	11.18	HLV	0.91	$0.90^{+0.04}_{-0.10}$	0.59	11.78	HL
GW250109_010541	0.89	$0.84^{+0.09}_{-0.31}$	0.73	11.04	HLV	0.89	$0.83^{+0.07}_{-0.11}$	0.92	12.34	HLV	0.89	$0.88^{+0.05}_{-0.11}$	0.62	13.10	HL
GW250109_074552	0.85	$0.81^{+0.10}_{-0.66}$	0.71	8.19	HV	0.83	$0.81^{+0.07}_{-0.13}$	0.68	11.21	HV	–	–	–	–	–
GW250114_082203	0.99	$1.00^{+0.00}_{-0.00}$	0.47	79.09	HL	0.97	$0.97^{+0.01}_{-0.02}$	0.66	73.54	HL	0.98	$0.99^{+0.00}_{-0.01}$	0.09	78.70	HL
GW250118_170523	0.88	$0.87^{+0.06}_{-0.25}$	0.63	12.21	HL	0.87	$0.86^{+0.05}_{-0.08}$	0.66	13.46	HL	0.86	$0.87^{+0.05}_{-0.08}$	0.45	13.93	HL
GW250119_025138	0.91	$0.86^{+0.06}_{-0.19}$	0.85	12.64	HLV	0.90	$0.86^{+0.06}_{-0.10}$	0.87	13.84	HLV	0.94	$0.90^{+0.04}_{-0.07}$	0.96	14.38	HL

NOTE—The three minimally-modeled waveform reconstruction methods used were BAYESWAVE, CWB-2G (both designed for generic GW bursts), and CWB-BBH (specifically optimized for CBC signals with tailored frequency bands and time-frequency resolutions). The p-values are calculated by comparing the on-source value with the off-source distribution of overlaps.

Because of their differences, due at least in part to the different detector networks used in their processing, the tests carried out by the three pipelines can be considered to be independent studies. Both CWB-BBH and CWB-2G injected 2000 waveform samples drawn from the posterior distributions, while BAYESWAVE processed 200 samples, and this accounts for the different error bars in Figure 8. The interferometer networks used by CWB-BBH and CWB-2G sometimes differ: while CWB-2G uses three detectors whenever possible, the version of CWB-BBH used to produce the results in this catalog is limited to two detectors. Finally, the three pipelines use different versions of the posterior samples to construct the injections. Taken together, these studies show that while a few of the new candidates added to GWTC-5.0 show noticeable systematic uncertainties in our inferences of their source properties, there is as yet no strong evidence for missing signal content in our models. In particular, this also applies to GW240930_234614, which is discussed above as one of the events detected only by CWB-BBH and exhibiting the most significant differences in posteriors between analyses, with p-values 0.22 and 0.81 from CWB-2G and CWB-BBH, respectively.

4. CONCLUSION

We present GWTC-5.0 which contains 390 CBC events. The criteria for inclusion in the catalog are that events have $p_{\rm astro} \geq 0.5$ and have passed further event validation checks, making them unlikely to be of instrumental origin. Analyzing data from O4b, this version of the catalog adds 161 GW candidates consistent with BBHs to the cumulative catalog of events, further expanding the census of CBCs from the first three observing runs (Abbott et al. 2023a). For high-significance candidates with FAR $< 1\,{\rm yr}^{-1}$, we also estimate the source properties. Some particularly notable candidates are: GW250114_082203 (Abac et al. 2025b), the highest SNR observed to date; GW240615_113620, the best localized GW source observed to date; GW241011_233834 and GW241110_124123 (Abac et al. 2025c), which have well-measured, non-zero effective inspiral spins $\chi_{\rm eff}$; and GW240925_005809, whose high SNR enabled an informative astrophysical measurements of GW detector calibration (Abac et al. 2026a)

Additional results related to candidates in the catalog are interpreted in other papers of the GWTC-5.0 focus issue (Abac et al. 2026g). This includes inferring the mass and spin distributions of the CBCs we have observed (Abac et al. 2026d), testing general relativity in the strong-field regime (Abac et al. 2026f), providing independent measures of local cosmology (Abac et al. 2026e), and searching for gravitationally lensed counterparts to our candidates (Abac et al. 2026h).

The data products associated with the results described here, as well as a larger list of candidates satisfying the weaker selection criterion with a FAR $< 2\,{\rm d}^{-1}$ and the underlying strain data are publicly available through GWOSC and are described in detail in Abac et al. (2026c). Past releases of the public strain data have led to additional GW candidates (Nitz et al. 2019; Venumadhav et al. 2020, 2019; Zackay et al. 2021, 2019; Magee et al. 2019; Nitz et al. 2020b, 2021, 2023; Olsen et al. 2022; Kumar & Dent 2024; Mishra et al. 2025; Koloniari et al. 2025), and the data products have enabled numerous studies probing the nature of individual detections, population properties, and other astrophysical inferences.

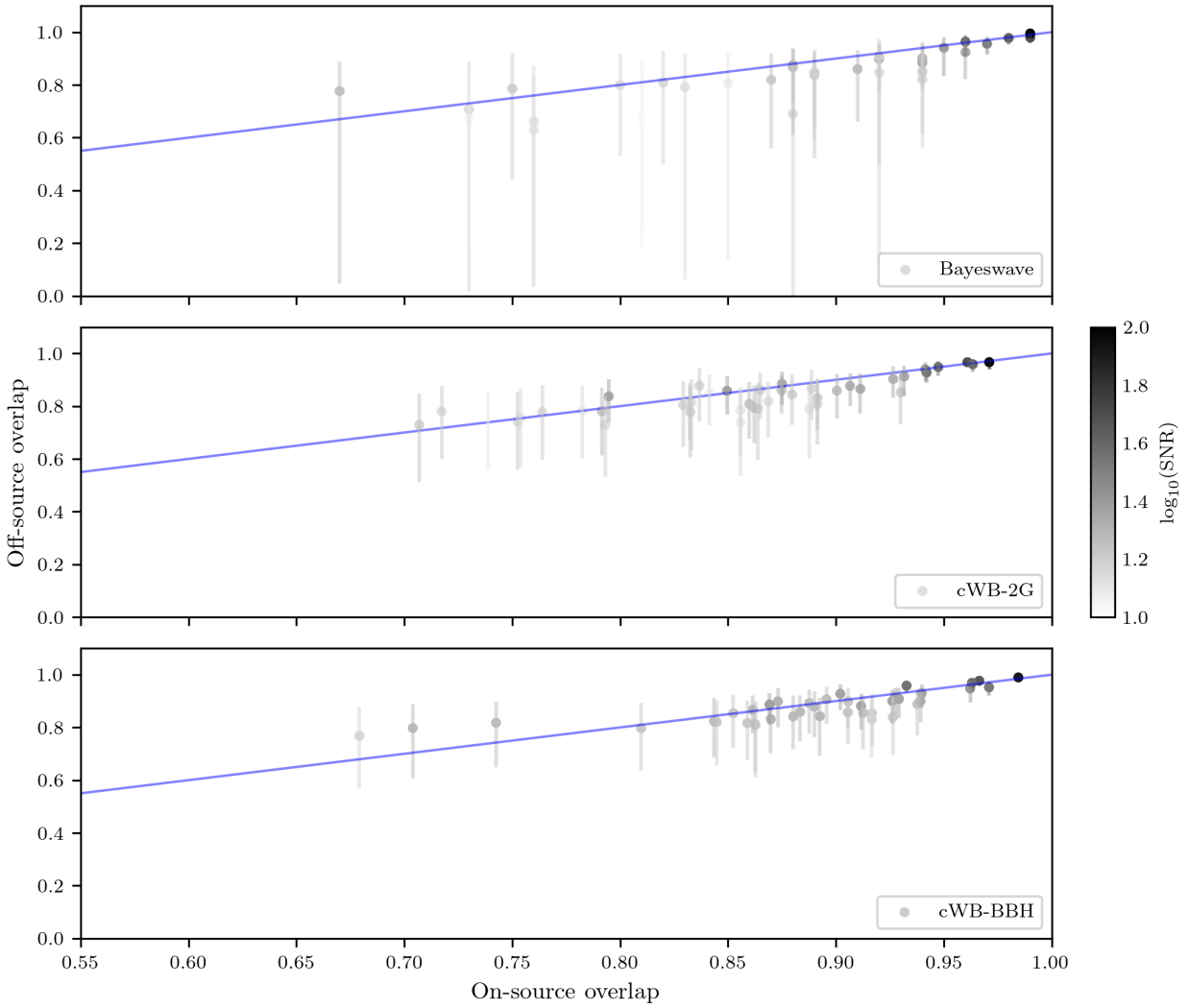

Figure 8. A comparison of the overlap between the on-source and off-source (with 90% confidence intervals) reconstructions for three different minimally modeled pipelines, BAYESWAVE, CWB-2G, and CWB-BBH where the IMRPHENOMXPHM_SPINTAYLOR waveform was used in parameter estimation, the network SNR was greater than 10, and the redshifted chirp mass $(1+z)\mathcal{M} > 15M_{\odot}$. The data points and their uncertainties are drawn with a gray level corresponding to the network SNR detected by each pipeline; the gray scale is non linear to fit the large dynamic range of SNR values. The blue line denotes equal overlap between the on- and off-source reconstructions, indicating that there is no significant difference between the two.

The data-taking period reported here ended on 2025 January 28. Data recorded subsequently fall into the third part of the fourth observing run (O4c), which is presently being analyzed. O4c included a commissioning break between 2025 April 1 and 2025 June 11, and eventually ended on 2025 November 18. The candidate list and associated parameter inference for O4c data will be published in GWTC-6.0.

Regarding the next data taking, LVK plan an interim observing run, designated intermediate run 1 whose details can be found and will be regularly updated in LIGO–Virgo–KAGRA Collaboration (2026c). Both LIGO detectors are expected to be observing, and Virgo and KAGRA will join as they are available. Furthermore, in the coming years, the LVK network will undergo additional upgrades to further improve its sensitivity (Abbott et al. 2020) in order to enable the improved uncertainties of binary population (Abac et al. 2026d) and cosmological (Abac et al. 2026e) properties, and more stringent constraints on tests of general relativity (Abac et al. 2026f) and searches for gravitational lensing (Abac et al. 2026h), as well as the long-awaited next multimessenger observations since GW170817 (Abbott et al. 2017a). Future GW transients could include not only novel CBC sources, such as subsolar-mass compact binaries (Abbott et al. 2018, 2019e, 2022a, 2023c; Nitz & Wang 2021a,b) or other exotica, but also new classes of GW transients such as supernovae (Abbott et al. 2021d), cosmic strings (Abbott et al. 2021e), and bursts of unknown origin (Abac et al. 2025d,d; Abbott et al. 2021c). We additionally anticipate

detections of gravitationally lensed GW signals (Abac et al. 2025) as well as long-lived GW signals from rapidly rotating NSs (Abac et al. 2025d; Abbott et al. 2022b) and the stochastic background (Abbott et al. 2021f,g) of the Universe. As the detectors improve in sensitivity, we therefore expect to continue to deepen our understanding of the Universe.

DATA AVAILABILITY

All strain data analysed as part of GWTC-5.0 are publicly availably through GWOSC. The details of this data release and information about the digital version of the GWTC are described in detail in Abac et al. (2026c). We also provide data releases of the search pipeline results and initial source localization; see LIGO–Virgo–KAGRA Collaboration (2026d) for GWTC-5.0 and LIGO–Virgo–KAGRA Collaboration (2026e) for GWTC-4.1, as well as parameter-estimation samples; see LIGO–Virgo–KAGRA Collaboration (2026a,b) for GWTC-5.0 and LIGO–Virgo–KAGRA Collaboration (2026f) for GWTC-4.1. Additionally, data for the glitch modelling (LIGO–Virgo–KAGRA Collaboration 2026g), and data-quality products (LIGO–Virgo–KAGRA Collaboration 2026h) are included as part of this release. Finally, the search sensitivity estimates are also publicly available (LIGO–Virgo–KAGRA Collaboration 2026i,j).

ACKNOWLEDGEMENTS

This material is based upon work supported by NSF's LIGO Laboratory, which is a major facility fully funded by the National Science Foundation. The authors also gratefully acknowledge the support of the Science and Technology Facilities Council (STFC) of the United Kingdom, the Max-Planck-Society (MPS), and the State of Niedersachsen/Germany for support of the construction of Advanced LIGO and construction and operation of the GEO 600 detector. Additional support for Advanced LIGO was provided by the Australian Research Council. The authors gratefully acknowledge the Italian Istituto Nazionale di Fisica Nucleare (INFN), the French Centre National de la Recherche Scientifique (CNRS) and the Netherlands Organization for Scientific Research (NWO) for the construction and operation of the Virgo detector and the creation and support of the EGO consortium. The authors also gratefully acknowledge research support from these agencies as well as by the Council of Scientific and Industrial Research of India, the Department of Science and Technology, India, the Science & Engineering Research Board (SERB), India, the Ministry of Human Resource Development, India, the Spanish Agencia Estatal de Investigación (AEI), the Spanish Ministerio de Ciencia, Innovación y Universidades, the European Union NextGenerationEU/PRTR (PRTR-C17.I1), the ICSC - CentroNazionale di Ricerca in High Performance Computing, Big Data and Quantum Computing, funded by the European Union NextGenerationEU, the Comunitat Autonòma de les Illes Balears through the Conselleria d'Educació i Universitats, the Conselleria d'Innovació, Universitats, Ciència i Societat Digital de la Generalitat Valenciana and the CERCA Programme Generalitat de Catalunya, Spain, the Polish National Agency for Academic Exchange, the National Science Centre of Poland and the European Union - European Regional Development Fund; the Foundation for Polish Science (FNP), the Polish Ministry of Science and Higher Education, the Swiss National Science Foundation (SNSF), the Russian Science Foundation, the European Commission, the European Social Funds (ESF), the European Regional Development Funds (ERDF), the Royal Society, the Scottish Funding Council, the Scottish Universities Physics Alliance, the Hungarian Scientific Research Fund (OTKA), the French Lyon Institute of Origins (LIO), the Belgian Fonds de la Recherche Scientifique (FRS-FNRS), Actions de Recherche Concertées (ARC) and Fonds Wetenschappelijk Onderzoek - Vlaanderen (FWO), Belgium, the Paris Île-de-France Region, the National Research, Development and Innovation Office of Hungary (NKFIH), the National Research Foundation of Korea, the Natural Sciences and Engineering Research Council of Canada (NSERC), the Canadian Foundation for Innovation (CFI), the Brazilian Ministry of Science, Technology, and Innovations, the International Center for Theoretical Physics South American Institute for Fundamental Research (ICTP-SAIFR), the Research Grants Council of Hong Kong, the National Natural Science Foundation of China (NSFC), the Israel Science Foundation (ISF), the US-Israel Binational Science Fund (BSF), the Leverhulme Trust, the Research Corporation, the National Science and Technology Council (NSTC), Taiwan, the United States Department of Energy, and the Kavli Foundation. The authors gratefully acknowledge the support of the NSF, STFC, INFN and CNRS for provision of computational resources.

This work was supported by MEXT, the JSPS Leading-edge Research Infrastructure Program, JSPS Grant-in-Aid for Specially Promoted Research 26000005, JSPS Grant-in-Aid for Scientific Research on Innovative Areas 2402: 24103006, 24103005, and 2905: JP17H06358, JP17H06361 and JP17H06364, JSPS Core-to-Core Program A. Advanced Research Networks, JSPS Grants-in-Aid for Scientific Research (S) 17H06133 and 20H05639, JSPS Grant-in-Aid for Transformative Research Areas (A) 20A203: JP20H05854, the joint research program of the Institute for Cosmic Ray Research, University of Tokyo, the National Research Foundation (NRF), the Computing Infrastructure Project of the Global Science experimental Data hub Center (GSDC) at KISTI, the Korea Astronomy and Space Science Institute (KASI), the Ministry of Science and ICT (MSIT) in Korea, Academia Sinica (AS), the AS Grid Center (ASGC) and the National Science and Technology Council (NSTC) in Taiwan under grants including the Science Vanguard Research Program, the Advanced Technology Center (ATC) of NAOJ, the Mechanical Engineering Center of KEK and Vietnam National Foundation for Science and Technology Development (NAFOSTED) 103.01-2025.147.

Additional acknowledgements for support of individual authors may be found in the following document: `https://dcc.ligo.org/LIGO-M2300033/public`.

thor Accepted Manuscript version arising. We request that citations to this article use 'A. G. Abac *et al.* (LIGO-Virgo-KAGRA Collaboration), ...' or similar phrasing, depending on journal convention.

Software: Calibration of the LIGO strain data was performed with a GSTLAL-based calibration software pipeline (Viets et al. 2018). Data-quality products and event-validation results were computed using the BRISTOL (Di Renzo et al. 2024), DMT (Zweizig 2006), DQRBUILD (Davis et al. 2026), DQSEGDB (Fisher et al. 2021), GLITCHFIND (Vazsonyi & Davis 2023), GSPYNETTREE (Álvarez-López et al. 2024), GWDETCHAR (Urban et al. 2021), HVETO (Smith et al. 2011), IDQ (Essick et al. 2020), LIGODV-WEB (Areeda et al. 2017), OMEGAOVERLAP (Areeda et al. 2017) OMICRON (Robinet et al. 2020), PEMCHECK (Helmling-Cornell et al. 2024), PYTHONVIRGOTOOLS (Virgo Collaboration 2021) STATIONARITY (Mozzon et al. 2020), and VIRGO DQR (Acernese et al. 2023) software packages and contributing software tools. Analyses in this catalog relied upon the LALSUITE software library (LIGO–Virgo–KAGRA Collaboration 2018; Wette 2020). The detection of the signals and subsequent significance evaluations in this catalog were performed with the GSTLAL-based inspiral software pipeline (Messick et al. 2017; Sachdev et al. 2019; Hanna et al. 2020; Cannon et al. 2021), with the MBTA pipeline (Adams et al. 2016; Aubin et al. 2021), and with the PYCBC (Usman et al. 2016; Nitz et al. 2017; Davies et al. 2020) and the CWB (Klimenko & Mitselmakher 2004; Klimenko et al. 2011, 2016) packages. Estimates of the noise spectra and glitch models were obtained using BAYESWAVE (Cornish & Littenberg 2015; Littenberg et al. 2016; Cornish et al. 2021; Gupta & Cornish 2024). Source-parameter estimation was performed with the BILBY library (Ashton et al. 2019; Romero-Shaw et al. 2020) using the DYNESTY nested sampling package (Speagle 2020). PESUMMARY was used to postprocess and collate parameter-estimation results (Hoy & Raymond 2021). The various stages of the parameter-estimation analysis were managed with the ASIMOV library (Williams et al. 2023). Plots were prepared with MATPLOTLIB (Hunter 2007), SEABORN (Waskom 2021) and GWPY (Macleod et al. 2021). NUMPY (Harris et al. 2020) and SCIPY (Virtanen et al. 2020) were used in the preparation of the manuscript.

APPENDIX

A. UPDATE ON O4A CANDIDATES

In this section we update some of the results for those identified in O4a after the reanalysis by the two search pipelines, PYCBC and GSTLAL, with updated configurations (Abac et al. 2026b). Specifically, this includes the updated information for the O4a candidates with a FAR $< 1\,\mathrm{yr}^{-1}$ and $p_{\mathrm{astro}} \geq 0.5$ as well as the source properties of additional two candidates in the following. To clarify that these O4a results supersede those in GWTC-4.0, we name them GWTC-4.1. However, as GWTC-5.0 is a cumulative catalog, all the results labeled GWTC-4.1 are included in GWTC-5.0 by definition. The candidates with a FAR $< 2\,\mathrm{d}^{-1}$ that do not meet these criteria are also included in the data release (LIGO–Virgo–KAGRA Collaboration 2026e).

For PYCBC, the updated O4a reanalysis incorporates corrections to the ranking statistics: single-detector triggers are downweighted by a constant correction to improve the overall search sensitivity, as described in Section 3.4 of Abac et al. (2026b). With the new statistics, 77 events are identified with a FAR $< 1\,\mathrm{yr}^{-1}$ as compared to 71 in the previous GWTC-4.0 catalog. Two of these events are not identified with a FAR $< 1\,\mathrm{yr}^{-1}$ by any other pipeline: GW231026_130704 and GW231113_150041.

For GSTLAL, the updated O4a reanalysis includes a set of methodological corrections that affect both ranking statistics and the computation of p_{astro} (Abac et al. 2026b). First, we revised the handling of horizon-distance information, which encodes the time-dependent detector sensitivity in the ranking statistic. Second, GW events detected online are excluded from the background estimation during re-ranking. Finally, the normalization used to map ranking information to p_{astro} was corrected. As a result, the odds, $p_{\mathrm{astro}}/(1 - p_{\mathrm{astro}})$, are increased by a factor of ~ 3.6 in O4a. The net effect of these changes is to increase p_{astro}, which in our previous publication had been systematically underestimated. All of these corrections have also been applied to the O4b results presented in this paper.

The significant candidates resulting from these reanalyses, together with the candidates produced by MBTA and CWB (which are unchanged from GWTC-4.0), are summarized in Table 6, containing all candidates detected with $p_{\mathrm{astro}} \geq 0.5$ and FAR $< 1\,\mathrm{yr}^{-1}$ in at least one of the four pipelines during O4a and the pre-O4a engineering run. Consequently, we identify 1456 candidates with a FAR $< 2\,\mathrm{d}^{-1}$ in at least one pipeline, and 139 candidates with $p_{\mathrm{astro}} \geq 0.5$ in at least one pipeline and not vetoed during event validation (Abac et al. 2026b). These updated candidate lists also imply changes in the purity of the set of subthreshold candidates with $p_{\mathrm{astro}} < 0.5$. We recompute this for the updated O4a candidates, using the refined formalism described in Abbott et al. (2023a); Abac et al. (2026b), and find that the purity of the subthreshold candidate set is now 0.022, as compared to the estimate of 0.013 obtained from a simplified method for the previous release of O4a candidates.

A detailed analysis of source properties was carried out for the two new candidates identified by PyCBC with a FAR $< 1\,\mathrm{yr}^{-1}$, whose results are summarized in Table 7 and Figure 9. Similar to Figure 2, the lower region of each posterior distribution in Figure 9 shows the population-informed measurements based on the BBH population inferred in Abac et al. (2026d). This analysis was run using four waveform models. Unless otherwise noted, BILBY was used to perform inference. The two mod-

els IMRPHENOMXPHM_SPINTAYLOR and NRSUR7DQ4 were operated precisely as in GWTC-4.0 (Abac et al. 2025). The NRSUR7DQ4 model is used where the posteriors of the source are within the model validity parameter range, in this case only for GW231026_130704. The SEOBNRv5PHM model has been updated to also include asymmetries between negative and positive multipoles (Abac et al. 2026b; Estellés et al. 2026), and was run with the RIFT sampler. Finally, the waveform model IMRPHENOMXPNR replaces IMRPHENOMXO4A. Similar to the O4b results presented in Section 3, the posteriors derived from the IMRPHENOMXPHM_SPINTAYLOR are shown in Table 7 and Figure 9. We find that the inferred component masses of these two candidates are consistent with BBHs sources. All of the posterior samples from O4a, including the two new events above, are available in the data release (LIGO–Virgo–KAGRA Collaboration 2026f).

Table 6. Candidate GW signals from the O4a reanalysis with a FAR $< 1\,\mathrm{yr}^{-1}$ in at least one pipeline and for which $p_{\mathrm{astro}} \geq 0.5$.

Candidate	Inst.	cWB-BBH			**GstLAL**			MBTA			**PyCBC**		
		FAR (yr^{-1})	SNR	p_{astro}	FAR (yr^{-1})	SNR	p_{astro}	FAR (yr^{-1})	SNR	p_{astro}	FAR (yr^{-1})	SNR	p_{astro}
GW230518_125908	HL	–	–	–	$\mathbf{< 1.0 \times 10^{-5}}$	**13.7**	**> 0.99**	$< 1.0 \times 10^{-5}$	14.1	> 0.99	$\mathbf{7.1 \times 10^{-4}}$	**13.6**	**> 0.99**
GW230529_181500	L	–	–	–	**0.0056**	**11.8**	**0.93**	2.2×10^{-4}	11.4	> 0.99	$\mathbf{1.0 \times 10^{-3}}$	**11.7**	**> 0.99**
GW230601_224134	HL	0.0013	13.4	> 0.99	$\mathbf{< 1.0 \times 10^{-5}}$	**11.8**	**> 0.99**	0.0082	12.4	> 0.99	$\mathbf{2.8 \times 10^{-4}}$	**12.2**	**> 0.99**
GW230605_065343	HL	*560*	*7.5*	*< 0.01*	$\mathbf{2.3 \times 10^{-5}}$	**10.7**	**> 0.99**	$< 1.0 \times 10^{-5}$	11.1	> 0.99	$\mathbf{1.3 \times 10^{-5}}$	**11.4**	**> 0.99**
GW230606_004305	HL	0.0067	11.1	> 0.99	**0.0013**	**10.9**	**> 0.99**	*1.9*	*10.9*	*0.83*	$\mathbf{4.1 \times 10^{-4}}$	**10.7**	**> 0.99**
GW230608_205047	HL	0.032	9.9	> 0.99	**0.0011**	**10.2**	**> 0.99**	0.27	10.2	0.96	–	–	–
GW230609_064958	HL	0.0013	10.6	> 0.99	$\mathbf{1.3 \times 10^{-4}}$	**10.0**	**> 0.99**	*3.6*	*10.5*	*0.73*	$\mathbf{1.0 \times 10^{-4}}$	**9.6**	**> 0.99**
GW230624_113103	HL	0.0022	11.4	> 0.99	$\mathbf{1.7 \times 10^{-4}}$	**10.0**	**> 0.99**	0.018	10.3	> 0.99	**0.0011**	**10.2**	**> 0.99**
GW230627_015337	HL	0.0011	27.8	> 0.99	$\mathbf{< 1.0 \times 10^{-5}}$	**28.3**	**> 0.99**	$< 1.0 \times 10^{-5}$	28.4	> 0.99	$\mathbf{< 1.0 \times 10^{-5}}$	**28.7**	**> 0.99**
GW230628_231200	HL	0.0011	16.4	> 0.99	$\mathbf{< 1.0 \times 10^{-5}}$	**15.3**	**> 0.99**	$< 1.0 \times 10^{-5}$	15.9	> 0.99	$\mathbf{< 1.0 \times 10^{-5}}$	**15.9**	**> 0.99**
GW230630_070659*	HL	–	–	–	**0.47**	**9.8**	**0.96**	–	–	–	–	–	–
GW230630_125806	HL	0.16	9.0	0.97	**0.24**	**8.1**	**0.98**	*1.3*	*8.2*	*0.87*	**0.048**	**8.1**	**> 0.99**
GW230630_234532	HL	–	–	–	**0.029**	**9.8**	**> 0.99**	4.2×10^{-4}	9.9	> 0.99	**0.023**	**9.8**	**> 0.99**
GW230702_185453	HL	0.0089	10.1	> 0.99	$\mathbf{< 1.0 \times 10^{-5}}$	**9.8**	**> 0.99**	0.21	9.9	0.97	**0.0020**	**9.2**	**> 0.99**
GW230704_021211	HL	–	–	–	**0.20**	**9.4**	**0.98**	*2.7*	*9.2*	*0.78*	**0.037**	**9.2**	**> 0.99**
GW230704_212616	HL	*43*	*8.3*	*0.14*	***10***	***8.3***	***0.57***	0.51	8.7	0.93	–	–	–
GW230706_104333	HL	–	–	–	**0.22**	**9.2**	**0.98**	–	–	–	**0.25**	**8.8**	**0.99**
GW230707_124047	HL	0.0011	11.9	> 0.99	**0.0026**	**10.1**	**> 0.99**	0.072	10.3	0.99	$\mathbf{4.2 \times 10^{-4}}$	**10.5**	**> 0.99**
GW230708_053705	HL	–	–	–	***2.4***	***8.6***	***0.84***	*54*	*8.9*	*0.15*	**0.028**	**8.9**	**> 0.99**
GW230708_230935	HL	*1.2*	*10.0*	*0.80*	**0.0036**	**9.6**	**> 0.99**	0.26	9.7	0.96	**0.0010**	**9.4**	**> 0.99**
GW230709_122727	HL	0.071	10.2	> 0.99	**0.16**	**9.9**	**0.98**	*12*	*10.1*	*0.48*	$\mathbf{9.7 \times 10^{-4}}$	**10.0**	**> 0.99**
GW230712_090405	HL	0.018	9.5	> 0.99	***98***	***8.2***	***0.14***	–	–	–	***67***	***8.2***	***0.17***
GW230723_101834	HL	–	–	–	**0.0052**	**9.9**	**> 0.99**	0.0034	10.0	> 0.99	$\mathbf{2.2 \times 10^{-4}}$	**10.1**	**> 0.99**
GW230726_002940	L	–	–	–	$\mathbf{< 1.0 \times 10^{-5}}$	**10.5**	**> 0.99**	–	–	–	***4.5***	***10.0***	***0.68***
GW230729_082317	HL	–	–	–	**0.17**	**9.5**	**0.98**	–	–	–	***4.7***	***9.4***	***0.78***
GW230731_215307	HL	–	–	–	$\mathbf{< 1.0 \times 10^{-5}}$	**12.2**	**> 0.99**	$< 1.0 \times 10^{-5}$	11.9	> 0.99	$\mathbf{< 1.0 \times 10^{-5}}$	**11.9**	**> 0.99**
GW230803_033412	HL	*3.0*	*9.4*	*0.68*	***2.9***	***8.0***	***0.81***	*19*	*8.6*	*0.35*	**0.044**	**8.2**	**> 0.99**

Table 6 *continued*

Table 6 *(continued)*

Candidate	Inst.	cWB-BBH			**GstLAL**			MBTA			**PyCBC**		
		FAR (yr^{-1})	SNR	p_{astro}	FAR (yr^{-1})	SNR	p_{astro}	FAR (yr^{-1})	SNR	p_{astro}	FAR (yr^{-1})	SNR	p_{astro}
GW230805_034249	HL	*7.5*	*9.5*	*0.49*	**0.0063**	**9.3**	**> 0.99**	*6.4*	*9.4*	*0.62*	**2.9×10^{-4}**	**9.4**	**> 0.99**
GW230806_204041	HL	0.0065	9.4	> 0.99	**0.0035**	**9.1**	**> 0.99**	0.20	9.4	0.97	**0.0035**	**9.1**	**> 0.99**
GW230811_032116	HL	0.0013	13.6	> 0.99	**$< 1.0 \times 10^{-5}$**	**12.9**	**> 0.99**	8.6×10^{-5}	13.3	> 0.99	**$< 1.0 \times 10^{-5}$**	**12.4**	**> 0.99**
GW230814_061920	HL	0.0039	11.2	> 0.99	**5.9×10^{-4}**	**10.2**	**> 0.99**	0.041	10.0	> 0.99	**7.0×10^{-4}**	**9.6**	**> 0.99**
GW230814_230901	L	–	–	–	**$< 1.0 \times 10^{-5}$**	**42.3**	**> 0.99**	–	–	–	**1.0×10^{-3}**	**43.0**	**> 0.99**
GW230819_171910	HL	0.011	9.9	> 0.99	**0.013**	**9.0**	**> 0.99**	–	–	–	***3.5***	***8.9***	***0.82***
GW230820_212515	HL	*68*	*7.9*	*0.10*	**0.24**	**9.1**	**0.98**	0.30	9.3	0.96	**0.28**	**9.0**	**0.97**
GW230824_033047	HL	0.0035	11.1	> 0.99	**$< 1.0 \times 10^{-5}$**	**10.5**	**> 0.99**	0.017	10.6	> 0.99	**$< 1.0 \times 10^{-5}$**	**10.7**	**> 0.99**
GW230825_041334	HL	*1.3*	*8.8*	*0.83*	**0.093**	**8.7**	**0.99**	*1.8*	*8.5*	*0.84*	**0.24**	**8.7**	**0.98**
GW230831_015414	HL	*27*	*7.8*	*0.20*	**0.61**	**8.6**	**0.95**	*1.4*	*8.6*	*0.87*	**0.036**	**8.5**	**> 0.99**
GW230904_051013	HL	–	–	–	**3.7×10^{-5}**	**10.5**	**> 0.99**	4.3×10^{-5}	10.4	> 0.99	**2.9×10^{-4}**	**10.2**	**> 0.99**
GW230911_195324	H	–	–	–	**0.014**	**10.7**	**> 0.99**	–	–	–	**1.0×10^{-3}**	**11.1**	**> 0.99**
GW230914_111401	HL	0.0012	17.2	> 0.99	**$< 1.0 \times 10^{-5}$**	**15.9**	**> 0.99**	$< 1.0 \times 10^{-5}$	16.6	> 0.99	**$< 1.0 \times 10^{-5}$**	**16.0**	**> 0.99**
GW230919_215712	HL	0.0012	16.8	> 0.99	**$< 1.0 \times 10^{-5}$**	**16.3**	**> 0.99**	$< 1.0 \times 10^{-5}$	16.1	> 0.99	**$< 1.0 \times 10^{-5}$**	**16.5**	**> 0.99**
GW230920_071124	HL	0.0012	11.1	> 0.99	**$< 1.0 \times 10^{-5}$**	**10.1**	**> 0.99**	0.11	10.2	0.98	**3.3×10^{-4}**	**9.6**	**> 0.99**
GW230922_020344	HL	0.013	13.4	> 0.99	**$< 1.0 \times 10^{-5}$**	**12.3**	**> 0.99**	4.1×10^{-5}	12.2	> 0.99	**3.4×10^{-4}**	**11.9**	**> 0.99**
GW230922_040658	HL	0.0012	12.5	> 0.99	**$< 1.0 \times 10^{-5}$**	**11.6**	**> 0.99**	3.0×10^{-4}	11.6	> 0.99	**5.3×10^{-4}**	**11.6**	**> 0.99**
GW230924_124453	HL	0.0012	13.5	> 0.99	**$< 1.0 \times 10^{-5}$**	**13.3**	**> 0.99**	$< 1.0 \times 10^{-5}$	13.3	> 0.99	**$< 1.0 \times 10^{-5}$**	**13.0**	**> 0.99**
GW230927_043729	HL	0.0012	12.1	> 0.99	**$< 1.0 \times 10^{-5}$**	**11.3**	**> 0.99**	8.6×10^{-4}	11.1	> 0.99	**$< 1.0 \times 10^{-5}$**	**11.1**	**> 0.99**
GW230927_153832	HL	0.0012	20.3	> 0.99	**$< 1.0 \times 10^{-5}$**	**19.8**	**> 0.99**	$< 1.0 \times 10^{-5}$	20.2	> 0.99	**$< 1.0 \times 10^{-5}$**	**19.6**	**> 0.99**
GW230928_215827	HL	0.0035	10.5	> 0.99	**1.4×10^{-5}**	**9.5**	**> 0.99**	*1.3*	*9.3*	*0.88*	**6.0×10^{-4}**	**9.5**	**> 0.99**
GW230930_110730	HL	*5.4*	*9.0*	*0.58*	**0.17**	**8.5**	**0.98**	*1.1*	*8.6*	*0.89*	**0.095**	**8.3**	**> 0.99**
GW231001_140220	HL	0.0012	11.5	> 0.99	**1.5×10^{-5}**	**10.3**	**> 0.99**	1.8×10^{-4}	10.6	> 0.99	**2.1×10^{-4}**	**9.9**	**> 0.99**
GW231004_232346	HL	0.16	8.9	0.97	***6.4***	***7.9***	***0.68***	–	–	–	**–**	**–**	**–**
GW231005_021030	HL	0.010	10.4	> 0.99	**0.16**	**9.3**	**0.98**	0.019	9.7	> 0.99	**0.023**	**9.8**	**> 0.99**
GW231005_091549	HL	*54*	*11.0*	*0.13*	**0.040**	**8.9**	**> 0.99**	*2.6*	*8.6*	*0.79*	**0.59**	**8.5**	**0.96**
GW231008_142521	HL	–	–	–	**0.0015**	**9.3**	**> 0.99**	*1.6*	*9.1*	*0.86*	**0.017**	**8.7**	**> 0.99**
GW231014_040532	HL	*29*	*8.6*	*0.23*	**0.21**	**9.0**	**0.98**	*1.2*	*8.8*	*0.88*	**0.55**	**8.7**	**0.96**
GW231018_233037	HL	–	–	–	***130***	***8.7***	***0.11***	0.68	9.1	0.93	***42***	***8.6***	***0.29***
GW231020_142947	HL	–	–	–	**$< 1.0 \times 10^{-5}$**	**11.9**	**> 0.99**	$< 1.0 \times 10^{-5}$	12.0	> 0.99	**$< 1.0 \times 10^{-5}$**	**11.8**	**> 0.99**
GW231026_130704	HL	–	–	–	***1.6***	***8.1***	***0.88***	*340*	*8.3*	*0.02*	**0.76**	**8.1**	**0.95**
GW231028_153006	HL	0.0012	22.4	> 0.99	**$< 1.0 \times 10^{-5}$**	**21.0**	**> 0.99**	$< 1.0 \times 10^{-5}$	21.9	> 0.99	**$< 1.0 \times 10^{-5}$**	**21.9**	**> 0.99**
GW231029_111508	L	–	–	–	**5.1×10^{-5}**	**10.8**	**> 0.99**	–	–	–	**–**	**–**	**–**
GW231102_071736	HL	0.0012	15.6	> 0.99	**$< 1.0 \times 10^{-5}$**	**13.8**	**> 0.99**	$< 1.0 \times 10^{-5}$	14.8	> 0.99	**$< 1.0 \times 10^{-5}$**	**13.4**	**> 0.99**
GW231104_133418	HL	–	–	–	**$< 1.0 \times 10^{-5}$**	**11.3**	**> 0.99**	$< 1.0 \times 10^{-5}$	11.4	> 0.99	**$< 1.0 \times 10^{-5}$**	**11.8**	**> 0.99**

Table 6 *continued*

Table 6 *(continued)*

Candidate	Inst.	cWB-BBH			**GstLAL**			MBTA			**PyCBC**		
		FAR (yr^{-1})	SNR	p_{astro}	FAR (yr^{-1})	SNR	p_{astro}	FAR (yr^{-1})	SNR	p_{astro}	FAR (yr^{-1})	SNR	p_{astro}
GW231108_125142	HL	2.1×10^{-4}	12.6	> 0.99	$\mathbf{< 1.0 \times 10^{-5}}$	**12.6**	**> 0.99**	7.5×10^{-5}	12.5	> 0.99	$\mathbf{< 1.0 \times 10^{-5}}$	**12.3**	**> 0.99**
GW231110_040320	HL	–	–	–	$\mathbf{< 1.0 \times 10^{-5}}$	**11.4**	**> 0.99**	8.7×10^{-4}	11.5	> 0.99	$\mathbf{< 1.0 \times 10^{-5}}$	**11.1**	**> 0.99**
GW231113_122623	HL	–	–	–	**0.73**	**8.3**	**0.94**	*38*	*8.6*	*0.16*	**0.063**	**8.6**	**> 0.99**
GW231113_150041	HL	*2.4*	*8.7*	*0.81*	***4.5***	***7.9***	***0.74***	*130*	*8.0*	*0.04*	**0.50**	**7.9**	**0.97**
GW231113_200417	HL	–	–	–	$\mathbf{7.4 \times 10^{-4}}$	**10.3**	**> 0.99**	3.8×10^{-5}	10.1	> 0.99	$\mathbf{2.7 \times 10^{-5}}$	**10.5**	**> 0.99**
GW231114_043211	HL	–	–	–	$\mathbf{1.2 \times 10^{-4}}$	**10.0**	**> 0.99**	2.0×10^{-4}	9.9	> 0.99	$\mathbf{6.2 \times 10^{-4}}$	**9.6**	**> 0.99**
GW231118_005626	HL	–	–	–	$\mathbf{1.1 \times 10^{-5}}$	**10.4**	**> 0.99**	$< 1.0 \times 10^{-5}$	10.7	> 0.99	$\mathbf{1.1 \times 10^{-5}}$	**10.5**	**> 0.99**
GW231118_071402	HL	0.078	9.2	> 0.99	**0.0046**	**9.2**	**> 0.99**	0.50	9.2	0.93	$\mathbf{2.2 \times 10^{-4}}$	**9.2**	**> 0.99**
GW231118_090602	HL	–	–	–	$\mathbf{< 1.0 \times 10^{-5}}$	**10.8**	**> 0.99**	$< 1.0 \times 10^{-5}$	11.0	> 0.99	$\mathbf{1.0 \times 10^{-5}}$	**10.8**	**> 0.99**
GW231119_075248	HL	*22*	*7.9*	*0.30*	**0.50**	**8.1**	**0.96**	*1.9*	*8.0*	*0.83*	**0.0029**	**8.3**	**> 0.99**
GW231123_135430	HL	1.0×10^{-4}	21.8	> 0.99	$\mathbf{< 1.0 \times 10^{-5}}$	**20.1**	**> 0.99**	0.016	19.0	> 0.99	**0.0020**	**19.9**	**> 0.99**
GW231127_165300	HL	0.010	9.9	> 0.99	**0.030**	**9.8**	**> 0.99**	0.24	9.5	0.96	**0.23**	**9.6**	**0.98**
GW231129_081745	HL	0.056	9.4	> 0.99	**0.22**	**8.5**	**0.98**	*2.3*	*8.4*	*0.80*	**0.35**	**8.5**	**0.97**
GW231206_233134	HL	0.0012	12.8	> 0.99	$\mathbf{< 1.0 \times 10^{-5}}$	**11.9**	**> 0.99**	0.074	11.7	0.98	$\mathbf{1.6 \times 10^{-5}}$	**11.5**	**> 0.99**
GW231206_233901	HL	0.0012	21.9	> 0.99	$\mathbf{< 1.0 \times 10^{-5}}$	**20.7**	**> 0.99**	$< 1.0 \times 10^{-5}$	21.4	> 0.99	$\mathbf{1.6 \times 10^{-5}}$	**21.0**	**> 0.99**
GW231213_111417	HL	0.0046	10.0	> 0.99	$\mathbf{< 1.0 \times 10^{-5}}$	**10.2**	**> 0.99**	0.029	10.4	> 0.99	$\mathbf{4.9 \times 10^{-5}}$	**10.1**	**> 0.99**
GW231221_135041	HL	0.54	10.0	0.96	***8.5***	***8.4***	***0.62***	*520*	*8.1*	*< 0.01*	***110***	***8.3***	***0.11***
GW231223_032836	HL	0.0046	10.2	> 0.99	$\mathbf{3.6 \times 10^{-4}}$	**9.4**	**> 0.99**	*13*	*9.1*	*0.42*	$\mathbf{4.4 \times 10^{-4}}$	**9.0**	**> 0.99**
GW231223_075055	HL	–	–	–	***9.4***	***9.3***	***0.59***	*1.6*	*9.4*	*0.85*	**0.23**	**9.4**	**0.98**
GW231223_202619	H	–	–	–	***3.2***	***10.1***	***0.80***	–	–	–	**0.0020**	**10.0**	**> 0.99**
GW231224_024321	HL	–	–	–	$\mathbf{< 1.0 \times 10^{-5}}$	**13.0**	**> 0.99**	$< 1.0 \times 10^{-5}$	14.0	> 0.99	$\mathbf{< 1.0 \times 10^{-5}}$	**13.3**	**> 0.99**
GW231226_101520	HL	0.0012	34.7	> 0.99	$\mathbf{< 1.0 \times 10^{-5}}$	**34.2**	**> 0.99**	$< 1.0 \times 10^{-5}$	33.6	> 0.99	$\mathbf{< 1.0 \times 10^{-5}}$	**33.2**	**> 0.99**
GW231230_170116	HL	0.42	8.2	0.96	***72***	***8.0***	***0.19***	–	–	–	**–**	**–**	**–**
GW231231_154016	H	–	–	–	$\mathbf{< 1.0 \times 10^{-5}}$	**13.4**	**> 0.99**	–	–	–	$\mathbf{1.0 \times 10^{-3}}$	**13.4**	**> 0.99**
GW240104_164932	H	–	–	–	$\mathbf{< 1.0 \times 10^{-5}}$	**14.8**	**> 0.99**	–	–	–	**0.042**	**12.2**	**> 0.99**
GW240107_013215	HL	0.37	9.4	0.95	**0.23**	**9.1**	**0.98**	0.24	9.6	0.96	**0.0094**	**9.1**	**> 0.99**
GW240109_050431	H	–	–	–	$\mathbf{2.2 \times 10^{-4}}$	**10.4**	**> 0.99**	–	–	–	$\mathbf{1.0 \times 10^{-3}}$	**10.0**	**> 0.99**

NOTE— The date and time of each candidate is encoded in the name as GWYYMMDD_hhmmss. The candidate properties produced by PyCBC and GstLAL pipelines are given in **bold**. The detectors that were observing at the time of each transient are denoted by a single-letter (e.g., H for LIGO Hanford). This does not necessarily indicate that the same detectors contributed triggers for a given candidate. We include results from pipelines that observe a candidate with FAR $\geq 1\,\mathrm{yr}^{-1}$ in *italics*. A dash (–) indicates that a candidate was not found by an analysis. There is evidence that the candidate labeled with an asterisk (*) is of instrumental origin. FARs have been capped at $1 \times 10^{-5}\,\mathrm{yr}^{-1}$ to maintain a consistent limiting FAR across pipelines.

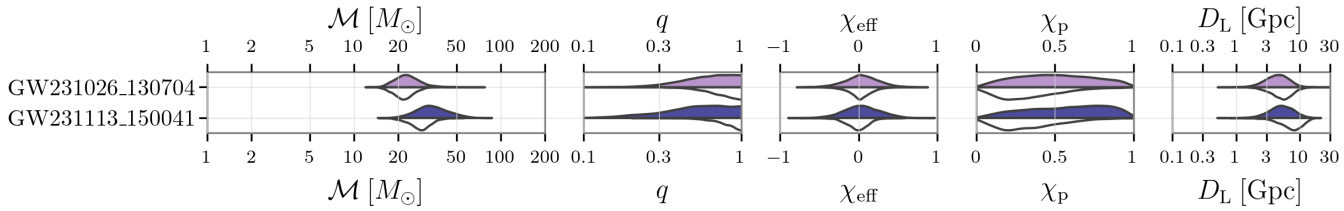

Figure 9. The marginal probability distributions for the source frame chirp mass $\mathcal{M}$, mass ratio q, effective inspiral spin $\chi_{\rm eff}$, effective precession spin $\chi_{\rm p}$, and luminosity distance $D_{\rm L}$ for the two O4a candidates with a FAR $< 1\,{\rm yr}^{-1}$. The vertical thickness of each region is proportional to the marginal posterior probability at that value for each candidate.

Table 7. The inferred properties of new GW candidates from O4a with a FAR $< 1\,{\rm yr}^{-1}$ and $p_{\rm astro} \geq 0.5$. For one-dimensional distributions, we provide the median and 90% symmetric credible intervals, while for the localization area $\Delta\Omega$ we provide the 90% credible area.

Candidate	M $[M_\odot]$	$\mathcal{M}$ $[M_\odot]$	m_1 $[M_\odot]$	m_2 $[M_\odot]$	$\chi_{\rm eff}$	$D_{\rm L}$ [Gpc]	z	$M_{\rm f}$ $[M_\odot]$	$\chi_{\rm f}$	$\Delta\Omega$ [deg^2]	SNR
GW231026_130704	55^{+29}_{-14}	$22.8^{+10.3}_{-5.7}$	34^{+27}_{-11}	$20.8^{+9.8}_{-8.2}$	$0.03^{+0.36}_{-0.36}$	$4.4^{+4.0}_{-2.4}$	$0.71^{+0.49}_{-0.33}$	53^{+28}_{-13}	$0.70^{+0.14}_{-0.17}$	3500	$7.3^{+0.4}_{-0.7}$
GW231113_150041	85^{+46}_{-26}	34^{+18}_{-11}	56^{+38}_{-22}	29^{+18}_{-16}	$0.04^{+0.39}_{-0.37}$	$5.2^{+5.1}_{-2.8}$	$0.80^{+0.60}_{-0.38}$	82^{+44}_{-25}	$0.70^{+0.16}_{-0.19}$	4800	$7.4^{+0.6}_{-0.7}$

NOTE—The columns show the source-frame total mass M, source-frame chirp mass $\mathcal{M}$, source-frame component masses m_i, effective inspiral spin $\chi_{\rm eff}$, luminosity distance $D_{\rm L}$, redshift z, source-frame remnant mass $M_{\rm f}$, remnant spin $\chi_{\rm f}$, localization area $\Delta\Omega$, and SNR.

B. ADDITIONAL SEARCH RESULTS

We present the individual-detector SNRs for all O4b candidates with a FAR $< 1\,{\rm yr}^{-1}$ in Table 8, extending the information provided in Table 1 and offering additional context on the search pipeline responses to the signals observed in data from individual detectors.

Table 8. Individual-detector SNRs for all candidates with a FAR $< 1\,{\rm yr}^{-1}$.

Candidate	cWB-BBH			GSTLAL			MBTA			PyCBC		
	H	L	V	H	L	V	H	L	V	H	L	V
GW240406_062847	–	–	–	8.4	7.4	–	8.5	7.1	–	8.4	7.5	–
GW240413_022019	7.5	10.5	–	9.0	14.0	–	9.5	14.8	4.3	9.4	14.8	–
GW240414_054515	–	–	–	9.1	–	5.6	9.5	–	5.9	8.9	–	6.2
GW240420_175625	–	–	–	*10.0*	–	–	–	–	–	9.9	–	–
GW240426_031451	5.6	8.6	–	5.8	7.3	–	6.4	7.6	–	6.3	7.6	–
GW240428_225440	–	–	–	14.1	–	6.5	14.1	–	6.7	14.0	–	6.6
GW240501_033534	7.4	7.4	–	6.7	7.0	–	7.0	7.3	2.9	6.6	7.4	–
GW240505_133552	5.7	7.2	–	5.8	6.1	–	*6.5*	*6.4*	*2.3*	5.5	5.8	–
GW240507_041632	–	–	–	6.3	7.3	–	6.3	7.2	3.5	6.4	6.9	–
GW240511_031507	9.7	12.9	–	8.8	12.3	5.0	9.0	12.8	4.7	8.2	12.4	5.2
GW240512_024139	–	–	–	6.9	8.1	–	7.0	8.4	3.7	6.9	7.9	–
GW240513_183302	10.4	9.1	–	8.9	10.4	4.6	8.9	9.8	4.6	9.0	9.6	4.8
GW240514_121713	13.5	10.2	–	12.3	9.3	–	12.5	10.0	2.0	12.0	9.9	–
GW240515_005301	*8.2*	*9.8*	–	6.8	8.9	–	*6.6*	*8.7*	*2.1*	6.2	8.4	–
GW240519_012815	–	–	–	–	9.2	4.7	–	–	–	–	9.4	4.9
GW240520_213616	–	–	–	7.3	8.4	–	7.0	8.9	3.7	7.1	8.7	–

Table 8 *continued*

Table 8 *(continued)*

Candidate	cWB-BBH			GSTLAL			MBTA			PyCBC		
	H	L	V	H	L	V	H	L	V	H	L	V
GW240525_031210	–	–	–	5.9	6.3	–	*5.6*	*6.2*	*3.4*	*5.7*	*5.8*	–
GW240526_093944	–	–	–	–	–	–	8.1	4.6	2.8	–	–	–
GW240527_183429	8.2	6.3	–	7.2	5.6	–	7.7	5.8	1.6	7.8	6.1	–
GW240527_230910	*6.8*	*6.5*	–	7.6	5.7	4.8	7.7	6.2	4.8	7.6	5.9	–
GW240530_012417	*6.4*	*6.8*	–	5.7	8.9	–	5.2	9.1	1.7	5.4	8.4	–
GW240531_040326	–	–	–	*7.5*	*4.4*	–	–	–	–	7.2	5.0	–
GW240531_075248	*5.8*	*6.8*	–	4.8	7.3	–	5.1	7.6	1.6	5.1	7.7	–
GW240601_061200	6.5	7.5	–	*4.7*	*6.8*	–	*4.9*	*7.5*	*2.2*	*4.4*	*7.3*	–
GW240601_231004	–	–	–	5.8	7.6	–	6.2	7.9	2.6	6.1	8.1	–
GW240612_081540	*7.7*	*6.1*	–	*6.6*	*4.1*	–	6.7	4.8	1.8	6.8	4.6	–
GW240615_113620	16.6	19.7	–	16.2	19.3	5.3	16.5	19.9	5.4	15.8	20.5	5.6
GW240615_160735	*9.1*	*9.4*	–	7.2	7.3	–	7.3	7.5	2.0	7.4	7.7	–
GW240618_071627	5.4	6.9	–	5.1	6.1	–	5.4	6.2	–	*5.2*	*6.2*	–
GW240621_195059	22.8	16.6	–	22.3	15.2	–	22.4	16.1	3.8	22.4	15.4	–
GW240621_200935	6.4	8.6	–	5.2	7.9	–	5.2	8.7	1.5	4.7	8.7	–
GW240621_214041	*5.1*	*5.6*	–	*4.6*	*6.1*	–	*4.6*	*6.3*	*1.4*	4.7	6.4	–
GW240622_004008	7.6	6.4	–	9.4	7.9	–	9.7	8.0	2.1	9.8	7.9	–
GW240627_131622	–	–	–	6.7	6.3	–	6.6	6.4	3.4	6.8	6.3	–
GW240629_145256	–	–	–	6.8	10.2	–	7.3	10.2	2.3	7.1	10.2	–
GW240630_101703	8.1	6.8	–	7.8	6.3	–	7.5	6.4	2.0	7.7	6.2	–
GW240703_191355	–	–	–	–	9.3	4.0	–	–	–	–	9.8	–
GW240705_053215	11.2	12.5	–	8.9	10.5	–	9.2	12.0	2.3	9.2	12.1	–
GW240716_034900	–	–	–	–	12.4	–	–	–	–	–	*11.7*	–
GW240824_205609	6.4	5.7	–	*5.7*	*5.5*	–	*5.6*	*5.3*	*4.6*	*5.5*	*5.3*	–
GW240825_055146	–	–	–	7.2	6.2	–	7.6	6.4	2.6	7.0	6.7	–
GW240830_211120	–	–	–	7.8	7.5	–	7.9	7.3	2.6	7.7	7.6	–
GW240902_143306	*7.2*	*6.3*	–	7.9	6.5	–	8.3	6.3	1.9	8.2	6.1	–
GW240907_153833	7.0	7.8	–	6.1	6.8	–	6.5	7.4	1.8	6.4	7.2	–
GW240908_082628	7.4	6.5	–	7.1	6.5	5.6	6.6	6.8	5.3	7.0	6.7	–
GW240908_125134	–	–	–	4.7	6.5	–	4.5	6.9	2.3	*4.2*	*6.5*	–
GW240910_103535	11.7	10.2	–	11.9	13.3	–	12.1	13.1	–	11.9	13.2	–
GW240915_001357	11.3	11.6	–	8.8	11.7	–	10.4	12.1	3.8	10.2	12.2	–
GW240915_105151	–	–	–	13.3	–	–	–	–	–	13.9	–	–
GW240916_184352	–	–	–	5.7	7.1	–	5.9	7.3	2.8	5.9	6.9	–
GW240919_061559	9.7	12.9	–	9.4	12.3	5.7	9.6	12.8	5.6	9.5	12.3	5.3
GW240920_073424	10.1	9.6	–	9.5	8.1	–	9.9	8.3	2.0	10.0	8.2	–
GW240920_124024	23.5	29.1	–	22.9	28.5	–	23.0	28.8	–	22.7	29.1	–
GW240921_201835	–	–	–	–	10.0	4.7	–	10.2	4.9	–	10.5	–
GW240922_142106	*7.2*	*8.7*	–	7.3	9.2	–	7.6	9.6	2.9	8.1	8.4	–
GW240923_204006	8.1	10.9	–	6.9	8.9	–	6.8	10.0	2.5	6.4	9.8	–
GW240924_000316	8.8	7.3	–	7.9	6.3	–	7.7	6.3	2.1	6.9	5.8	–
GW240925_005809	17.2	24.0	–	16.8	25.5	–	17.3	25.8	2.4	17.3	25.7	–
GW240930_035959	10.4	11.6	–	8.8	12.0	–	9.0	12.7	4.2	9.0	12.5	–
GW240930_234614	6.6	9.1	–	–	–	–	–	–	–	–	–	–
GW241002_030559	–	–	–	–	10.4	4.9	–	10.7	5.2	–	10.2	5.3
GW241006_015333	13.3	11.6	–	12.1	10.9	–	12.5	11.1	2.4	12.7	10.5	–
GW241007_082943	7.5	5.9	–	*8.2*	*4.2*	–	8.2	4.6	2.6	*8.0*	*4.4*	–
GW241009_022835	–	–	–	4.1	7.0	–	*4.4*	*6.9*	*1.4*	4.5	7.1	–

Table 8 *continued*

Table 8 *(continued)*

Candidate	cWB-BBH			GSTLAL			MBTA			PyCBC		
	H	L	V	H	L	V	H	L	V	H	L	V
GW241009_084816	–	–	–	8.1	6.9	4.0	8.8	7.7	3.2	8.7	7.9	–
GW241009_220455	–	–	–	6.0	6.3	4.4	6.2	6.4	4.5	6.1	6.3	4.7
GW241011_233834	–	–	–	33.5	–	8.5	34.5	–	9.1	34.7	–	8.7
GW241101_220523	–	–	–	–	9.9	–	–	–	–	–	*10.4*	–
GW241102_124058	14.8	13.3	–	14.7	14.6	–	15.3	15.0	3.7	15.4	14.8	–
GW241102_144729	8.6	9.3	–	8.3	7.9	–	8.7	7.8	3.3	8.4	7.7	–
GW241109_033317	–	–	–	–	10.2	–	–	10.4	4.5	–	10.0	4.3
GW241109_115924	–	–	–	11.6	–	–	11.7	–	2.2	11.7	–	–
GW241110_124123	–	–	–	7.2	6.5	–	7.1	6.9	2.2	7.3	7.0	–
GW241111_111552	13.4	9.3	–	13.5	7.9	–	13.6	8.1	–	13.2	7.6	–
GW241113_163507	–	–	–	–	12.3	–	–	–	–	–	12.5	–
GW241114_024711	8.7	7.2	–	7.5	6.9	–	*7.4*	*6.9*	*2.5*	7.5	7.0	–
GW241114_235258	–	–	–	–	12.1	–	–	–	–	–	11.6	–
GW241116_151753	7.4	6.6	–	7.8	5.4	–	8.5	5.5	2.5	6.9	5.8	–
GW241124_024914	*5.7*	*6.2*	–	*5.7*	*5.6*	–	*5.7*	*6.1*	*2.4*	5.5	6.4	–
GW241125_010116	8.1	7.4	–	7.0	6.6	–	7.1	7.3	2.4	7.3	6.7	–
GW241127_061008	24.7	19.2	–	24.1	17.1	–	25.1	18.0	4.6	24.8	18.1	–
GW241129_021832	12.7	10.9	–	12.1	10.2	–	12.3	10.6	2.2	11.8	10.4	–
GW241130_034908	10.7	7.7	–	11.5	6.1	–	11.7	6.5	3.2	11.3	6.3	–
GW241130_110422	–	–	–	7.6	5.4	–	8.0	5.8	2.7	7.9	5.6	–
GW241201_055758	*7.4*	*4.9*	–	7.0	4.2	–	*6.8*	*4.8*	*3.5*	*6.2*	*4.2*	–
GW241210_060606	8.3	10.6	–	8.1	8.9	–	8.1	9.2	2.6	8.3	9.3	–
GW241210_120900	*5.6*	*6.9*	–	4.8	7.0	–	*5.4*	*7.2*	–	*4.9*	*6.7*	–
GW241225_042553	–	–	–	–	16.2	–	–	–	–	–	16.4	–
GW241225_082815	11.9	15.4	–	11.1	13.5	–	10.9	14.2	–	10.4	14.5	–
GW241229_155844	*5.2*	*6.0*	–	*5.5*	*6.1*	–	*5.0*	*6.1*	*2.9*	5.4	5.8	–
GW241230_084504	–	–	–	–	10.9	–	–	–	–	–	–	–
GW241230_233618	6.2	10.4	–	4.1	9.3	–	–	–	–	–	–	–
GW241231_054133	12.7	11.0	–	12.6	11.5	–	13.0	11.2	2.6	12.6	11.0	–
GW250101_011205	–	–	–	5.0	7.7	–	4.5	8.2	2.7	4.7	7.7	–
GW250104_015122	8.1	9.0	–	6.9	8.6	–	7.2	8.8	2.2	7.4	8.7	–
GW250108_152221	9.9	6.5	–	9.2	6.1	–	9.6	6.0	2.1	9.5	5.7	–
GW250109_010541	8.6	9.8	–	6.2	9.9	–	6.0	10.2	3.2	5.9	9.2	–
GW250109_074552	–	–	–	9.9	–	4.0	*8.9*	–	*4.5*	*8.5*	–	*4.4*
GW250114_082203	49.3	53.5	–	51.4	56.8	–	52.0	59.0	–	51.4	58.2	–
GW250116_015318	–	–	–	*5.8*	*4.8*	–	*5.5*	*5.2*	*2.0*	5.7	5.4	–
GW250118_023225	6.2	6.5	–	5.7	6.5	–	*5.8*	*6.3*	*1.9*	5.6	6.3	–
GW250118_055802	*6.1*	*7.6*	–	6.8	6.8	4.3	6.9	6.8	3.2	6.6	7.0	–
GW250118_170523	8.5	11.0	–	8.9	9.9	–	9.0	10.1	–	8.8	9.6	–
GW250119_025138	9.3	10.9	–	9.8	9.8	–	10.4	9.9	2.0	9.6	9.9	–
GW250119_190238	12.5	15.7	–	12.7	14.6	5.1	13.4	15.9	4.7	13.0	15.4	–

NOTE—LIGO Hanford, LIGO Livingston, and Virgo are denoted by H, L, and V, respectively. Entries in *italics* indicate candidates that were recovered with a FAR $\geq 1\,\mathrm{yr}^{-1}$ by a given analysis. Dashes (–) indicate that a candidate was not found by an analysis.

In Table 9 we provide the calculated probabilities that a candidate comes from a BBH (p_{BBH}), an NSBH (p_{NSBH}), or a BNS (p_{BNS}) for some new candidates in GWTC-5.0 with the maximum $p_{\mathrm{astro}} > 0.5$ and minimum FARs $> 1\,\mathrm{yr}^{-1}$ across pipelines. We only show systems where $p_{\mathrm{NSBH}} + p_{\mathrm{BNS}} > 0.001$; the remaining marginal candidates are consistent with BBHs. GSTLAL estimates the relative probabilities of different astrophysical source types using the component masses of the matching template,

and the SNR of the signal (Ray et al. 2023); MBTA uses the chirp mass and mass ratio of the identifying template (Andres et al. 2022), and PyCBC only uses the chirp mass, along with an estimate of the source luminosity distance (Dal Canton et al. 2021; Villa-Ortega et al. 2022). Neglecting mass ratio information can systematically impact the source categorization (Villa-Ortega et al. 2022). The full details of the $p_{\rm astro}$ calculations are described in Abac et al. (2026b).

Table 9. Multicomponent $p_{\rm astro}$ for all candidates with FAR $\geq 1\,{\rm yr}^{-1}$, $p_{\rm astro} \geq 0.5$ and $p_{\rm BNS} + p_{\rm NSBH} > 0.001$.

Candidate	cWB-BBH	GstLAL				MBTA				PyCBC			
	$p_{\rm astro}$	$p_{\rm BBH}$	$p_{\rm NSBH}$	$p_{\rm BNS}$	$p_{\rm astro}$	$p_{\rm BBH}$	$p_{\rm NSBH}$	$p_{\rm BNS}$	$p_{\rm astro}$	$p_{\rm BBH}$	$p_{\rm NSBH}$	$p_{\rm BNS}$	$p_{\rm astro}$
GW240512_051606	–	–	–	–	–	*0.68*	*0.02*	*< 0.01*	*0.70*	–	–	–	–
GW240807_214559	–	*0.03*	*< 0.01*	*< 0.01*	*0.03*	–	–	–	–	*0.57*	*0.09*	*< 0.01*	*0.66*
GW240813_034548	–	*0.03*	*< 0.01*	*< 0.01*	*0.03*	–	–	–	–	*0.57*	*0.07*	*< 0.01*	*0.64*
GW240907_121650	–	–	–	–	–	*< 0.01*	*0.34*	*0.18*	*0.52*	–	–	–	–
GW241129_140416	–	–	–	–	–	–	–	–	–	*0.48*	*0.03*	*< 0.01*	*0.51*
GW250109_083206	–	–	–	–	–	–	–	–	–	*0.80*	*0.20*	*< 0.01*	*> 0.99*

NOTE—These candidates do not meet the criterion for source property estimation. Entries in *italics* indicate candidates that were recovered with a FAR $\geq 1\,{\rm yr}^{-1}$ by a given analysis. Dashes (–) indicate that a candidate was not found by an analysis. The BBH, BNS, and NSBH categories are defined by the masses of the search template that recovered the candidate and are not necessarily indicative of true astrophysical population.

C. GLITCH MITIGATION

When a glitch is identified around the time of a candidate, we carry out further procedures to mitigate its impact on our inferences described in Section 4 of Abac et al. (2026b). For the candidates identified in O4b, we can model and coherently subtract the glitch with the BayesWave algorithm (Cornish & Littenberg 2015; Littenberg & Cornish 2015; Cornish et al. 2021; Hourihane et al. 2022; Abac et al. 2026b); integrate the parameter-estimation likelihood in a narrower frequency band to exclude the effect of the glitch by increasing the low-frequency cutoff $f_{\rm low}$, or do both. For cases where we applied BayesWave, Table 10 shows input parameters for the algorithm: the reference trigger time of the CBC candidate as determined by GW searches, and the bands in time and frequency space where the glitch is *a priori* identified to have power. For cases where we narrow the frequency band, we give the $f_{\rm low}$ value used to set the lower bound; the upper bound $f_{\rm high}$ is the Nyquist frequency multiplied by a roll-off factor as described in Abac et al. (2026b).

Table 10. List of O4b candidates with FAR < $1\,{\rm yr}^{-1}$, for which glitch mitigation was performed.

Candidate	GPS time [s]	Detector	Time window [s]	Frequency range [Hz]	$f_{\rm low}$ [Hz]
GW240413_022019	–	L	–	–	30
GW240514_121713	1399724251.72	L	$[0.70, 2.00]$	[20, 35]	–
GW240515_005301	1399769599.11	L	$[-4.01, -3.01]$	[10, 50]	–
GW240520_213616	1400276194.97	L	$[-0.28, -0.04]$	[60, 90]	–
GW240525_031210	1400641948.64	L	$[-4.64, -4.24]$	[10, 30]	–
GW240531_075248	1401177186.46	V	$[-0.30, -0.20]$	[120, 200]	–
GW240601_061200	1401257538.36	L	$[0.52, 0.73]$	[200, 300]	–
GW240601_231004	1401318622.03	L	$[-5.30, -4.55]$	[20, 30]	–
GW240612_081540	–	L	–	–	30
GW240615_160735	1402502873.33	L	$[-0.05, -0.01]$	[100, 300]	–
GW240621_200935	1403035793.53	L	$[0.30, 0.40]$	[200, 300]	–
GW240621_200935	1403035793.53	V	$[-1.80, -1.60]$	[100, 200]	–
GW240629_145256	1403707994.86	H	$[-3.10, -2.90]$	[250, 400]	20.88
GW240629_145256	–	L	–	–	20.88
GW240629_145256	–	V	–	–	20.88

Table 10 *continued*

Table 10 *(continued)*

Candidate	GPS time [s]	Detector	Time window [s]	Frequency range [Hz]	$f_{\rm low}$ [Hz]
GW240705_053215	1404192753.92	V	[0.90, 1.10]	[50, 100]	–
GW240902_143306	1409322804.76	V	[−0.10, 0.10]	[300, 400]	–
GW240908_082628	1409819206.41	V	[−0.18, 0.03]	[164, 210]	–
GW240908_082628	–	L	–	–	30
GW240908_125134	1409835112.27	L	[0.60, 1.20]	[20, 30]	–
GW240919_061559	1410761777.19	H	[0.20, 0.80]	[20, 30]	–
GW240920_124024	1410871242.88	L	[0.002, 0.30]	[20, 35]	–
GW240921_201835	1410985133.79	L	[−4.60, −4.20]	[10, 30]	–
GW240922_142106	1411050084.39	H	[−0.40, −0.20]	[150, 250]	–
GW240923_204006	–	H	–	–	21.28
GW240923_204006	–	L	–	–	21.28
GW240923_204006	–	V	–	–	21.28
GW240930_035959	1411704017.96	L	[1.00, 1.80]	[10, 800]	–
GW241009_220455	1412546713.52	L	[−0.22, 0.58]	[10, 30]	–
GW241102_144729	1414594067.73	L	[−2.58, −1.63]	[10, 30]	–
GW241109_033317	1415158416.00	L	[0.60, 1.00]	[10, 50]	–
GW241110_124123	–	L	–	–	30
GW241111_111552	–	L	–	–	30
GW241113_163507	–	L	–	–	30
GW241114_024711	–	L	–	–	30
GW241114_235258	–	L	–	–	30
GW241125_010116	1416531694.78	H	[−0.60, −0.30]	[20, 40]	–
GW241127_061008	–	L	–	–	30
GW241130_034908	–	V	–	–	70
GW241201_055758	–	V	–	–	50
GW250108_152221	–	L	–	–	30
GW250109_010541	–	L	–	–	30
GW250109_010541	–	V	–	–	60
GW250119_190238	–	L	–	–	30

NOTE— For each candidate, we show the GPS time, and the interferometer(s) where glitch subtraction was applied (H, L and V indicate LIGO Hanford, LIGO Livingston and Virgo respectively). For candidates where glitch subtraction was performed using BAYESWAVE, we provide the time and frequency windows used for subtraction. For candidates where the low-frequency cutoff, $f_{\rm low}$, was changed (from the standard 20 Hz) to excise contaminate data, we quote the cutoff used.

REFERENCES

Aasi, J., Abbott, B. P., Abbott, R., et al. 2015, Classical and Quantum Gravity, 32, 074001, doi: 10.1088/0264-9381/32/7/074001

Abac, A. G., Abouelfettouh, I., Acernese, F., et al. 2025, arXiv e-prints, arXiv:2509.07348, doi: 10.48550/arXiv.2509.07348

Abac, A. G., Abouelfettouh, I., Acernese, F., et al. 2026a, To be published in this issue. https://dcc.ligo.org/LIGO-P2500701/public

—. 2026b, To be published in this issue. https://dcc.ligo.org/LIGO-P2600166/public

—. 2026c, To be published in this issue. https://dcc.ligo.org/LIGO-P2600085/public

—. 2026d, To be published in this issue. https://dcc.ligo.org/LIGO-P2600045/public

—. 2026e, To be published in this issue. https://dcc.ligo.org/LIGO-P2600018/public

—. 2026f, To be published in this issue

—. 2026g, To be published in this issue

—. 2026h, To be published in this issue

Abac, A. G., Abbott, R., Abe, H., et al. 2024, ApJ, 973, 132, doi: 10.3847/1538-4357/ad65ce

Abac, A. G., et al. 2025

Abac, A. G., Abouelfettouh, I., Acernese, F., et al. 2025a, arXiv e-prints, arXiv:2508.18082, doi: 10.48550/arXiv.2508.18082

—. 2025b, PhRvL, 135, 111403, doi: 10.1103/kw5g-d732
—. 2025c, ApJL, 993, L21, doi: 10.3847/2041-8213/ae0d54
—. 2025d, PhRvD, 112, 102005, doi: 10.1103/wjdz-jdby
—. 2025e, ApJL, 993, L25, doi: 10.3847/2041-8213/ae0c9c
Abac, A. G., et al. 2025
Abac, A. G., Abouelfettouh, I., Acernese, F., et al. 2025, arXiv e-prints, arXiv:2508.18081, doi: 10.48550/arXiv.2508.18081
—. 2026a, arXiv e-prints, arXiv:2605.11703. https://arxiv.org/abs/2605.11703
—. 2026b, PhRvL, 136, 041403, doi: 10.1103/6c61-fm1n
Abbott, B. P., Abbott, R., Abbott, T. D., et al. 2016a, PhRvL, 116, 061102, doi: 10.1103/PhysRevLett.116.061102
—. 2016b, PhRvL, 116, 241102, doi: 10.1103/PhysRevLett.116.241102
—. 2016c, Physical Review X, 6, 041015, doi: 10.1103/PhysRevX.6.041015
—. 2016d, Physical Review X, 6, 041014, doi: 10.1103/PhysRevX.6.041014
—. 2017a, PhRvL, 119, 161101, doi: 10.1103/PhysRevLett.119.161101
—. 2017b, PhRvD, 95, 042003, doi: 10.1103/PhysRevD.95.042003
—. 2017c, PhRvL, 118, 221101, doi: 10.1103/PhysRevLett.118.221101
—. 2018, PhRvL, 121, 231103, doi: 10.1103/PhysRevLett.121.231103
—. 2019a, Physical Review X, 9, 031040, doi: 10.1103/PhysRevX.9.031040
—. 2019b, ApJ, 875, 161, doi: 10.3847/1538-4357/ab0e8f
—. 2019c, PhRvD, 100, 024017, doi: 10.1103/PhysRevD.100.024017
—. 2019d, Physical Review X, 9, 011001, doi: 10.1103/PhysRevX.9.011001
—. 2019e, PhRvL, 123, 161102, doi: 10.1103/PhysRevLett.123.161102
—. 2020, Classical and Quantum Gravity, 37, 055002, doi: 10.1088/1361-6382/ab685e
Abbott, B. P., et al. 2020, Living Rev. Rel., 23, 3, doi: 10.1007/s41114-020-00026-9
Abbott, B. P., Abbott, R., Abbott, T. D., et al. 2020, ApJL, 892, L3, doi: 10.3847/2041-8213/ab75f5
Abbott, R., Abbott, T. D., Abraham, S., et al. 2021a, ApJL, 915, L5, doi: 10.3847/2041-8213/ac082e
—. 2021b, Physical Review X, 11, 021053, doi: 10.1103/PhysRevX.11.021053
Abbott, R., Abbott, T. D., Acernese, F., et al. 2021c, PhRvD, 104, 122004, doi: 10.1103/PhysRevD.104.122004
Abbott, R., Abbott, T. D., Abraham, S., et al. 2021d, ApJ, 921, 80, doi: 10.3847/1538-4357/ac17ea
—. 2021e, PhRvL, 126, 241102, doi: 10.1103/PhysRevLett.126.241102
—. 2021f, PhRvD, 104, 022004, doi: 10.1103/PhysRevD.104.022004
—. 2021g, PhRvD, 104, 022005, doi: 10.1103/PhysRevD.104.022005
Abbott, R., Abbott, T. D., Acernese, F., et al. 2022a, PhRvL, 129, 061104, doi: 10.1103/PhysRevLett.129.061104
—. 2022b, ApJ, 932, 133, doi: 10.3847/1538-4357/ac6ad0
—. 2023a, Physical Review X, 13, 041039, doi: 10.1103/PhysRevX.13.041039
—. 2023b, Physical Review X, 13, 011048, doi: 10.1103/PhysRevX.13.011048
Abbott, R., Abe, H., Acernese, F., et al. 2023c, MNRAS, 524, 5984, doi: 10.1093/mnras/stad588
Abbott, R., Abbott, T. D., Acernese, F., et al. 2024, PhRvD, 109, 022001, doi: 10.1103/PhysRevD.109.022001
Acernese, F., Agathos, M., Agatsuma, K., et al. 2015, Classical and Quantum Gravity, 32, 024001, doi: 10.1088/0264-9381/32/2/024001
Acernese, F., Agathos, M., Ain, A., et al. 2023, Classical and Quantum Gravity, 40, 185005, doi: 10.1088/1361-6382/acdf36
Adams, T., Buskulic, D., Germain, V., et al. 2016, Classical and Quantum Gravity, 33, 175012, doi: 10.1088/0264-9381/33/17/175012
Ade, P. A. R., Aghanim, N., Arnaud, M., et al. 2016, A&A, 594, A13, doi: 10.1051/0004-6361/201525830
Ajith, P., Hannam, M., Husa, S., et al. 2011, PhRvL, 106, 241101, doi: 10.1103/PhysRevLett.106.241101
Akutsu, T., Ando, M., Arai, K., et al. 2021, Progress of Theoretical and Experimental Physics, 2021, 05A101, doi: 10.1093/ptep/ptaa125
Alléné, C., Aubin, F., Bentara, I., et al. 2025, Classical and Quantum Gravity, 42, 105009, doi: 10.1088/1361-6382/add234
Alsing, J., Silva, H. O., & Berti, E. 2018, MNRAS, 478, 1377, doi: 10.1093/mnras/sty1065
Álvarez-López, S., Liyanage, A., Ding, J., Ng, R., & McIver, J. 2024, Classical and Quantum Gravity, 41, 085007, doi: 10.1088/1361-6382/ad2194
Andres, N., Assiduo, M., Aubin, F., et al. 2022, Classical and Quantum Gravity, 39, 055002, doi: 10.1088/1361-6382/ac482a
Antoniadis, J., Tauris, T. M., Ozel, F., et al. 2016, arXiv e-prints, arXiv:1605.01665, doi: 10.48550/arXiv.1605.01665
Apostolatos, T. A., Cutler, C., Sussman, G. J., & Thorne, K. S. 1994, PhRvD, 49, 6274, doi: 10.1103/PhysRevD.49.6274
Areeda, J. S., Smith, J. R., Lundgren, A. P., et al. 2017, Astronomy and Computing, 18, 27, doi: 10.1016/j.ascom.2017.01.003
Ashton, G., & Talbot, C. 2021, Mon. Not. Roy. Astron. Soc., 507, 2037, doi: 10.1093/mnras/stab2236
Ashton, G., Thiele, S., Lecoeuche, Y., McIver, J., & Nuttall, L. K. 2022, Classical and Quantum Gravity, 39, 175004, doi: 10.1088/1361-6382/ac8094

Ashton, G., Hübner, M., Lasky, P. D., et al. 2019, ApJS, 241, 27, doi: 10.3847/1538-4365/ab06fc
Aubin, F., Brighenti, F., Chierici, R., et al. 2021, Classical and Quantum Gravity, 38, 095004, doi: 10.1088/1361-6382/abe913
Baird, E., Fairhurst, S., Hannam, M., & Murphy, P. 2013, PhRvD, 87, 024035, doi: 10.1103/PhysRevD.87.024035
Berry, C. P. L., Mandel, I., Middleton, H., et al. 2015, ApJ, 804, 114, doi: 10.1088/0004-637X/804/2/114
Blanchet, L. 2014, Living Reviews in Relativity, 17, 2, doi: 10.12942/lrr-2014-2
Cannon, K., Cariou, R., Chapman, A., et al. 2012, ApJ, 748, 136, doi: 10.1088/0004-637X/748/2/136
Cannon, K., Caudill, S., Chan, C., et al. 2021, SoftwareX, 14, 100680, doi: 10.1016/j.softx.2021.100680
Chatziioannou, K., Cornish, N., Klein, A., & Yunes, N. 2015, ApJL, 798, L17, doi: 10.1088/2041-8205/798/1/L17
Chatziioannou, K., Cornish, N., Wijngaarden, M., & Littenberg, T. B. 2021, PhRvD, 103, 044013, doi: 10.1103/PhysRevD.103.044013
Chia, H. S., Olsen, S., Roulet, J., et al. 2022, PhRvD, 106, 024009, doi: 10.1103/PhysRevD.106.024009
Christensen, N., & Meyer, R. 2022, Reviews of Modern Physics, 94, 025001, doi: 10.1103/RevModPhys.94.025001
Chu, Q., Kovalam, M., Wen, L., et al. 2022, PhRvD, 105, 024023, doi: 10.1103/PhysRevD.105.024023
Colleoni, M., Ramis Vidal, F. A., García-Quirós, C., Akçay, S., & Bera, S. 2025, PhRvD, 111, 104019, doi: 10.1103/PhysRevD.111.104019
Cornish, N. J., & Littenberg, T. B. 2015, Classical and Quantum Gravity, 32, 135012, doi: 10.1088/0264-9381/32/13/135012
Cornish, N. J., Littenberg, T. B., Bécsy, B., et al. 2021, PhRvD, 103, 044006, doi: 10.1103/PhysRevD.103.044006
Cutler, C., & Flanagan, É. E. 1994, PhRvD, 49, 2658, doi: 10.1103/PhysRevD.49.2658
Cutler, C., Apostolatos, T. A., Bildsten, L., et al. 1993, PhRvL, 70, 2984, doi: 10.1103/PhysRevLett.70.2984
Dal Canton, T., Nitz, A. H., Gadre, B., et al. 2021, ApJ, 923, 254, doi: 10.3847/1538-4357/ac2f9a
Dal Canton, T., Nitz, A. H., Lundgren, A. P., et al. 2014, PhRvD, 90, 082004, doi: 10.1103/PhysRevD.90.082004
Damour, T. 2001, PhRvD, 64, 124013, doi: 10.1103/PhysRevD.64.124013
Davies, G. S., Dent, T., Tápai, M., et al. 2020, PhRvD, 102, 022004, doi: 10.1103/PhysRevD.102.022004
Davis, D., Yarbrough, Z., Areeda, J., et al. 2026, arXiv e-prints, arXiv:2605.16183. https://arxiv.org/abs/2605.16183
Dax, M., Green, S. R., Gair, J., et al. 2021, Phys. Rev. Lett., 127, 241103, doi: 10.1103/PhysRevLett.127.241103
Del Pozzo, W., Berry, C. P. L., Ghosh, A., et al. 2018, MNRAS, 479, 601, doi: 10.1093/mnras/sty1485
Di Renzo, F., Fidecaro, F., Razzano, M., & Sorrentino, N. 2024, arXiv e-prints, arXiv:2401.15392, doi: 10.48550/arXiv.2401.15392
Drago, M., Klimenko, S., Lazzaro, C., et al. 2021, SoftwareX, 14, 100678, doi: 10.1016/j.softx.2021.100678
Essick, R., Godwin, P., Hanna, C., Blackburn, L., & Katsavounidis, E. 2020, Machine Learning: Science and Technology, 2, 015004, doi: 10.1088/2632-2153/abab5f
Essick, R., Coughlin, M. W., Zevin, M., et al. 2025, PhRvD, 112, 102001, doi: 10.1103/44x3-hv3y
Estellés, H., Buonanno, A., Enficiaud, R., Foo, C., & Pompili, L. 2026, PhRvD, 113, 044049, doi: 10.1103/pjbd-pjxn
Estellés, H., Husa, S., Colleoni, M., et al. 2022, ApJ, 924, 79, doi: 10.3847/1538-4357/ac33a0
Fairhurst, S. 2009, New Journal of Physics, 11, 123006, doi: 10.1088/1367-2630/11/12/123006
—. 2011, Classical and Quantum Gravity, 28, 105021, doi: 10.1088/0264-9381/28/10/105021
Farr, B., Berry, C. P. L., Farr, W. M., et al. 2016, ApJ, 825, 116, doi: 10.3847/0004-637X/825/2/116
Farrow, N., Zhu, X.-J., & Thrane, E. 2019, ApJ, 876, 18, doi: 10.3847/1538-4357/ab12e3
Finn, L. S., & Chernoff, D. F. 1993, PhRvD, 47, 2198, doi: 10.1103/PhysRevD.47.2198
Fishbach, M., Holz, D. E., & Farr, B. 2017, ApJL, 840, L24, doi: 10.3847/2041-8213/aa7045
Fisher, R. P., Hemming, G., Bizouard, M.-A., et al. 2021, SoftwareX, 14, 100677, doi: 10.1016/j.softx.2021.100677
García-Bellido, J., Nuño Siles, J. F., & Ruiz Morales, E. 2021, Physics of the Dark Universe, 31, 100791, doi: 10.1016/j.dark.2021.100791
Ghonge, S., Chatziioannou, K., Clark, J. A., et al. 2020, PhRvD, 102, 064056, doi: 10.1103/PhysRevD.102.064056
Glanzer, J., Banagiri, S., Coughlin, S. B., et al. 2023, Classical and Quantum Gravity, 40, 065004, doi: 10.1088/1361-6382/acb633
Green, R., Hoy, C., Fairhurst, S., et al. 2021, Phys. Rev. D, 103, 124023, doi: 10.1103/PhysRevD.103.124023
Grover, K., Fairhurst, S., Farr, B. F., et al. 2014, PhRvD, 89, 042004, doi: 10.1103/PhysRevD.89.042004
Gupta, T., & Cornish, N. J. 2024, PhRvD, 109, 064040, doi: 10.1103/PhysRevD.109.064040
Hamilton, E., Colleoni, M., Thompson, J. E., et al. 2026, PhRvD, 113, 084055, doi: 10.1103/kxsf-23rr
Hanna, C., Caudill, S., Messick, C., et al. 2020, PhRvD, 101, 022003, doi: 10.1103/PhysRevD.101.022003
Harris, C. R., Millman, K. J., van der Walt, S. J., et al. 2020, Nature, 585, 357, doi: 10.1038/s41586-020-2649-2
Helmling-Cornell, A. F., Nguyen, P., Schofield, R. M. S., & Frey, R. 2024, Classical and Quantum Gravity, 41, 145003, doi: 10.1088/1361-6382/ad5139

Hourihane, S., Chatziioannou, K., Wijngaarden, M., et al. 2022, PhRvD, 106, 042006, doi: 10.1103/PhysRevD.106.042006
Hoy, C., Fairhurst, S., & Mandel, I. 2025, Phys. Rev. D, 111, 023037, doi: 10.1103/PhysRevD.111.023037
Hoy, C., & Raymond, V. 2021, SoftwareX, 15, 100765, doi: 10.1016/j.softx.2021.100765
Huang, Y., Middleton, H., Ng, K. K. Y., Vitale, S., & Veitch, J. 2018, PhRvD, 98, 123021, doi: 10.1103/PhysRevD.98.123021
Hunter, J. D. 2007, Computing in Science and Engineering, 9, 90, doi: 10.1109/MCSE.2007.55
Huxford, R., George, R., Trevor, M., Yarbrough, Z., & Godwin, P. 2024, arXiv e-prints, arXiv:2412.04638, doi: 10.48550/arXiv.2412.04638
Johnson-McDaniel, N. K., Ghosh, A., Ghonge, S., et al. 2022, PhRvD, 105, 044020, doi: 10.1103/PhysRevD.105.044020
Joshi, P., Tsukada, L., Hanna, C., et al. 2025, arXiv e-prints, arXiv:2506.06497, doi: 10.48550/arXiv.2506.06497
Kafka, P. 1988, in ESA Special Publication, Vol. 283, ESA Special Publication, ed. W. R. Burke, 121–130
Kasliwal, M. M., & Nissanke, S. 2014, ApJL, 789, L5, doi: 10.1088/2041-8205/789/1/L5
Kidder, L. E. 1995, PhRvD, 52, 821, doi: 10.1103/PhysRevD.52.821
Klimenko, S. 2022, arXiv e-prints, arXiv:2201.01096, doi: 10.48550/arXiv.2201.01096
Klimenko, S., & Mitselmakher, G. 2004, Classical and Quantum Gravity, 21, S1819, doi: 10.1088/0264-9381/21/20/025
Klimenko, S., Mohanty, S., Rakhmanov, M., & Mitselmakher, G. 2005, PhRvD, 72, 122002, doi: 10.1103/PhysRevD.72.122002
Klimenko, S., Yakushin, I., Mercer, A., & Mitselmakher, G. 2008, Classical and Quantum Gravity, 25, 114029, doi: 10.1088/0264-9381/25/11/114029
Klimenko, S., Vedovato, G., Drago, M., et al. 2011, PhRvD, 83, 102001, doi: 10.1103/PhysRevD.83.102001
—. 2016, PhRvD, 93, 042004, doi: 10.1103/PhysRevD.93.042004
Koloniari, A. E., Koursoumpa, E. C., Nousi, P., et al. 2025, Machine Learning: Science and Technology, 6, 015054, doi: 10.1088/2632-2153/adb5ed
Kovalam, M., Kaium Patwary, M. A., Sreekumar, A. K., et al. 2022, ApJL, 927, L9, doi: 10.3847/2041-8213/ac5687
Krishnendu, N. V., & Ohme, F. 2022, Phys. Rev. D, 105, 064012, doi: 10.1103/PhysRevD.105.064012
Krolak, A., & Schutz, B. F. 1987, General Relativity and Gravitation, 19, 1163, doi: 10.1007/BF00759095
Kumar, P., & Dent, T. 2024, PhRvD, 110, 043036, doi: 10.1103/PhysRevD.110.043036
Landry, P., & Read, J. S. 2021, ApJL, 921, L25, doi: 10.3847/2041-8213/ac2f3e
Lange, J., O'Shaughnessy, R., Boyle, M., et al. 2017, PhRvD, 96, 104041, doi: 10.1103/PhysRevD.96.104041
LIGO–Virgo–KAGRA Collaboration. 2018, LVK Algorithm Library - LALSuite, Free software (GPL), doi: 10.7935/GT1W-FZ16
—. 2025, LIGO/Virgo/KAGRA Public Alerts User Guide. https://emfollow.docs.ligo.org/userguide
—. 2026a, GWTC-5.0: Parameter Estimation Data Release (Part 1 of 2), Zenodo, doi: 10.5281/zenodo.20276105
—. 2026b, GWTC-5.0: Parameter Estimation Data Release (Part 2 of 2), Zenodo, doi: 10.5281/zenodo.20291739
—. 2026c, LIGO, VIRGO AND KAGRA OBSERVING RUN PLANS. https://observing.docs.ligo.org/plan/
—. 2026d, GWTC-5.0: Candidate Data Release, Zenodo, doi: 10.5281/zenodo.20276129
—. 2026e, GWTC-4.1: Candidate Data Release, Zenodo, doi: 10.5281/zenodo.20276094
—. 2026f, GWTC-4.1: Parameter Estimation Data Release, Zenodo, doi: 10.5281/zenodo.20275768
—. 2026g, GWTC-5.0: Glitch Modelling for Events, In preparation
—. 2026h, GWTC-5.0: Data Quality Products for Transient Gravitational Wave Searches, In preparation
—. 2026i, GWTC-5.0: O4a+O4b Search Sensitivity Estimates, Zenodo, doi: 10.5281/zenodo.19500064
—. 2026j, GWTC-5.0: Cumulative Search Sensitivity Estimates, Zenodo, doi: 10.5281/zenodo.19500052
LIGO Scientific Collaboration, VIRGO Collaboration, & KAGRA Collaboration. 2024, GRB Coordinates Network, 36812, 1
Littenberg, T. B., & Cornish, N. J. 2015, PhRvD, 91, 084034, doi: 10.1103/PhysRevD.91.084034
Littenberg, T. B., Kanner, J. B., Cornish, N. J., & Millhouse, M. 2016, PhRvD, 94, 044050, doi: 10.1103/PhysRevD.94.044050
Macleod, D. M., Areeda, J. S., Coughlin, S. B., Massinger, T. J., & Urban, A. L. 2021, SoftwareX, 13, 100657, doi: 10.1016/j.softx.2021.100657
Magee, R., Fong, H., Caudill, S., et al. 2019, ApJL, 878, L17, doi: 10.3847/2041-8213/ab20cf
Mehta, A. K., Buonanno, A., Gair, J., et al. 2022, ApJ, 924, 39, doi: 10.3847/1538-4357/ac3130
Messick, C., Blackburn, K., Brady, P., et al. 2017, PhRvD, 95, 042001, doi: 10.1103/PhysRevD.95.042001
Mishra, T., Bhaumik, S., Gayathri, V., et al. 2025, PhRvD, 111, 023054, doi: 10.1103/PhysRevD.111.023054
Mozzon, S., Nuttall, L. K., Lundgren, A., et al. 2020, Classical and Quantum Gravity, 37, 215014, doi: 10.1088/1361-6382/abac6c
NASA. 2025, GCN, gcn.nasa.gov
Ng, K. K. Y., Vitale, S., Zimmerman, A., et al. 2018, PhRvD, 98, 083007, doi: 10.1103/PhysRevD.98.083007
Nissanke, S., Kasliwal, M., & Georgieva, A. 2013, ApJ, 767, 124, doi: 10.1088/0004-637X/767/2/124
Nissanke, S., Sievers, J., Dalal, N., & Holz, D. 2011, ApJ, 739, 99, doi: 10.1088/0004-637X/739/2/99

Nitz, A. H., Capano, C., Nielsen, A. B., et al. 2019, ApJ, 872, 195, doi: 10.3847/1538-4357/ab0108
Nitz, A. H., Capano, C. D., Kumar, S., et al. 2021, ApJ, 922, 76, doi: 10.3847/1538-4357/ac1c03
Nitz, A. H., Dal Canton, T., Davis, D., & Reyes, S. 2018, PhRvD, 98, 024050, doi: 10.1103/PhysRevD.98.024050
Nitz, A. H., Dent, T., Dal Canton, T., Fairhurst, S., & Brown, D. A. 2017, ApJ, 849, 118, doi: 10.3847/1538-4357/aa8f50
Nitz, A. H., Kumar, S., Wang, Y.-F., et al. 2023, ApJ, 946, 59, doi: 10.3847/1538-4357/aca591
Nitz, A. H., Schäfer, M., & Dal Canton, T. 2020a, ApJL, 902, L29, doi: 10.3847/2041-8213/abbc10
Nitz, A. H., & Wang, Y.-F. 2021a, PhRvL, 126, 021103, doi: 10.1103/PhysRevLett.126.021103
—. 2021b, ApJ, 915, 54, doi: 10.3847/1538-4357/ac01d9
Nitz, A. H., Dent, T., Davies, G. S., et al. 2020b, ApJ, 891, 123, doi: 10.3847/1538-4357/ab733f
Nuttall, L. K. 2018, Philosophical Transactions of the Royal Society of London Series A, 376, 20170286, doi: 10.1098/rsta.2017.0286
Olsen, S., Venumadhav, T., Mushkin, J., et al. 2022, PhRvD, 106, 043009, doi: 10.1103/PhysRevD.106.043009
Özel, F., & Freire, P. 2016, ARA&A, 54, 401, doi: 10.1146/annurev-astro-081915-023322
Pankow, C., Brady, P., Ochsner, E., & O'Shaughnessy, R. 2015, PhRvD, 92, 023002, doi: 10.1103/PhysRevD.92.023002
Poisson, E., & Will, C. M. 1995, PhRvD, 52, 848, doi: 10.1103/PhysRevD.52.848
Pompili, L., Buonanno, A., Estellés, H., et al. 2023, PhRvD, 108, 124035, doi: 10.1103/PhysRevD.108.124035
Powell, J. 2018, Classical and Quantum Gravity, 35, 155017, doi: 10.1088/1361-6382/aacf18
Pratten, G., Schmidt, P., Buscicchio, R., & Thomas, L. M. 2020, Physical Review Research, 2, 043096, doi: 10.1103/PhysRevResearch.2.043096
Pratten, G., García-Quirós, C., Colleoni, M., et al. 2021, PhRvD, 103, 104056, doi: 10.1103/PhysRevD.103.104056
Pürrer, M., Hannam, M., & Ohme, F. 2016, PhRvD, 93, 084042, doi: 10.1103/PhysRevD.93.084042
Racine, É. 2008, PhRvD, 78, 044021, doi: 10.1103/PhysRevD.78.044021
Ramos-Buades, A., Buonanno, A., Estellés, H., et al. 2023, PhRvD, 108, 124037, doi: 10.1103/PhysRevD.108.124037
Ray, A., Niu, W., Sakon, S., et al. 2023, arXiv e-prints, arXiv:2306.07190, doi: 10.48550/arXiv.2306.07190
Relton, P., & Raymond, V. 2021, PhRvD, 104, 084039, doi: 10.1103/PhysRevD.104.084039
Robinet, F., Arnaud, N., Leroy, N., et al. 2020, SoftwareX, 12, 100620, doi: 10.1016/j.softx.2020.100620
Romero-Shaw, I. M., Talbot, C., Biscoveanu, S., et al. 2020, MNRAS, 499, 3295, doi: 10.1093/mnras/staa2850
Sachdev, S., Caudill, S., Fong, H., et al. 2019, arXiv e-prints, arXiv:1901.08580, doi: 10.48550/arXiv.1901.08580
Sachdev, S., Magee, R., Hanna, C., et al. 2020, ApJL, 905, L25, doi: 10.3847/2041-8213/abc753
Sakon, S., Tsukada, L., Fong, H., et al. 2024, PhRvD, 109, 044066, doi: 10.1103/PhysRevD.109.044066
Salemi, F., Milotti, E., Prodi, G. A., et al. 2019, PhRvD, 100, 042003, doi: 10.1103/PhysRevD.100.042003
Santamaría, L., Ohme, F., Ajith, P., et al. 2010, PhRvD, 82, 064016, doi: 10.1103/PhysRevD.82.064016
Schmidt, P., Ohme, F., & Hannam, M. 2015, PhRvD, 91, 024043, doi: 10.1103/PhysRevD.91.024043
Schutz, B. F. 1986, Nature, 323, 310, doi: 10.1038/323310a0
SCiMMA. 2025, SCiMMA Hopskotch, scimma.org/hopskotch
Singer, L. P., Price, L. R., Farr, B., et al. 2014, ApJ, 795, 105, doi: 10.1088/0004-637X/795/2/105
Singer, L. P., Chen, H.-Y., Holz, D. E., et al. 2016, ApJL, 829, L15, doi: 10.3847/2041-8205/829/1/L15
Smith, J. R., Abbott, T., Hirose, E., et al. 2011, Classical and Quantum Gravity, 28, 235005, doi: 10.1088/0264-9381/28/23/235005
Soni, S., Berger, B. K., Davis, D., et al. 2025, Classical and Quantum Gravity, 42, 085016, doi: 10.1088/1361-6382/adc4b6
Speagle, J. S. 2020, MNRAS, 493, 3132, doi: 10.1093/mnras/staa278
Stevenson, S., Berry, C. P. L., & Mandel, I. 2017, MNRAS, 471, 2801, doi: 10.1093/mnras/stx1764
Talbot, C., & Thrane, E. 2017, PhRvD, 96, 023012, doi: 10.1103/PhysRevD.96.023012
Thrane, E., & Talbot, C. 2019, PASA, 36, e010, doi: 10.1017/pasa.2019.2
Tsukada, L., Joshi, P., Adhicary, S., et al. 2023, PhRvD, 108, 043004, doi: 10.1103/PhysRevD.108.043004
Urban, A. L., et al. 2021, gwdetchar/gwdetchar, doi.org/10.5281/zenodo.2575786, Zenodo, doi: 10.5281/zenodo.597016
Usman, S. A., Nitz, A. H., Harry, I. W., et al. 2016, Classical and Quantum Gravity, 33, 215004, doi: 10.1088/0264-9381/33/21/215004
Vajente, G., Huang, Y., Isi, M., et al. 2020, PhRvD, 101, 042003, doi: 10.1103/PhysRevD.101.042003
Varma, V., Field, S. E., Scheel, M. A., et al. 2019, Physical Review Research, 1, 033015, doi: 10.1103/PhysRevResearch.1.033015
Vazsonyi, L., & Davis, D. 2023, Classical and Quantum Gravity, 40, 035008, doi: 10.1088/1361-6382/acafd2
Veitch, J., Mandel, I., Aylott, B., et al. 2012, PhRvD, 85, 104045, doi: 10.1103/PhysRevD.85.104045

Veitch, J., Raymond, V., Farr, B., et al. 2015, PhRvD, 91, 042003, doi: 10.1103/PhysRevD.91.042003

Venumadhav, T., Zackay, B., Roulet, J., Dai, L., & Zaldarriaga, M. 2019, PhRvD, 100, 023011, doi: 10.1103/PhysRevD.100.023011

—. 2020, PhRvD, 101, 083030, doi: 10.1103/PhysRevD.101.083030

Viets, A. D., Wade, M., Urban, A. L., et al. 2018, Classical and Quantum Gravity, 35, 095015, doi: 10.1088/1361-6382/aab658

Villa-Ortega, V., Dent, T., & Barroso, A. C. 2022, Mon. Not. Roy. Astron. Soc., 515, 5718, doi: 10.1093/mnras/stac2120

Virgo Collaboration. 2021, PythonVirgoTools, v5.1.1, git.ligo.org/virgo/virgoapp/PythonVirgoTools

Virtanen, P., Gommers, R., Oliphant, T. E., et al. 2020, Nature Medicine, 17, 261, doi: 10.1038/s41592-019-0686-2

Vitale, S., Lynch, R., Raymond, V., et al. 2017a, PhRvD, 95, 064053, doi: 10.1103/PhysRevD.95.064053

Vitale, S., Lynch, R., Sturani, R., & Graff, P. 2017b, Classical and Quantum Gravity, 34, 03LT01, doi: 10.1088/1361-6382/aa552e

Vitale, S., Lynch, R., Veitch, J., Raymond, V., & Sturani, R. 2014, PhRvL, 112, 251101, doi: 10.1103/PhysRevLett.112.251101

Waskom, M. 2021, The Journal of Open Source Software, 6, 3021, doi: 10.21105/joss.03021

Wette, K. 2020, SoftwareX, 12, 100634, doi: 10.1016/j.softx.2020.100634

Williams, D., Veitch, J., Chiofalo, M., et al. 2023, The Journal of Open Source Software, 8, 4170, doi: 10.21105/joss.04170

Wysocki, D., O'Shaughnessy, R., Lange, J., & Fang, Y.-L. L. 2019, PhRvD, 99, 084026, doi: 10.1103/PhysRevD.99.084026

Zackay, B., Dai, L., Venumadhav, T., Roulet, J., & Zaldarriaga, M. 2021, PhRvD, 104, 063030, doi: 10.1103/PhysRevD.104.063030

Zackay, B., Venumadhav, T., Dai, L., Roulet, J., & Zaldarriaga, M. 2019, PhRvD, 100, 023007, doi: 10.1103/PhysRevD.100.023007

Zevin, M., Berry, C. P. L., Coughlin, S., Chatziioannou, K., & Vitale, S. 2020, ApJL, 899, L17, doi: 10.3847/2041-8213/aba8ef

Zevin, M., Bavera, S. S., Berry, C. P. L., et al. 2021, ApJ, 910, 152, doi: 10.3847/1538-4357/abe40e

Zweizig, J. 2006, The Data Monitor Tool Project, labcit.ligo.caltech.edu/~jzweizig/DMT-Project.html